THE UNIVERSITY of EDINBURGH

Title	Spectral properties of stars and stellar populations
Author	Murphy, Tara.
Qualification	PhD
Year	2003

Digitisation Notes:

- pages xii, 60,164 missing from original

Spectral Properties of Stars and Stellar Populations

TARA MURPHY

Institute for Astronomy

School of Physics

A thesis submitted to the University of Edinburgh

for the degree of Doctor of Philosophy

September 2003

Abstract

I present the results of an investigation into the spectral properties of stars and galaxies. Firstly I investigate methods for automatic MKK classification of stellar spectra, providing both a comparative study of some of the standard methods of automatic classification and a demonstration of a state-of-the-art machine learning technique — Support Vector Machines. Using this technique I obtain a classification accuracy of $\sigma = 1.7$.

One of the limitations in the classification of stellar spectra is the lack of good training data at high resolution. With this and also the application of population synthesis in mind, I present a high resolution ($\lambda/\Delta\lambda = 250\,000$) library of 6410 synthetic stellar spectra which I have generated from the Kurucz model atmospheres. The library covers the wavelength range $3000 - 10\,000$ with 54 values of effective temperature in the range $5250 - 50\,000$ K, 11 values of log surface gravity between 0.0 and 5.0 and 19 metallicities in the range -5.0 to 1.0. By comparing the new synthetic spectra with the STELIB library of observed spectra (Le Borgne et al., 2003) I demonstrate their suitability for the application of population synthesis.

I then extend this library by supplementing the Kurucz spectra with other synthetic spectra, to form a library for population synthesis similar to that of Lejeune et al. (1998) but at higher resolution (2). I also investigate two methods of empirical population synthesis however I find that even with modern computational resources these methods are not suitable for the number and size of current spectra.

Finally I measure the Lick indices for a sample of Sloan Digital Sky Survey spectra and use these in conjunction with the 2dF groups catalogue to investigate the change in these parameters with the local density of galaxies. I find no strong trends in any of the Lick indices with group velocity dispersion.

Declaration

I hereby declare that this thesis entitled *Spectral Properties of Stars and Stellar Populations* is not substantially the same as any that I have submitted for a degree or diploma or other qualification at any other University. I further state that no part of my thesis has already been or is being concurrently submitted for any such degree, diploma or other qualification.

This thesis is the outcome of my own work except where specifically indicated in the text.

Tara Murphy
Edinburgh,
September 2003.

Acknowledgements

I would like to thank my supervisors Avery Meiksin and John Peacock[1] for the help and support they have given me over the last 3 years, both in technical and personal issues. Also, I have appreciated the support of Dick Hunstead who has been an excellent mentor (and friend) throughout my PhD.

My thesis covers a wide range of topics, and there have been many people I have emailed for advice throughout my PhD. They have all been exceptionally helpful, well beyond the call of duty, and so I must especially thank the following people: Coryn Bailer-Jones, for making his neural network software publicly available, and also making his library of template spectra available to me; Ivan Baldry, for loads of advice on the synthetic spectra, reading my draft paper and showing me some cool IDL tricks; John Lester, for making his Unix version of Kurucz's synthetic spectra code available, updating it when we found problems with it, and responding very quickly to all my enquiries; and Friedrich Kupka, also for advice on the synthetic spectra, but particularly for chasing me down at NAM and explaining all the things that were wrong with my poster – and more importantly how to fix them!

I would also like to thank Robert Kurucz, for explaining some of the finer details of his software, Barry Smalley for advice on generating the synthetic spectra, Michael Kurtz for providing a copy of his thesis on minimum distance methods and Michael Blanton for advice on using his k-correction code and other issues relating to the SDSS spectra.

My examiners, Alan Heavens and Stéphane Charlot, possibly don't realise how grateful I

[1] And thanks to John for introducing me to Scruffy, potentially the craziest dog in Edinburgh if not the world.

am that they managed to organise my viva early, and hence replace a flight back from Australia with a much, much shorter flight to Munich – thanks!

The best thing about my time in Edinburgh was sharing the experience with my fellow students, in particular 'our year' Dave, Dan, Ian, Olivia and Stephen. It was great fun sharing all those dinners – even Dan managed to come through with an impressive meal – and just generally lazing around (in between all the PhD work of course). Stephen (and Peter Brand) provided a never-ending source of interesting and challenging conversations. Ian was always on hand to listen and provide help, useful (and useless) opinions and diversionary activities – the most important of which was of course `thesisplot`, without which we would all still be lost in the PhD wilderness. Olivia, what can I say, it was great having someone else to see arty movies with, share whinges with, and having as close to girly chats as I manage – thanks for being there in all the really rough patches, I wish Sydney wasn't so far away.

On the other side of the world, I have to thank my Mum and Dad. I appreciate immensely the hard work that you have done to give me the opportunity to get this far. Also to Kate and Ben who have had to put up with having a super-nerdy sister for their whole lives! And thanks to Mum for being brave enough to proofread chapters from this thesis – I expect the rest of you to read it too!

Finally I would like to thank James for practically everything else – I couldn't imagine a better person to have gone through my PhD with. It been great learning programming from a Jedi-master, and having a near perfect sysadmin on hand at all times! I don't think either of us can count the number of times you've motivated me to keep going through all the hard bits, done all the chores when neither of us wanted to, listened to all the whinges, eaten endless tubs of Häagen Dazs and Ben & Jerry's (I know you found that particularly difficult), watched more Seachange, and somehow managed to keep motivated and sane enough to do your own PhD at the same time. Our time in Edinburgh was an amazing adventure; the cycling, the Russian, the snow, the mice, the festivals, the travelling, your conversion to art-house cinema and of course the book shopping! Thanks for everything.

Contents

List of Figures

List of Tables

CHAPTER 1

Introduction

This thesis is concerned with the nature of stars and galaxies (or stellar populations), specifically, what we can determine from their spectra. To understand where galaxies fit into the overall picture of the universe we need to look both on smaller scales, at the individual stars that comprise galaxies, and on larger scales at the formation, evolution and distribution of galaxies in a cosmological context. The topics dealt with in this thesis are stellar spectral classification, population synthesis and how the spectral properties of galaxies vary with their local density. It involves both synthetic stellar and galaxy spectra as well as galaxy spectra from the Sloan Digital Sky Survey (SDSS) (York et al., 2000). This introduction outlines the basic astrophysics necessary for each of these areas, before tying them together in the overall theme of the thesis. It is intended to be a very brief overview of the different fields, as specific details of each topic will be discussed further in the introductory sections of each individual chapter.

1.1 Stars and stellar evolution

In terms of scale, stars are the smallest astronomical phenomena I will be concerned with in this thesis. The nature of the light emitted by stars is determined by their surface area, surface temperature and chemical composition of the outer layers. These in turn are determined by the age, mass and the composition of the stellar interiors. To understand and model stellar populations it is necessary to have an understanding of stellar structure and evolution. The structure of stellar atmospheres will be discussed in Chapter 3. The definitive text for stellar atmospheres is Milhalas (1978), however a more accessible account is given in Boehm-Vitense (1989). In this section I will outline what is known about stellar evolution, and how stars at each stage in their evolution contribute to the light emitted from a galaxy.

The fundamental observable property of a star is its flux[1], the total energy received by the observer per second per square metre. The intrinsic property corresponding to flux is the luminosity which is the amount of energy the star emits per second. Assuming the star shines with equal brightness in all directions they are related by the inverse-square law

$$F = \frac{L}{4\pi d^2} \tag{1.1}$$

and hence the key to determining the luminosity is an accurate measurement of the distance, d, to the star. The Sun's bolometric luminosity is $L_\odot = 3.86 \times 10^{26}$ W and stellar luminosities can range from $10^{-4} L_\odot$ to $> 10^6 L_\odot$. The most important correlation in stellar properties is that between luminosity and effective temperature (or colour and absolute magnitude) which forms the Hertzsprung-Russell (HR) diagram (also known as the colour-magnitude diagram). Stars fall into distinctive groups on the HR diagram, which largely correspond to stars in different stages of their evolution. Figure 1.1 shows the HR diagram for a typical globular cluster.

The evolutionary process for normal stars is well known. Some of the main stages in stellar evolution are marked on the HR diagram in Figure 1.1. Stars start as protostellar objects which are formed when clouds of gas become dense enough to collapse under their own gravity. The collapse stops when the temperature in the core is hot enough for hydrogen to undergo

[1] Flux (measured for a specific wavelength range) has SI units of W m^{-3} but is usually quoted in units of erg $s^{-1} cm^{-2-1}$

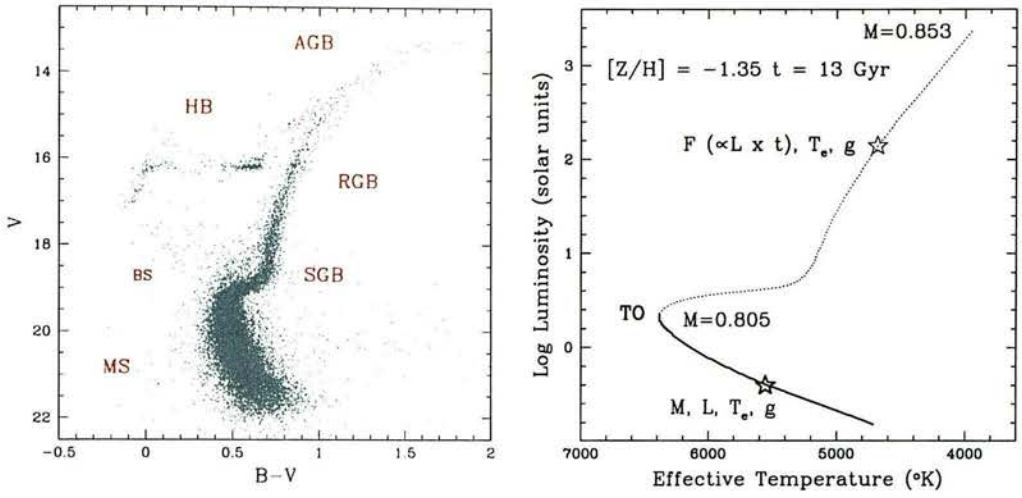

Figure 1.1: The evolutionary stages in the stellar lifecycle. Left: an observed HR diagram for the old, metal poor galactic cluster NGC1851. The main phases in the evolution are shown: Main Sequence (MS), Sub Giant Branch (SGB), Red Giant Branch (RGB), Horizontal Branch (HB), Blue Stragglers (BS) and Asymptotic Giant Branch (AGB). Right: Theoretical HR diagram of an old, metal-poor Simple Stellar Population, up to the RGB-tip (isochrone from Cassisi et al., 1999). The solid line shows the main sequence and the dotted line shows the post-main sequence evolution. The stellar masses at the turnoff (TO) and the RGB tip are annotated. Image source: Maraston (2003), also available online at NASA's Level 5.

nuclear fusion. At this point the pressure from the nuclear reactions balances the force due to gravitational collapse and the star stabilises, becoming a main sequence (MS) star. Stars remain on the main sequence until their core hydrogen supply is exhausted. During this time they move from the left hand boundary of the MS (the Zero Age Main Sequence, ZAMS) across the main sequence band as their surface temperature decreases. When and where stars enter and exit the main sequence depends on their mass, but on average stars remain on the main sequence for about 90% of their lives. More massive stars consume the hydrogen more quickly and hence have shorter MS lives ($\sim$ 7 million years) whereas low mass stars can stay on the MS for much longer (over 10 billion years). The sun is about 4.5×10^9 years old and is approximately half way through its life.

Once stars 'turn off' the main sequence, their subsequent evolutionary paths differ greatly

depending on their mass[2]. In low mass stars ($0.6M_{\odot} < M < 2M_{\odot}$) the core starts to contract and the outer layers expand, causing the star to radiate over a much larger area than before. The surface temperature decreases and the star moves on to the subgiant branch (SGB) which is populated by cool, red stars. The temperature in the hydrogen-burning shell surrounding the core rises, and the star ascends the red giant branch (RGB) as its luminosity increases. When the core of a red giant gets dense enough it becomes degenerate and can not expand. Hence when the temperature reaches a critical point ($\sim 10^8$ K) at which it is hot enough to ignite helium the star undergoes what is known as the helium flash. Helium then replaces hydrogen as the main core fuel, with hydrogen fusion taking place in the surrounding shell. This continues until the core helium supply is exhausted at which point the core contracts and the shell expands again. The star moves onto the asymptotic giant branch (AGB) where both hydrogen and helium fusion occur in its outer shells. At this point the star is more luminous but cooler than it was in the red giant phase. The star eventually ejects its outer layers of gas into a planetary nebula and only the hot core remains as a white dwarf star. From this point the white dwarf gradually cools, becoming increasingly faint.

Intermediate mass stars ($2M_{\odot} < M < 8M_{\odot}$) move directly to the RGB once their core hydrogen is exhausted. Unlike in the low mass stars, in these stars the core does not become degenerate and so there is no helium flash. After helium fusion has started the stars become bluer, moving across the HR diagram, but as the core helium is exhausted the stars become redder again. Then star then moves onto the AGB where, as with the lower mass stars, both hydrogen and helium fusion occur it its outer shells. While on the AGB stellar winds carry heavy elements such as carbon and nitrogen away from the stellar surface. The outer layers of the star are shed (creating a planetary nebula) leaving a white dwarf, which becomes increasingly cooler and fainter.

Massive stars ($M > 8M_{\odot}$) become hot (blue and yellow) supergiants. As the core increases in temperature metals can burn, until iron is produced. At this point the fuel in the core is exhausted and the core collapses and becomes degenerate. The outer shells of the core also collapse rapidly inward until they hit the core and then explode, forming a supernova. This releases large quantities of metals into the interstellar medium, leaving the core of the star as a

[2]Mass is given in terms of the solar mass, where $1M_{\odot} = 1.98892 \times 10^{30}$ kg.

neutron star or black hole.

There are many other aspects of stellar evolution that have not been discussed here as they are not necessary for the basic population synthesis done in Chapter 4. However, for accurate modelling of observed galaxy spectra their more subtle effects must be taken into account. Many of these issues, such as stellar winds, interacting systems and stellar mass loss are discussed in the conference proceedings by Lambert (1991).

Different types of stars can be distinguished by the appearance of their spectra, both from the continuum shape and line features. Broad classification schemes separate stars of different types such as carbon stars and white dwarfs from 'normal' main sequence stars and giants. These more unusual types of stars have their own sub-classification schemes (see, for example, Keenan (1993) for carbon stars and Sion et al. (1983) for white dwarfs). Normal main sequence and giant stars are classified into discrete spectral types and luminosity classes. The standard scheme for doing this is MKK classification (Morgan and Keenan, 1973). In the MKK system the main sequence stars, ranging from hot, blue stars to cool, red stars are all referred to as dwarfs and have luminosity class V. Supergiant, giant and subgiant stars have luminosity classes I, II, III and IV. All stars are classified with a spectral type ranging from O (hot) to M (cool). Details of the MKK system are given in Section 2.2. An excellent resource for MKK classification in the modern era is the conference proceedings by Corbally et al. (1994).

The MKK system suits the traditional method of stellar classification where astronomers examine each spectrum by eye and make a decision about its category. An alternative to discrete classification systems is physical parameterisation, which aims to establish where the star lies on the three dimensional continuum of parameters: effective temperature, surface gravity and metallicity. Effective temperature is a measure of how much energy is emitted through a unit area of the star's surface and is defined by the Stefan-Boltzmann Law

$$L \equiv 4\pi R^2 \sigma T_{\rm eff}^4 \tag{1.2}$$

where L is the luminosity of the star, R is the radius and σ is the Stefan-Boltzmann constant[3].

[3] $\sigma = 5.6703 \times 10^{-8} \mathrm{Wm^{-2}K^{-4}}$

Surface gravity determines the pressure gradient in the star's atmosphere and is defined as

$$g \equiv \frac{GM}{R^2} \tag{1.3}$$

where M is the mass of the star, R is the radius and G is the gravitational constant [4]. It is possible to measure these parameters directly for a small number of close stars (*e.g.* Hanbury Brown et al., 1974), but for other stars they must be obtained indirectly. This has become possible with the development of stellar spectral synthesis packages such as ATLAS9 and SYNTHE (Kurucz, 1992) and NextGen (Hauschildt et al., 1999a,b). These packages allow the generation of a grid of spectra covering a wide range of physical parameter space which can be used as templates for classifying observed spectra. Physical parameterisation can be calibrated against the MKK system using the effective temperature scale (*i.e.* the relationship between the effective temperature of a star and its spectral type). Methods for developing an effective temperature scale are summarised by Boehm-Vitense (1981). Physical parameterisation is addressed in Section 2.2.

Classification of stellar spectra by hand is not feasible when faced with the large number of spectra generated by modern surveys. The alternative is automatic classification. Progress in this field is summarised by Bailer-Jones (2001). The most successful methods so far have been machine learning methods, specifically artificial neural networks. In Chapter 2 I do a comparative study of these methods and highlight their problems and limitations. I then demonstrate a machine learning method that has not been used extensively in astrophysics — the Support Vector Machine (SVM). A complete coverage of the theory behind SVMs and their applications is given by Cristianini and Shawe-Taylor (2000). Automatic classification will become essential for classifying the large number of stars observed in future surveys such as GAIA (Lindegren and Perryman, 1996), for use in generating population synthesis models.

1.2 Stellar populations

The light from galaxies is to some approximation the integrated light from all of the component stars. However, almost all galaxies are too far away to be able to separate out the light

[4] $G = 6.672 \times 10^{-11} \mathrm{m^3 kg^{-1} s^{-2}}$

from the different stars to study a galaxy's composition. Instead we can synthesise models of galaxies, match the resulting spectra to observations and hence infer the properties of the observed galaxy. This section outlines the basic principles behind evolutionary population synthesis (EPS). Two good summaries of population synthesis are Bruzual (2001) and Maraston (2003). A good resource for details of all aspects of population synthesis is the conference proceedings by Leitherer et al. (1996b).

The term *stellar population* refers to a group of stars born at the same time and having the same initial composition. It primarily refers to synthetically generated stellar populations which are designed to model globular star clusters or galaxies. Galaxies are a complex combination of stellar populations — most synthetic stellar populations are greatly simplified in some way. The simplest system is the Simple Stellar Population (SSP) which is a coeval (*i.e.* all stars formed at the same time) and chemically homogeneous group of stars. An SSP is completely characterised by its age, chemical composition and initial mass function (IMF). Although these simple systems do not accurately reflect the properties of galaxies, their simplicity means that theories of stellar evolution can be used successfully to predict their global properties, as done by Tinsley and Gunn (1976) and Renzini and Buzzoni (1986).

Galaxies are usually referred to in terms of their morphological properties, *i.e.* ellipticals and spirals. Comparison of the galaxy spectra with stellar spectra led to the development of empirical population synthesis, the precursor to evolutionary population synthesis. This approach involves working backward from the galaxy spectra to obtain the fractional contribution from each type of stellar spectrum (*e.g.* Faber, 1973; Pickles, 1985). I will discuss aspects of empirical population synthesis further in Section 4.3. Most of the work in both empirical and evolutionary population synthesis is concerned with investigating the populations of 'normal' spiral and elliptical galaxies, however there is also some work in other areas, for example starburst galaxies (Poggianti et al., 2001) and Wolf-Rayet galaxies (Conti, 2000).

The key feature of the EPS approach is the use of theoretical stellar evolutionary *isochrones*. An isochrone is made up of tracks, each of which plot the evolutionary path for a star of a given mass, with time (specifically, the change in luminosity and effective temperature). Hence the isochrone shows the distribution of temperatures and luminosities for stars of a range of masses,

at a given time. This is where an understanding of the evolutionary path of different types of stars is important for galaxy population synthesis. Each stage in the evolution must be included, from pre-main sequence stars to white dwarfs. Examples of commonly used stellar tracks are those from the Padova (Bressan et al., 1993), Geneva (Schaller et al., 1992; Charbonnel et al., 1996) and Yale (Yi et al., 2001) groups. The isochrones are a major source of error in population synthesis results, as shown in a study by Charlot et al. (1996). Two of the main issues that cause differences between the sets of tracks are whether convective overshooting is accounted for and what mixing length is used (these will be defined in Section 3.2). The computational approach to EPS falls into one of two categories, either fuel consumption theory (Renzini and Buzzoni, 1986) or isochrone synthesis (Charlot and Bruzual, 1991).

EPS also requires a library of stellar spectra covering a range of different spectral types. These can be theoretical (*e.g.* Lejeune et al., 1997) or empirical (*e.g.* Le Borgne et al., 2003) or a combination of both. A wide range of spectra suitable for stellar population modelling is available as part of a database described by Leitherer et al. (1996a). The quality of the final synthesised galaxy spectra is sensitive to the accuracy of the grid of input stellar spectra. Observational libraries have limited wavelength coverage, limited coverage of parameter space and observational and calibration uncertainties. Theoretical libraries can be created to cover any range of parameter space, but do not always match observed stellar spectra accurately (particularly for cooler stars where molecular lines are important). Until recently neither observed or theoretical libraries of stellar spectra have been available at high resolution (over a reasonable wavelength range). This was of particular interest to me as I intended to compare synthetic galaxy spectra with those from the SDSS. Synthetic grids of spectra over wide wavelength ranges were only available at a resolution of 20 , much lower than the SDSS ($\sim 1-2$). This issue is discussed further in Section 4.2 where I present a higher resolution library of synthetic stellar spectra.

Although there are still many issues to resolve in accurate modelling of galaxy spectra, there are some basic results that have come out of evolutionary population synthesis. Some of these are:

- populations become less luminous with increasing age;

- populations become redder with increasing age or metallicity;
- neutral metal lines increase in strength with increasing age or metallicity;
- after about 10^8 years, hydrogen lines decrease in strength with increasing age or abundance;
- most of the blue light in galaxies comes from the hotter stars (with spectral types of A, F and G);
- the extremely hot stars (with spectral types O and B) are rare and so do not contribute much to the total light, except when the galaxy has undergone recent star formation;
- most of the light at the red end of the spectrum comes from cool stars (typically with spectral type K).

1.3 Galaxies in a cosmological context

The final part of this thesis is concerned with how the spectral properties of galaxies relate to their environment. In particular I will investigate the dependence of galaxy properties on local density, *i.e.* the density of galaxies around a particular galaxy. Redshift surveys are the crucial tool in allowing us to build up a three dimensional picture of the way galaxies are distributed throughout the universe. The results from these surveys have to be interpreted assuming a particular cosmological model, which specifies the geometry and dynamics of the universe in which the observations have been made. Assuming that on the largest scales the universe is homogeneous and that it is expanding isotropically, the geometry of the universe can be described by the Robertson-Walker metric. The solutions to Einstein's general relativistic field equations, assuming this geometry, are the Friedmann cosmological models. This section outlines only the concepts and equations used in this thesis (specifically in Chapter 5). For a complete discussion of cosmological issues and the derivations behind these equations, see Peebles (1993) and Peacock (2000).

In the local universe, measuring the distance to or between objects is quite straightforward.

However, on cosmological scales it is complex, and dependent on the cosmological model adopted and the distance measure used. It is important to distinguish between the different ways of measuring distance, and clearly identify which one is being used. This section outlines the basic cosmological tools necessary to measure the distance to galaxies from their redshifts. Knowing the distance allows us to calculate properties such as the absolute magnitude of the galaxies. The absolute magnitude of a source is defined as the magnitude it would be if it were located at a distance of 10 parsecs from the observer. Hence the difference between the absolute and apparent magnitudes for a particular source is given by

$$m - M = 5\log_{10}(D/10\,\mathrm{pc}) \tag{1.4}$$

where D is the distance, and assuming there is no obscuration by interstellar dust. On cosmological scales we have to choose an appropriate distance measure for D.

The recessional speed of the expanding universe is related to distance by the Hubble parameter, H

$$v = H_0 D\,. \tag{1.5}$$

In general H changes with time, so at the current time it is denoted H_0 (the Hubble constant) and has dimensions

$$H_0 = 100h_0\,\mathrm{km\,s^{-1}Mpc^{-1}} \tag{1.6}$$

where h_0 is a dimensionless parameter. The current best estimate for the Hubble constant comes from the Hubble Space Telescope Key Project by Freedman et al. (2001) which measured a value of $H_0 = 72 \pm 8\,\mathrm{kms^{-1}Mpc^{-1}}$. The Hubble constant determines the scale of the universe in terms of the Hubble time

$$t_H \equiv \frac{1}{H_0} \tag{1.7}$$

and the Hubble distance

$$D_H \equiv \frac{c}{H_0}\,. \tag{1.8}$$

The dynamical properties of the universe are determined by the matter and radiation densities and the cosmological constant Λ. In a universe with matter, radiation and a cosmological constant, the total density ρ is given by

$$\rho = \rho_m + \rho_r + \rho_\Lambda\,. \tag{1.9}$$

To express these in terms of observable quantities we define a density parameter

$$\Omega = \frac{\rho}{\rho_c} = \frac{8\pi G\rho}{3H^2} \tag{1.10}$$

where ρ_c is the critical density, for which the universe would have a flat geometry. If the density of the universe is less than the critical density, then the universe would have open geometry (and hence, if the cosmological constant $\Lambda = 0$, would expand forever). Similarly if the density of the universe is greater than the critical density the universe would have closed geometry. The individual components of the density parameter (in the current epoch) are given by

$$\Omega_{m,0} = \frac{8\pi G\rho_{m,0}}{3H_0^2} \tag{1.11}$$

$$\Omega_{r,0} = \frac{8\pi G\rho_{r,0}}{3H_0^2} \tag{1.12}$$

$$\Omega_{\Lambda,0} = \frac{\Lambda c^2}{3H_0^2} \tag{1.13}$$

so that

$$\Omega_0 = \Omega_{m,0} + \Omega_{r,0} + \Omega_{\Lambda,0}\,. \tag{1.14}$$

Inflation theory predicts that the total density $\Omega_0 = 1$. The contribution to Ω_0 from the radiation energy density can be estimated from the Cosmic Microwave Background (CMB). The CMB is almost isotropic in all directions on the sky (to one part in 10^5) and corresponds to a black body spectrum with a temperature of 2.728 K. It is found that the contribution from $\Omega_{r,0}$ can be neglected at the current time (the universe is Λ-dominated), however this is not the case for the very early stages of the universe when it was radiation dominated. Hence the parameters that are necessary to define the cosmological model that is being used are $\Omega_{m,0}$, $\Omega_{\Lambda,0}$ and h_0. The current best estimate parameters are (0.27, 0.73, 0.71) which are given by Bennett et al. (2003) in their presentation of the results from the first year of observations with the Wilkinson Microwave Anisotropy Probe (WMAP). Throughout this thesis I will be using a model with parameters $(\Omega_{m,0}, \Omega_{\Lambda,0}, h_0) = (0.3, 0.7, 0.7)$ which approximately correspond to those given by Bennett et al. (2003). This corresponds to a scenario in which the universe has open geometry and expands forever. In such a model, the age of the universe at the present time is $t_0 = 9.43h^{-1}$ Gyr.

Once the cosmological model has been selected, the crucial property for calculating the distance to an object is its redshift, z. In terms of shifts observed in spectral lines the redshift is

defined as

$$\frac{\nu_e}{\nu_o} \equiv 1 + z \tag{1.15}$$

where ν_e is the frequency the light was emitted at and ν_o is the frequency it appears to the observer. The observable quantity redshift, must now be converted into a distance measure suitable for use in Equation 1.4. The luminosity distance is defined as

$$D_L \equiv \sqrt{\frac{L}{4\pi S}} \tag{1.16}$$

where L is the bolometric luminosity and S is the bolometric flux. In a flat cosmology it can be written as

$$D_L = \frac{c}{H_0}(1+z)\int_0^z \frac{dz'}{E(z')} \tag{1.17}$$

where $E(z)$ is given by

$$H_0 E(z) = H_0[\Omega_m(1+z)^3 + \Omega_r(1+z)^4 + \Omega_\Lambda]^{1/2}\,. \tag{1.18}$$

Hence for a flat cosmology ($\Omega_r = 0$) the luminosity distance is given by

$$D_L = \frac{c}{H_0}(1+z)\int_0^z \frac{dz}{[\Omega_m(1+z)^3 + \Omega_\Lambda]^{1/2}} \tag{1.19}$$

When an object is redshifted the amount of flux received in each waveband is also affected because the object is emitting flux in a different waveband to the one being observed. To account for this, the *k-correction* is used. This correction factor modifies Equation 1.16 so that the flux in a given band is given by

$$S_\nu = (1+z)\frac{L_{(1+z)\nu}}{L_\nu}\frac{L_\nu}{4\pi D_L^2} \tag{1.20}$$

where the ratio of luminosities accounts for the difference in flux between the observed and emitted bands, and the factor of $(1+z)$ accounts for the change in bandwidth due to the redshift. A useful reference for the definition of k-corrections and associated equations is the preprint by Hogg et al. (2002).

Now we can reconsider the relationship between absolute and apparent magnitudes, given in Equation 1.4, using the luminosity distance and applying the k-correction

$$m - M = 5\log_{10}(D_L/10\,\mathrm{pc}) - 2.5\log\left[(1+z)\frac{L_{(1+z)\nu}}{L_\nu}\right] \tag{1.21}$$

where the $5\log_{10}(D_L/10\,\mathrm{pc})$ term is usually referred to as the *distance modulus*.

1.4 Motivation

The motivation for this thesis comes from the aim of studying the way spectral properties of galaxies vary with their local environment, making use of the large number of spectra available as part of the SDSS. This problem can be approached from a purely empirical point of view (*i.e.* looking directly at the data and seeing what trends are evident) and from a theoretical point of view (*i.e.* studying the properties of systems we have complete knowledge of — synthetic galaxies). This thesis investigates both approaches, making use of high resolution stellar and galaxy spectra from the SDSS.

The SDSS is a large redshift survey which, when finished, will have observed around 1 million objects covering a quarter of the sky. It consists of both imaging and spectroscopic data. The spectroscopic survey is predominantly a survey for bright galaxies, luminous red galaxies and quasars. The wavelength coverage is $\lambda = 3800 - 9200$ with a spectral resolution of $\lambda/\Delta\lambda \sim 1800$. So far there have been two data releases, the Early Data Release (EDR) (Stoughton et al., 2002) and Data Release 1 (DR1) (Abazajian et al., 2003). The DR1, which is what I have been using, consists of 186 250 spectra of which 134 000 are galaxy spectra, 18 680 are quasars and 22 100 are stellar spectra. The SDSS will be discussed in Section 5.2.

As I will discuss in Chapter 4 the galaxy population synthesis tools have been limited by the completeness and resolution of the stellar spectra available as an input grid. To compare the properties of SDSS resolution galaxies with synthetic galaxies it would be necessary to smooth the SDSS galaxies, which loses important fine grained information and hence does not fully utilise the SDSS spectra. With this limitation in mind, one of the aims of my thesis was to generate a grid of high resolution synthetic spectra to use in population synthesis. The Kurucz (1992) synthetic spectra are one of the main grids of spectra used for population synthesis, but these were only available at low resolution (20). The computational resources required to generate synthetic spectra at high resolution has so far limited the availability of such spectra. One of my aims was to investigate the process involved in generating high resolution synthetic spectra, and in Chapter 3 I present a new library of high resolution spectra generated from the Kurucz model atmospheres.

Before studying the spectral properties of galaxies I decided to look at the spectral properties of their component objects, stars. Stars are much simpler systems than galaxies and they have an established spectral classification scheme. I have investigated the automatic classification of stellar spectra, as a useful subject in its own right, and as a testbed of some of the tools that would later be useful for parameterising galaxy spectra. However, it became clear that the problem of stellar classification and galaxy classification are quite different. Although some of the tools, such as principal component analysis are applicable to both, automatic stellar classification is a supervised machine learning problem whereas galaxy classification is, in general, not. In Chapter 2 I present a comparative study of stellar classification techniques, and demonstrate the use of a new technique, Support Vector Machines.

The final section of my thesis deals with how galaxy spectral properties change with their local environment. Large surveys allow the study of subtle statistical trends across a massive number of objects. The environmental factor I consider is *local density*, a measure of the number of galaxies in a galaxy's immediate environment. There are clear differences in the nature of galaxies at both extremes: a lone field galaxy is generally different to a galaxy near the centre of a massive cluster. There are well known trends of metallicity with the properties of individual galaxies, for example more massive galaxies tend to be more metal rich. The aim of the final chapter is to see whether there are any trends between Lick index strength in galaxies and their environments. In future work this analysis could be compared to the predictions from semi-analytic galaxy formation scenarios, making use of the high resolution synthetic spectra that I discuss in Chapters 3 and 4.

CHAPTER 2

Automatic classification of stellar spectra

"The classification should describe the spectra not the stars; that is it should be based solely on what can be seen in the spectrum of a given star..."

IAU Commission 21, 1921

2.1 Introduction

A good classification system is central to most areas of science, often being developed very early on in the progress of the field. Stellar astrophysics is no exception to this and in the 1860's, around the same time spectroscopic instruments were being used for the first time, Angelo Secchi classified thousands of stars into four groups, based on their similarity to the sun. There are several reasons why classification is important. Firstly, particularly in astrophysics, empirical observations are the basis for much of the research in the field. They are the only

guaranteed knowledge, and a classification based purely on observations will survive regardless of changes in theory. Secondly, the amount of information that we are forced to process if we treat each star as an individual, different to others, is so overwhelming as to be near useless. To draw meaningful conclusions from the data we are forced to group it into categories of objects which share certain properties. Finally, and of most interest to the scientist, classification can lead to a deeper physical understanding of the data.

There are two general ways of approaching modern stellar spectral classification; MKK classification and physical parameterisation. The aim of MKK classification is to find a way of accurately classifying the spectra into the already established MKK classes. The aim of physical parameterisation is to establish where the star lies on the three dimensional continuum of physical parameters; effective temperate ($T_{\rm eff}$), surface gravity ($\log(g)$) and metallicity ([M/H]). The MKK system suits the traditional way of doing stellar classification — where astronomers examine each spectrum by eye, and make a decision about it category. Physical parameterisation has become possible with the development of reasonably accurate spectral synthesis packages such as ATLAS9 and SYNTHE (Kurucz, 1992) and NextGen (Hauschildt et al., 1999a,b). These packages allow the generation of a grid of spectra covering a wide range of physical parameters which can be used as templates for classifying observed spectra. I will discuss these classification systems in more detail in Section 2.2. The Kurucz model atmospheres and spectra are discussed in detail in Chapter 3.

The automatic methods used to do the classification range from criterion evaluation, which conceptually is closest to what a human classifier would do, through to various machine learning methods such as artificial neural networks. To speed up, and sometimes improve the accuracy of the automatic classification process, some kind of dimensionality reduction is often done. A stellar spectrum contains a lot of information, not all of which is necessary for classification (for example, some of it is noise). Human classifiers automatically 'remove' the unnecessary information, for example they might measure some line indices and ignore the rest of the spectrum. However, when using an automatic method of classification, you also need an automatic way of extracting the useful information from a spectrum. One method for doing this which has been used quite extensively in astronomy is principal component analysis (PCA), which I will discuss in Section 2.4.2. In Section 2.4.1 I experiment with wavelet

analysis, which has been used less than PCA but also shows potential as a useful technique for this application. An alternative to these mathematical based techniques is to measure specific absorption lines in the spectra. Although I do not experiment with this for classifying stellar spectra I do use the Lick indices when considering galaxy spectra in Chapters 4 and 5. The principles of machine learning and the specific methods used will be described in Section 2.3.

Using state-of-the-art machine learning techniques could have a significant impact on many areas of astronomy that extract information from large quantities of data. There are many machine learning techniques available that perform well on a range of standard tests, that are yet to be applied to astronomy problems. These methods will be crucial as the size of the datasets increase. One such technique is Support Vector Machines, which I will discuss in Section 2.7. These have not been used extensively in astronomy and yet have been shown to outperform neural networks in many standard machine learning tasks.

2.2 Stellar classification systems

2.2.1 The MKK classification system

The MKK system (named after its developers, Morgan, Keenan and Kellman) provides a way of classifying stars into discrete boxes, based on properties that are essentially continuous. It was initially defined in Morgan et al. (1943) and subsequently revised by Johnson and Morgan (1953) and then by Morgan and Keenan (1973). A key feature of the system is that it is not based on any specific properties of the spectra, but the overall appearance, taking into account the lines, blends and bands in the ordinary photographic region (Morgan and Keenan, 1973). The aim of the MKK system was to classify the stars based solely on their spectral features with respect to a set of standards. This has the advantage of avoiding any dependence on other factors, such as calibration, photometry or theory, hence making it robust against changes in any of those areas.

When the MKK system was first defined, photographic emulsions were only sensitive to

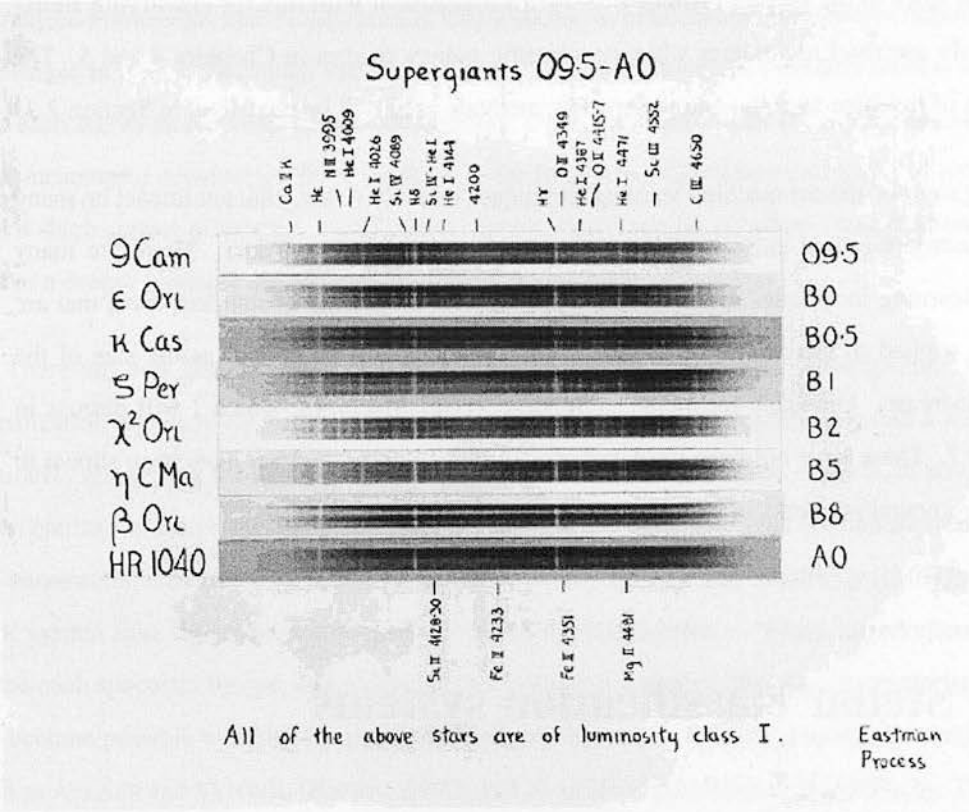

Figure 2.1: Examples of the spectra used to define the MKK system. Image source: (Morgan et al., 1943), also available online at NASA's Level 5.

the blue-violet region of the spectrum. As a result, the MKK system was defined based on that region. This has turned out to be particularly useful region as there is a high density of important atomic lines and molecular bands. Figure 2.1 shows some spectra used to define the MKK standards. Almost all modern classification is done using one-dimensional spectra rather than these two dimensional ones. Two spectral atlases published in the late 1970's (Keenan and McNeil, 1976; Morgan et al., 1978) summarise the MKK system up to that point. Since the publication of these atlases there have been many refinements and extensions of the MKK system. For example Gray (1989) extended the system to metal-weak F and G type stars and Henry et al. (1994) and Kirkpatrick et al. (1995) extended the system to very cool stars (M type and L type dwarfs). A summary of the modern MKK classification system standards is given in 'A Digital Spectral Classification Atlas' by R. Gray[1].

[1]Available as part of NASA's Level5 (`http://nedwww.ipac.caltech.edu/level5/`).

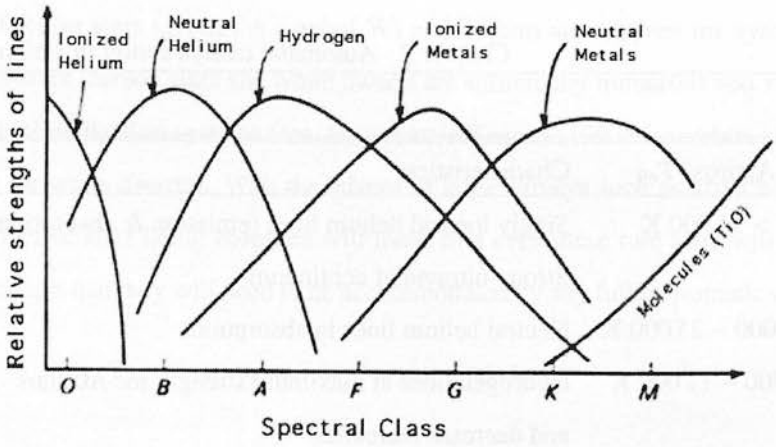

Figure 2.2: How the strength of the major lines changes with MKK spectral type. Image source: `http://lheawww.gsfc.nasa.gov/users/allen/stellar_lines.gif`

The MKK system is a two dimensional system, with the two parameters being spectral class and luminosity class. The spectral class ranges from O to M (with the famous mnemonic *Oh Be a Fine Guy/Girl Kiss Me*!). In the late 1800's Pickering and Fleming developed a classification scheme corresponding to Hydrogen line strength (A, B, C, ...). Later Annie Cannon realised that by rearranging the spectral types (O, B, A, ...) it was possible to obtain a system in which all the line strengths changed continuously. This formed the basis of the current MKK system. The spectral type essentially maps effective temperature, ranging from hot stars at O ($T_{\rm eff} > 25\,000$ K) to cool stars at M ($T_{\rm eff} < 3500$ K). Due to the remains of some now obsolete theories of stellar evolution, the hot stars (O, B and A) are sometimes referred to as early spectral types and the cool stars (G, K and M) as late spectral types. Each spectral class is divided into 10 subclasses, labelled from 0 to 9 (*i.e.* A0, A1, ..., A9) to allow for finer grained classifications. Figure 2.2 shows roughly how the abundances of several major lines change with spectral type and Table 2.1 outlines some basic properties of stars in each of the main classes. It is evident from Figure 2.2 that the rate of change of line strengths with spectral class is not uniform, so the error in classifying a star will depend on its class and subclass. The non-uniformity in the spectral class as a function of the physical properties of a star complicates the evaluation of the success of any classification scheme. The second parameter in the MKK system is the luminosity class which reflects how the shape and strength of certain lines change, and roughly corresponds to the surface gravity of the stars. The luminosity class ranges from

Type	Approx. T_{eff}	Characteristics
O	> 25 000 K	Singly ionised helium lines (emission & absorption). Strong ultraviolet continuum.
B	11 000 – 25 000 K	Neutral helium lines in absorption.
A	7500 – 11 000 K	Hydrogen lines at maximum strength for A0 stars and decrease thereafter.
F	6000 – 7500 K	Metallic lines become noticeable.
G	5000 – 6000 K	Solar-type spectra. Absorption lines of neutral metallic atoms and ions grow in strength.
K	3500 – 5000 K	Metallic lines dominate. Weak blue continuum.
M	< 3500 K	Molecular bands of titanium oxide noticeable.

Table 2.1: General properties of O–M stars.

Class	Description
Ia	Most luminous supergiants
Ib	Less luminous supergiants
II	Luminous giants
III	Normal giants
IV	Subgiants
V	Main sequence stars (dwarfs)

Table 2.2: Luminosity classes in the MKK system.

Ia for luminous supergiants to V for main sequence stars or dwarfs. The full scheme is shown in Table 2.2. So the full MKK classification of a spectrum is of the form G2V (for the sun).

One of the modern extensions to the system is the inclusion of peculiar types of stars. If the spectrum of a particular star mostly resembles that of a normal star, but with some peculiarities or irregularities, it is given a normal classification, plus a 'peculiarity code'. For example, 'e' indicates the presence of emission lines (usually hydrogen) and 's' indicates very narrow (sharp) lines. There are also stars with distinct spectra that are given separate classifications

such as Wolf-Rayet stars (given the symbol W) and T-Tauri stars (given the symbol T). Two other types of stars, carbon stars and white dwarfs are sufficiently numerous and varied to have their own sub-classification systems (see, for example Keenan (1993) for carbon stars and Sion et al. (1983) for white dwarfs). With the advent of large surveys such as SDSS and GAIA, the massive number of stars being observed will mean that even these rare stars will be observed frequently enough that they will need to be accommodated by any fully automatic classification system.

2.2.2 Physical parameterisation

Physical parameterisation is the process of determining the physical properties of a star from its spectrum. This is in contrast to the MKK system in which no deliberate physical links were made in determining the classification scheme. Each spectrum is classified with three parameters: effective temperature, ($T_{\rm eff}$), surface gravity ($\log(g)$) and metallicity ([M/H]). These parameters determine the structure of the stellar atmosphere, and hence the spectrum of the star.

Effective temperature is a measure of how much energy is emitted through a unit area of the star's surface and is defined as

$$T_{\rm eff} \equiv \left(\frac{L}{4\pi R^2 \sigma}\right)^{\frac{1}{4}} \tag{2.1}$$

where L is the luminosity of the star, R is the radius and σ is the Stefan-Boltzmann constant [2]. As a result, the effective temperature determines the shape of the continuum and, to a large extent, what absorption features are present in the spectrum. It is roughly equivalent to the spectral class in the MKK system. *Surface gravity* determines the pressure gradient in the star's atmosphere and hence at what densities spectral lines are formed. It is defined as

$$g \equiv \frac{GM}{R^2} \tag{2.2}$$

where M is the mass of the star, R is the radius and G is the gravitational constant [3]. The main effect of the surface gravity is the strength of the absorption features. It is roughly equivalent

[2] $\sigma = 5.6703 \times 10^{-8} \mathrm{Wm^{-2}K^{-4}}$

[3] $G = 6.672 \times 10^{-11} \mathrm{m^3 kg^{-1} s^{-2}}$

to the luminosity class in the MKK system. *Metallicity* is an approximation for the chemical composition of the stellar atmosphere, which determines the relative strengths of the spectral lines of atomic and molecular species present. Often one particular metal (usually Iron) is used to estimate this, in which case the symbol used for metallicity is [Fe/H]. Specifically, [Fe/H] is defined as the base 10 logarithm of the abundance of Fe relative to H (by mass) in the atmosphere, relative to the solar abundance. Metallicity is not explicitly dealt with by the MKK system.

Crucial to physical parameterisation is being able to measure the parameters empirically, at least for some stars. The fundamental parameter is the stellar radius because for a given mass it determines the surface gravity and for a given luminosity it determines the effective temperature. To measure radii we need to measure the angular diameter and distance to the star. One way of doing this is using intensity interferometry as done by Hanbury Brown et al. (1974) with the Narrabri interferometer. This technique can only be used for close, hot stars and as a result, the main resource for empirical angular diameters is their catalogue of 32 stars. These primary stars are then used to calibrate systems for calculating $T_{\rm eff}$, such as the Infra-red Flux Method (Blackwell et al., 1979), resulting in a larger catalogue of semi-empirically determined physical parameters. The larger catalogues can then be used to calibrate synthetic spectra such as the Kurucz (1992) spectra. The most commonly quoted stellar effective temperatures have been determined by comparison of the spectrum with the grid of Kurucz (1992) spectra, as distinct from a true effective temperature defined from Equation 2.1 with separately measured luminosity and radius. These Kurucz spectra are discussed in detail in Chapter 3.

The effective temperature scale (*i.e.* the relationship between physical parameters and MKK spectral types) has been studied by a number of people. A good summary of the methods used to determine the effective temperature scale is given by Boehm-Vitense (1981). One often cited comparison is that of Schmidt-Kaler (1982), part of which is shown in Table 2.3. Physical parameterisation has several advantages over the MKK system. It is in three dimensional parameter space, which means that changes in the spectrum can be isolated more easily. It allows a more specific classification, since the parameters are continuous, rather than the discrete MKK classes. It is more suited to automatic classification, as once a grid of synthetic spectra has been calibrated they are a valuable resource as template spectra. For these reasons, a lot

SpT	$T_{\rm eff}$ (V)	$T_{\rm eff}$ (III)	$T_{\rm eff}$ (I)	SpT	$T_{\rm eff}$ (V)	$T_{\rm eff}$ (III)	$T_{\rm eff}$ (I)
O3	52 000	50 000	47 300	A5	8 200	8 100	8 510
O5	44 500	42 500	40 300	F0	7 200	7 150	7 700
O7	38 000	37 000	35 700	F5	6 440	6 470	6 900
O9	33 000	32 000	32 600	G0	6 030	5 850	5 550
B0	30 000	29 000	26 500	G2	5 860	5 450	5 200
B2	22 000	20 300	18 500	G5	5 770	5 150	4 850
B3	18 700	17 100	16 200	K0	5 250	4 750	4 420
B5	15 400	15 000	13 600	K5	4 350	3 950	3 850
B7	13 000	13 200	12 200	M0	3 850	3 800	3 650
B8	11 900	12 400	11 200	M5	3 240	3 330	2 800
A0	9 520	10 100	9 730	M8	2 640		

Table 2.3: The effective temperature scale: relationship between the MKK spectral classes and $T_{\rm eff}$ for three different luminosity classes. The left hand column is for dwarf stars, the middle column for giants and the right hand column for supergiants. All temperatures are in Kelvin.

of modern classification work is focused on obtaining the physical parameters of spectra rather than the MKK classes.

2.3 Classification methods

To solve a problem like stellar classification, the most intuitive approach for an astronomer is probably to design an algorithm that measures different features in a spectrum and makes some decision about its type based on pre-defined criteria. The ideal program of this type would mimic a human classifier in as much detail as possible — an arbitrary number of rules could be added to the process. The difficulty with this approach is that it is hard to establish exactly what process a human does follow when classifying spectra.

This problem is not unique to stellar classification, similar problems are found in other

areas of astronomy (*e.g.* removal of artifacts from images, determining galaxy morphology), other sciences (*e.g.* detecting abnormal heartbeats on diagnostic screens) and business (*e.g.* face recognition, postcode recognition). There are many things that humans are so expert at that we can do without thinking, or do fairly easily after some degree of training, and yet are very hard to convert into a computer algorithm. The field of computer science that deals with this kind of problem is called machine learning. Machine learning is basically about designing systems which improve their performance through some kind of 'learning' process. There are two types of systems, *supervised*, in which the program has a set of pre-classified objects to work with, and *unsupervised* in which the program discovers possible classes working only from the raw data. Since stellar spectra already have well defined classes, the methods used in this chapter will all fall into the category of supervised machine learning.

Regardless of what specific type of machine learning method is used (*e.g.* decision trees, artificial neural networks) the general method of applying them is similar. The initial data is a large set of unclassified objects. Crucial to supervised learning is that there is also a (much smaller) set of objects for which the classifications are known. These objects form the training and testing sets. First the system is *trained* by giving it the raw inputs (in our case, the spectra) and their corresponding classes. The training set consists of a subset of the known spectra. Using a different subset of the known spectra, the system is then tested and some measure of its accuracy obtained. By changing some of the systems parameters, and repeating this process, a good set of parameters is found for the problem. After this fine-tuning, the system is then applied to the unknown spectra. In the rest of this section I will discuss the different methods that have been used for stellar spectral classification.

2.3.1 Criterion evaluation

It is widely recognised that humans are exceptionally good pattern matchers, far better than any current automatic techniques. The human classifier generally uses criterion evaluation. In the context of stellar classification, this involves choosing specific properties of the spectra that appear to be good at distinguishing between different types. For example, the ratio of HeI to HeII lines is used to distinguish between O type stars (Morgan and Keenan, 1973). The

largest homogeneously classified group of stellar spectra is the Michigan Catalogue (currently 5 volumes, the latest being Houk and Swift, 1999), which have been classified by Houk and co-workers over the last 30 years. Houk's internal error is estimated to be 0.44 subtypes (Houk, 1979), which sets a limit to what automatic techniques can achieve.

It is not surprising that some of the early attempts at automatic classification used criterion evaluation techniques. West (1973) outlines a system for automatically classifying objective prism spectra and suggests some useful criteria: line depths, line-depth ratios, peak heights, equivalent widths and absence/presence of specific features. Zekl (1982) and Malyuto (1984) both experimented with criteria evaluation, using line-depth ratios and equivalent widths.

Since these methods involve selecting only a small amount of data to use for comparison, they are computationally fast. However, selecting which criteria to use and measuring them in a standard way can be a problem. Also the techniques do not automatically extend to other wavelength regions, since new criteria have to be chosen. In some ways it seems this method should best reflect the way that humans perform the classification. However, it is not always clear — even to expert human classifiers — exactly how they make their final decision. This is the problem that most machine learning methods are trying to overcome.

2.3.2 Minimum distance methods

The minimum distance method (MDM) approach is probably the simplest machine learning method. It involves comparing a set of unknown spectra to a set of known spectra and choosing the closest match. One advantage of this approach is that no training is needed, as the 'training set' is the set of templates, kept throughout the process. However, to be successful it requires the training data to be dense in each parameter being classified (in particular, it is important that each subtype is represented).

Early research by Kurtz (1982) found that weighted metric distance methods were quite successful. The general metric distance between an unknown spectrum S_i and a template

spectrum T_i is given by

$$d_{ST} = \frac{1}{n} \sum_i \alpha^2(i)(S_i - T_i)^2 \tag{2.3}$$

where $\alpha(i)$ is a chosen weighting and n is the number of spectral points (pixels). When $\alpha(i) = 1$ then the equation reduces to the usual Euclidean metric distance. Kurtz initially found setting $\alpha(i) = \sigma(i)$, the variance of pixel i over the set of templates, to be effective, since the most weight is given to the pixels carrying the most information. In 1984 Kurtz proposed an improved weighting factor

$$\alpha^2(i) = \frac{\Sigma^2(i) - \sigma^2(i)}{\sigma^2(i)} \tag{2.4}$$

where Σ is the variance for each pixel calculated across the set of, for example, G stars and σ is calculated across the set of, for example, G2 stars. This weighting has the effect of selecting out those features that vary most across the larger group, but are very similar within the final class. For example Kurtz classified a sample of B type stars into subtypes with a mean error of 2.19 subtypes using the basic Euclidean distance. This improved to a mean error of 1.14 subtypes when using the weighting given in Equation 2.4 (Kurtz and Lasala, 1991).

Minimum distance methods have the advantage that the results are easy to interpret physically. However, they can be hard to apply to multi-parameter problems (such as classification in both spectral type and luminosity class). Since every unknown has to be compared with every template spectrum and there needs to be a template representing every possible classification, this method can be quite slow computationally. Bailer-Jones (2001) suggests it would be prohibitively slow to classify a large group of spectra in, say, five parameters.

2.3.3 Artificial neural networks

Most of the recent attempts to automatically classify stellar spectra have used artificial neural networks (ANN). For example Weaver and Torres-Dodgen (1997), Singh et al. (1998) and Bailer-Jones et al. (1998a) have used them, with varying degrees of success. The most successful result has been from the work of Bailer-Jones et al. (1998a) who achieved an accuracy of $\sigma = 1.09$ subtypes using his own neural network software package, `statnet`[4]. Neural

[4]Available from `http://www.mpia-hd.mpg.de/homes/calj/statnet.html`

networks are flexible tools, used in a wide range of fields on a very diverse set of applications. For an introduction or review of the theory of neural networks, see Bishop (1995). For a review of their application to astronomy problems, specifically stellar spectral classification, see Bailer-Jones (2001).

The original artificial neural network algorithms were designed as simple models of brain function. The purpose of the neural network is to learn the relationship between some input data and its parameters. The network relies on intrinsic properties and patterns in the data, rather than externally constructed rules. Neural networks consist of a series of layers, each with a chosen number of nodes and connections between the nodes. The process of classifying with neural networks involves firstly training the network on a set of known spectra. Neural networks can be quite slow to train (*i.e.* adjusting node connections to optimise successful classification of training data), but are fast to apply, which is an advantage since the training only needs to be done once (provided the training set is chosen carefully). They can cope well with nonlinear trends in the sample, and can recognise intraclass and interclass differences.

Every source in the training set affects the classification of all of the other sources, and so it is important that the distribution of frequencies of objects in this training set is realistic. This can be a problem if the expected distribution is unknown. Also, neural networks are not as robust at dealing with missing data as some of the other methods. I believe that the main disadvantage of neural networks at the moment is the fine tuning required to get the best result. There are many parameters that have to be chosen, such as: number of layers, number of nodes in each layer, when to stop training and how to weight the nodes, just to name a few. The performance of the neural network can be very sensitive to some or all of these parameters, as well as the exact nature of the training data. However, they have produced the best results so far, and so are very important for automatic classification of stellar spectra.

2.3.4 Principal component analysis

PCA has mainly been used as a method for data compression (discussed later in Section 2.4), reducing the data to a number of principal components before applying a neural network. How-

ever, there have been some attempts to use PCA directly as a classification method. Whitney (1983) classified 53 A and F type stars by doing a linear fit to the 3 most significant principal components. The accuracy of the classification proved to be no worse than when all 47 data points were used. Ibata and Irwin (1997) classified 1500 K stars into the discrete classes 'giants' and 'dwarfs'. For the highest S/N spectra their success rate was about 90 – 95% but the limited nature of this work makes it hard to compare with other methods.

PCA has the advantage of being a relatively fast procedure that can also account for incomplete spectra by projection onto the eigenvectors. Since the principal components themselves often have ambiguous physical interpretations, they are probably more suited to data compression, rather than as a direct classification method.

2.4 Dimensionality reduction techniques

Automatic classification of astronomical sources is essential in the age of surveys such as SDSS and GAIA — clearly a computer can perform many tasks much faster than a human. However, even a relatively fast procedure (such as calculating correlation coefficients) can become impractical when applied to a million spectra.

Data compression can be used to significantly speed up the required calculations by reducing the number of dimensions needed to describe each spectrum. When compressing the data it is crucial that the important information in the spectrum is retained. Not all of the information available may be useful or necessary for classification and some of it is almost certainly not (*e.g.* noise). For example, when people classify stars, they select a certain number of features which are measured, as well as looking at the overall spectrum. We could do the same type of thing within the machine learning paradigm, select a small number of features, measure them and then make these inputs to the system. However, there are several disadvantages to this. Firstly deciding which features to use immediately adds an interactive element to classification. Secondly, although there are standard absorption features that human classifiers measure, there is no clear way of taking into account the overall feeling they have about the spectrum.

In this section I explain the principles behind the two methods of dimensionality reduction that I use in this thesis; wavelet analysis and principal component analysis.

2.4.1 Wavelet analysis

In the last decade wavelets have become a popular tool for many astrophysics problems covering a wide range of areas from analysis of time-varying phenomena such as solar bursts (Giménez de Castro et al., 2001) to analysis of clustering and substructure in interstellar clouds (Langer et al., 1993). The wavelet transform is similar to the Fourier transform in that it allows a function, $f(\lambda)$, to be represented by a set of orthonormal basis functions, $\psi_{jk}(\lambda)$

$$f(\lambda) = \sum_{j=-\infty}^{\infty} \sum_{k=-\infty}^{\infty} d_{jk} \psi_{jk}(\lambda) \tag{2.5}$$

where d_{jk} are the wavelet coefficients. However, unlike the Fourier transform (which is spatially infinite), the wavelet function is localised in space (or time) and frequency, making it more efficient at representing discontinuities in the signal, or frequency behaviour that varies with time.

Every basis function within a given wavelet family $\psi_{jk}(\lambda)$ is obtained from a mother wavelet $\psi(\lambda)$ (Figure 2.3) by shifting and scaling using the following formula

$$\psi_{jk}(\lambda) = 2^{j/2} \psi(2^j \lambda - k) \tag{2.6}$$

where j and k are the scaling and shifting parameters respectively. This dual localisation in space and frequency means that wavelets can be used as a probe to determine the scale that the information is carried on. Some of the wavelet coefficients pick up fine structure in the spectra (such as noise) while others detect the coarser structure (such as changes in the shape of the continuum). It also results in many functions having a sparse representation to a high level of accuracy, when transformed into the wavelet domain. Within a class of wavelets (such as Daubechies or Haar wavelets) there are a range of different mother functions (Figure 2.3). Depending on the application, a function that is highly localised (compact) or one that is very smooth may be preferred. The Daubechies wavelets have proved to be particularly useful for signal compression and for representing discontinuities in the signal (Meyer, 1993). Throughout this thesis I will be using the Daubechies wavelet of order 20.

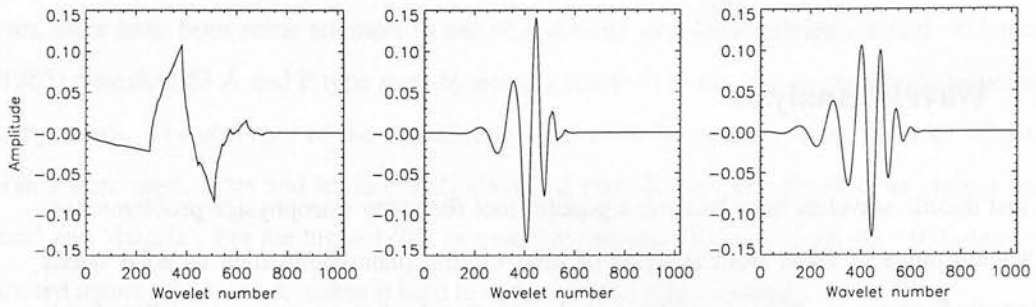

Figure 2.3: Three examples of wavelet mother functions from the Daubechies family. These were created by inverse transforming a delta function. Left: Daubechies 4. Centre: Daubechies 12. Right: Daubechies 20.

The *wavelet coefficients* d_{ij} given by Equation 2.5 are actually linear superpositions of the *fundamental coefficients* that define the wavelets (this will be demonstrated in Equation 2.9). It is important to make the distinction between these two sets of coefficients, and so in this section I will refer to each explicitly. However, in the rest of this thesis, the term *coefficients* will mean d_{ij} — the result of doing a wavelet transform.

A set of wavelets can be specified by a matrix of its fundamental coefficients and forms the basis of the Discrete Wavelet Transform (DWT). The most compact Daubechies wavelet is of order 4 and so has four fundamental coefficients, c_0, c_1, c_2, c_3 which form a matrix

$$\begin{bmatrix}
c_0 & c_1 & c_2 & c_3 & & & & & & & & \\
c_3 & -c_2 & c_1 & -c_0 & & & & & & & & \\
 & & c_0 & c_1 & c_2 & c_3 & & & & & & \\
 & & c_3 & -c_2 & c_1 & -c_0 & & & & & & \\
\vdots & \vdots & & & & & \ddots & & & & & \\
 & & & & & & & c_0 & c_1 & c_2 & c_3 & \\
 & & & & & & & c_3 & -c_2 & c_1 & -c_0 & \\
c_2 & c_3 & & & & & & & & c_0 & c_1 & \\
c_1 & -c_0 & & & & & & & & c_3 & -c_2 &
\end{bmatrix} \tag{2.7}$$

By using the fact that the above matrix is orthogonal, and by requiring that the sequence $c_3, -c_2, c_1, -c_0$ has a certain number of vanishing moments, the values of the fundamental

coefficients can be calculated. For the Daubechies 4 wavelets, these have the values

$$\begin{aligned} c_0 &= (1+\sqrt{3})/4\sqrt{2} \quad & c_1 &= (3+\sqrt{3})/4\sqrt{2} \\ c_2 &= (3-\sqrt{3})/4\sqrt{2} \quad & c_3 &= (1-\sqrt{3})/4\sqrt{2} \end{aligned} \tag{2.8}$$

Values for different wavelets can be found in tables, for example in Daubechies (1988). The matrix is actually comprised of two filters (quadrature mirror filters) which perform different operations when applied to the data. The output of the first filter (c_0, c_1, c_2, c_3) is the smooth information about the data. The output of the second filter $(c_3, -c_2, c_1, -c_0)$ is the detail information about the data. So one application of matrix 2.7, to a data vector of length 8 gives a vector of interleaved smooth (s) and detailed (d) components

$$\begin{bmatrix} c_0 & c_1 & c_2 & c_3 & & & & \\ c_3 & -c_2 & c_1 & -c_0 & & & & \\ & & c_0 & c_1 & c_2 & c_3 & & \\ & & c_3 & -c_2 & c_1 & -c_0 & & \\ & & & & c_0 & c_1 & c_2 & c_3 \\ & & & & c_3 & -c_2 & c_1 & -c_0 \\ c_2 & c_3 & & & & & c_0 & c_1 \\ c_1 & -c_0 & & & & & c_3 & -c_2 \end{bmatrix} \begin{bmatrix} x_1 \\ x_2 \\ x_3 \\ x_4 \\ x_5 \\ x_6 \\ x_7 \\ x_8 \end{bmatrix} = \begin{bmatrix} s_1 \\ d_1 \\ s_2 \\ d_2 \\ s_3 \\ d_3 \\ s_4 \\ d_4 \end{bmatrix} \tag{2.9}$$

However this has only operated on one resolution level — extracting the 2^{N-1} wavelet coefficients that represent the finest structure. To access the next resolution level the matrix must be reapplied to the smoothed data. This is done hierarchically using the pyramid algorithm, separating the detail coefficients at each stage (by rearranging the vector), and reapplying the matrix to the remaining smooth coefficients. In this way, the number of smooth coefficients is reduced by a factor of two each time, until two final smooth coefficients are left, the mother-function coefficients. Hence the resulting vector consists of 2 residual smooth coefficients and $2^N - 2$ wavelet coefficients, d_{ij}, and is the same length as the input data vector. In the case of the above example, only one more application is needed. In this thesis I calculate the DWT using the pyramid algorithm given in Press et al. (1992) and shown in Equation 2.10.

$$\begin{bmatrix} x_1 \\ x_2 \\ x_3 \\ x_4 \\ x_5 \\ x_6 \\ x_7 \\ x_8 \end{bmatrix} \xrightarrow[\text{8x8 matrix}]{\text{apply}} \begin{bmatrix} s_1 \\ d_1 \\ s_2 \\ d_2 \\ s_3 \\ d_3 \\ s_4 \\ d_4 \end{bmatrix} \xrightarrow{\text{rearrange}} \left[\begin{array}{c} s_1 \\ s_2 \\ s_3 \\ s_4 \\ \hline d_1 \\ d_2 \\ d_3 \\ d_4 \end{array}\right] \xrightarrow[\text{4x4 matrix}]{\text{apply}} \left[\begin{array}{c} S_1 \\ D_1 \\ S_2 \\ D_2 \\ \hline d_1 \\ d_2 \\ d_3 \\ d_4 \end{array}\right] \xrightarrow{\text{rearrange}} \left[\begin{array}{c} S_1 \\ S_2 \\ \hline D_1 \\ D_2 \\ \hline d_1 \\ d_2 \\ d_3 \\ d_4 \end{array}\right] \tag{2.10}$$

To help visualise this, Figure 2.4 shows an example of applying the DWT to a sine function and a slightly modified sine function. Comparing the two show how the wavelet transform probes structure on different scales. In both there are high amplitude wavelet coefficients at low wavelet numbers. These are caused by the sine curve itself. In the pure sine curve there is no structure at finer levels than this, and hence all the high wavelet numbers are zero. However, the transform of the modified curve shows some lower amplitude wavelet coefficients representing the fine scale structure — in this case caused by the spike. Wavelet coefficients not only detect what frequencies are present, they also record the position of the various features at each resolution scale.

Data compression

Many applications of wavelets are related to the fact that they can be used to compress data while still retaining most of the important information. The classification processes used in this thesis have linear time dependence on the number of data points. Hence, by using wavelets to compress the data by a factor of 10, the time it takes to classify each spectra can potentially be reduced by a factor of 10.

The power of wavelets as a method of data compression can be demonstrated using a typical stellar spectrum, as shown in the left panel of Figure 2.5. The wavelet transform is shown in the right panel. It is obvious that most of the coefficients are close to (although not equal to) zero, with most of the information being contained in a small number of coefficients. Truncating the vector of wavelet coefficients (keeping only the 10% of the coefficients with the highest

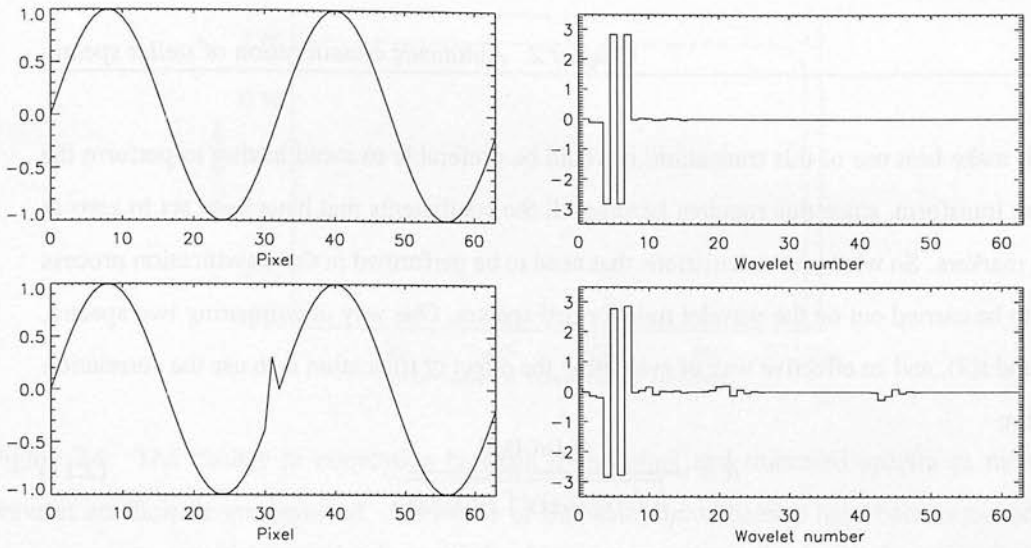

Figure 2.4: Top: A 64 data point sine curve, and its wavelet transform. Bottom: The same sine curve, modified by adding a spike, and its wavelet transform.

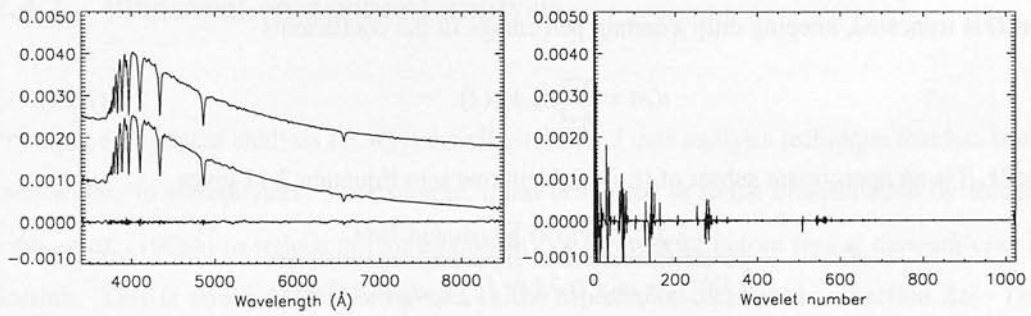

Figure 2.5: Left: A 1024 pixel section of an A0V stellar spectrum from the Pickles (1998) catalogue (top) and below it, the spectrum created by inverse transforming the truncated wavelet coefficient vector (for clarity the spectrum has been shifted on the y-axis). The bottom line is the difference spectrum. Right: The wavelet transform of the spectrum. The low coefficient numbers represent information at coarsest levels, and the high coefficient numbers represent the finest structure.

absolute value and setting the rest to zero) and performing the inverse DWT results in the lower spectrum in Figure 2.5. The truncated spectrum is remarkably close to the original, as shown by the difference spectrum.

To make best use of this truncation, it would be preferable to avoid having to perform the inverse transform, since this requires keeping all the coefficients that have been set to zero as place markers. So what ever calculations that need to be performed in the classification process need to be carried out on the wavelet transformed spectra. One way of comparing two spectra, $f(\lambda)$ and $t(\lambda)$, and an effective way of evaluating the effect of truncation is to use the correlation function

$$R = \frac{\int f(\lambda)t(\lambda)d\lambda}{\sqrt{(\int f^2(\lambda)d\lambda)(\int t^2(\lambda)d\lambda)}} . \tag{2.11}$$

The two spectra, $f(\lambda)$ and $t(\lambda)$ can be represented by their wavelet decompositions

$$f(\lambda) = \sum_{i,j} c_{ij}\psi_{ij}(\lambda) \tag{2.12}$$

$$t(\lambda) = \sum_{i,j} d_{ij}\psi_{ij}(\lambda) . \tag{2.13}$$

Now $t(\lambda)$ is truncated, keeping only a certain percentage of the coefficients

$$t(\lambda) = \sum_{k,l} d_{kl}\psi_{kl}(\lambda) \tag{2.14}$$

so that $\{k, l\}$ is an appropriate subset of $\{i, j\}$. Substituting into Equation 2.11 gives

$$R = \frac{\int \sum_{i,j} c_{ij}\psi_{ij}(\lambda) \sum_{k,l} d_{kl}\psi_{kl}(\lambda)d\lambda}{\sqrt{(\int(\sum_{i,j} c_{ij}\psi_{ij}(\lambda))^2 d\lambda)(\int(\sum_{k,l} d_{kl}\psi_{kl}(\lambda))^2 d\lambda)}} \tag{2.15}$$

$$= \frac{\sum_{i,j}\sum_{k,l} c_{ij}d_{kl}\int \psi_{ij}(\lambda)\psi_{kl}(\lambda)d\lambda}{(\sum_{i,j} c_{ij})^2(\sum_{k,l} d_{kl})^2} \tag{2.16}$$

but since the wavelets are an orthogonal set,

$$\int \psi_{ij}(\lambda)\psi_{kl}(\lambda)d\lambda = \delta_{ik}\delta_{jl} \tag{2.17}$$

which implies

$$R = \frac{\sum_{kl} c_{kl}d_{kl}}{(\sum_{i,j} c_{ij})^2(\sum_{k,l} d_{kl})^2} . \tag{2.18}$$

This shows that calculating the correlation before and after the wavelet transform are equivalent. Also, the calculations are only performed on the selected percentage of coefficients, significantly speeding up the process. Figure 2.6 shows the auto-correlation coefficient versus the percentage of wavelet coefficients removed (each time the auto-correlation coefficient is calculated using the truncated spectrum and the original spectrum.) It is clear from this Figure that the spectrum can be highly compressed before there is any significant effect on its appearance.

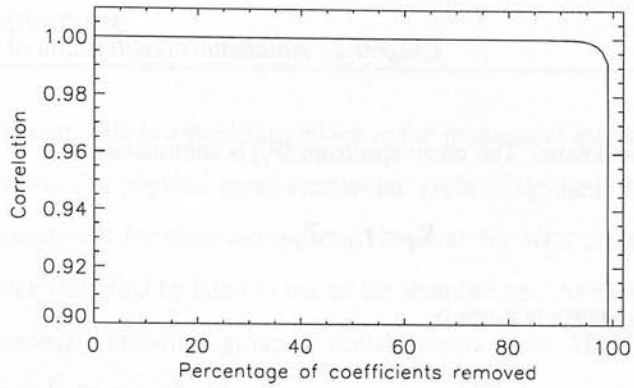

Figure 2.6: The change in correlation between the original and truncated spectra as more wavelet coefficients are removed. After 60% of the wavelet coefficients have been removed, the correlation with the original spectrum is still near perfect. It only decreases significantly after around 90% have been removed.

2.4.2 Principal component analysis

Principal component analysis (PCA) is a well established data analysis technique that has been used widely in astrophysics. For example, it has been used in stellar classification by Bailer-Jones et al. (1998a) to reduce the dimensionality of the spectra before neural network classification. This is how I will be using PCA in the experiments described in Section 2.6. The discussion in this section is based on that in Murtagh and Heck (1987) and Folkes et al. (1999).

PCA is a process that transforms a large number of possibly correlated variables into a set of uncorrelated variables. Most of the original information is contained in a small number of these independant variables and so it provides a way of representing a large amount of data with a few variables. We can see a set of n spectra, each of length m as an $n \times m$ array of data. For a typical set of say, $n \sim 10\,000$ of spectra, each with say, $m \sim 1000$ pixels (called attributes or variables), we are dealing with a very high dimensional dataset. PCA aims to find the best summarisation of this data.

Let us call the $n \times m$ matrix $X = \{x_{ij}\}$ where i is a spectrum (in $\Re^m$ space), and j is an attribute of a spectrum (in $\Re^n$ space). The first step is to find an axis which accounts for the

most variance within the dataset. The mean spectrum ($\bar{r}_j$) is subtracted

$$X_{ij} = r_{ij} - \bar{r}_j \tag{2.19}$$

and then the covariance matrix is given by

$$C_{jk} = \frac{1}{N} \sum_{i=1}^{N} X_{ij} X_{ik}, \quad 1 \leq j \leq M, 1 \leq k \leq M \tag{2.20}$$

Then the axis along which the variance is maximal is the eigenvector e_1, of C_1, which satisifies the equation

$$C_1 e_1 = \lambda_1 e_1 \tag{2.21}$$

where λ_1 is the largest eigenvalue (variance). The spectra are then projected onto this axis, and the process repeated to find the axis which accounts for the most variance. In this way, we obtain a set of eigenvectors and eigenvalues in order of what fraction of the variance they account for. The complete set of eigenvectors form a set of orthogonal axes which describe the dataset completely. Each spectrum is then projected onto n axes and the eigenvalue obtained is the nth principal component (PC). A spectrum can be reconstructed from, say, x principal components by

$$S_r = PC_1 e_1 + PC_2 e_2 + \ldots + PC_x e_x \tag{2.22}$$

In practice very few of the principal components are needed for a good reconstruction of the original spectrum, meaning a 1000 pixel spectrum can be represented by as few as 3 to 5 principal components, without much information loss. This makes it an excellent method of data compression.

2.5 The data

A crucial part of any supervised machine learning task is the availability of a pre-classified data set. Ideally the data should have dense coverage of the parameter space, *i.e.* it should represent all the types likely to be found in the real data. The data should be complete, *i.e.* each spectrum should be a full spectrum over the range of the real data. And it should be accurately classified as any mistakes will be applied to the real data, resulting in mis-classifications.

2.5.1 Data coverage

The lack of good training data is a stumbling block in the progress of automatic MKK classification of stellar spectra. For physical parameterisation, grids of synthetic spectra can be used directly to obtain parameters for observed spectra. However, for MKK classification, it is necessary to have spectra classified by hand to use as the template set. As mentioned previously, the largest homogeneously classified group of stellar spectra is the Michigan Henry Draper Catalogue, which has been classified by Houk and co-workers over the last 30 years. Until recently these have not been available as one dimensional spectra in a machine readable form. Hence typically people have used one of the following catalogues as template spectra.

Gunn-Stryker: The GS catalogue (Gunn and Stryker, 1983) consists of 175 spectra at a resolution of 20/pix. The spectra cover the wavelength range $\lambda = 3130 - 10\,800$.

Jacoby-Hunter: The JHC catalogue (Jacoby et al., 1984) consists of 161 spectra at a resolution of 4.5 /pix. The spectra cover the wavelength range $\lambda = 3510 - 7427$.

Silva-Cornell: The SC catalogue (Silva and Cornell, 1992) consists of 72 spectra at a resolution of 11 /pix. The spectra cover the wavelength range $\lambda = 3510 - 8930$.

Pickles: The Pickles catalogue (Pickles, 1998) consists of 131 spectra at a resolution of 5 /pix. The spectra cover the wavelength range $\lambda = 1150 - 10\,629$.

The spectral type distributions of the stars in each catalogue are shown in Figure 2.7. This figure clearly shows that the catalogues do not satisfy one of the major requirements of a stellar template library – good coverage in parameter space. This is particularly clear when you consider that these plots group stars of different luminosity classes together, and yet still have a small number of spectra in most spectral class bins. This adds an unavoidable error into the automatic classification process.

The importance of having a larger and more homogeneous library of pre-classified spectra for use in automatic classification has been recognised for some time. A big jump forward was made by Bailer-Jones et al. (1998b) who extracted a set of digital objective prism spectra from the Michigan catalogue. The plates were scanned in using the APM in Cambridge and

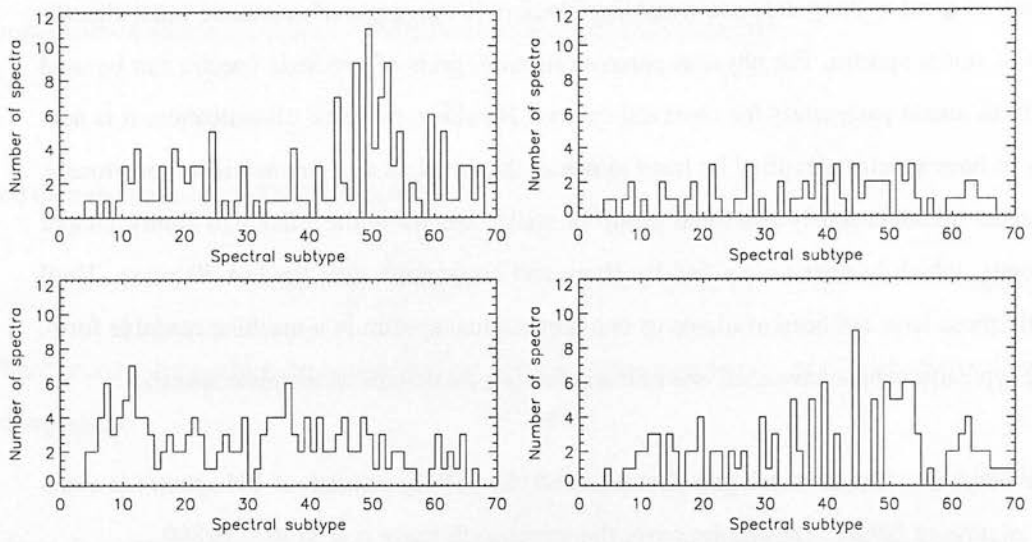

Figure 2.7: The distribution of spectral types in each catalogue. Where the catalogue classification covers more than one spectral subtype the average is used. The spectral classes are given a number ranging between 0 (for O0) to 69 (for M9). Top Left: GS. Top Right: SC. Bottom Left: JHC. Bottom Right: PI

the spectra then extracted into a one dimensional, machine readable format. The spectra are at a resolution of around 2 /pix and cover the wavelength range $\lambda = 3802 - 5186$. From the total of around 12 000 spectra extracted, Bailer-Jones has created a sample of 5219 high quality spectra for use in automatic classification which are now publicly available. The distribution of these sources in spectral type is shown in Figure 2.8. The number of spectra in each spectral subtype is typically an order of magnitude larger than what was previously available in the much smaller pre-classified datasets.

2.5.2 Data preparation

Dealing with missing data is an important part of making a classification system robust. A system must be able to detect spectra with missing data, and then correct for this. For example, the wavelet transform requires a data vector of 2^N pixels and hence it is necessary to interpolate over missing sections so that the number of pixels is correct.

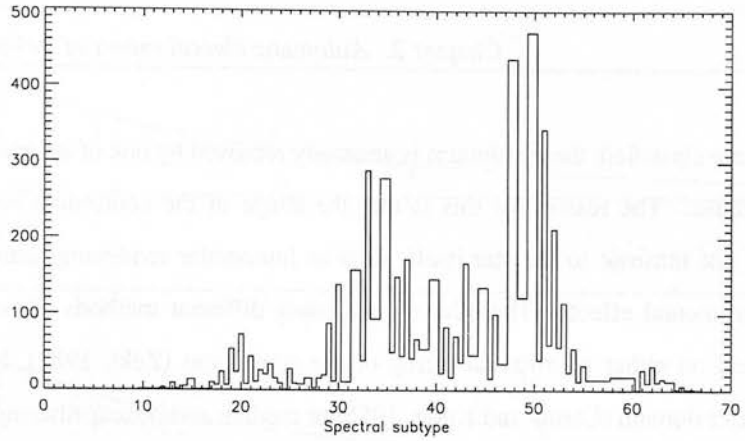

Figure 2.8: The distribution of spectral types in the Bailer-Jones catalogue. The spectral classes are given a number ranging between 0 (for O0) to 69 (for M9).

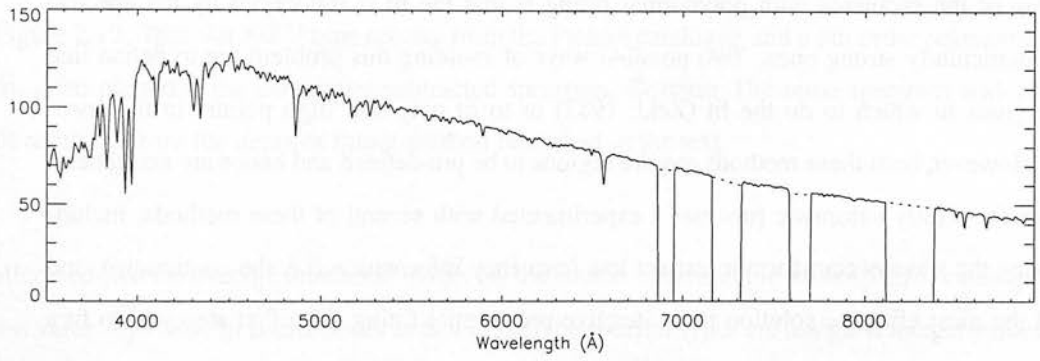

Figure 2.9: A F67V type spectra from the SC catalogue (solid line) with the dotted line showing the interpolated sections.

Some spectra in the GS and SC catalogues had missing data. In the SC catalogue this was systematic with four narrow regions missing from every spectrum. In the GS catalogue, only the occasional source had data missing. After some experimentation with these spectra I found that a simple straight line interpolation was a sufficient solution to this problem as it was much faster than a full polynomial interpolation, and did not significantly affect the results. An example is shown in Figure 2.9. Because the classification methods being used in this section do not depend on any specific spectral features, they are not significantly affected by small sections of missing data.

Before spectra are classified, the continuum is generally removed by one of several spectral rectification techniques. The reason for this is that the shape of the continuum is affected by factors that are not intrinsic to the star itself, such as interstellar reddening, atmospheric extinction and instrumental effects. There have been many different methods of continuum removal, most based on either polynomial fitting of the continuum (Zekl, 1982), high pass filtering in the Fourier domain (Lasala and Kurtz, 1985) or median and boxcar filtering (Bailer-Jones et al., 1998b). For the purposes of classification, the particular method of continuum subtraction chosen is not crucial, as long as it is consistent, and produces line spectra of similar quality across the range in spectral types being used.

One of the problems with polynomial fitting is that the fit is influenced by the spectral lines, particularly strong ones. Two possible ways of avoiding this problem are to define line free regions in which to do the fit (Zekl, 1982) or to fit only the 'high points' in the spectrum. However, both these methods require regions to be pre-defined and hence are not general enough for a fully automatic process. I experimented with several of these methods, including using the wavelet transform to extract low frequency information (*i.e.* the continuum), and found the most effective solution to be iterative polynomial fitting. The first step was to fit a 5th order polynomial to the spectrum. Then all points that fell below the fit, were set to be equal to the fit, and the process repeated. Iterating until the RMS error between the fit and the original data converged gave good results. Limiting the process to 5 iterations gave comparable results. Figure 2.10 shows the basic polynomial fit, and the improvement gained by iterating in this way. For the Bailer-Jones catalogue, the data are provided in two formats, the original spectra and a continuum subtracted version. The process used for continuum subtraction for that catalogue is discussed in detail in Bailer-Jones et al. (1998b).

2.5.3 The numbering of spectral types

When considering automatic classification results quoted in the literature, it is important to note that the way the spectral types are numbered is significant. In this work, I have assigned every spectral subtype a value, ranging from 0 to 69 and going up in increments of 1, as shown in Table 2.4. For cases where the spectral type given in the catalogue was a range the value

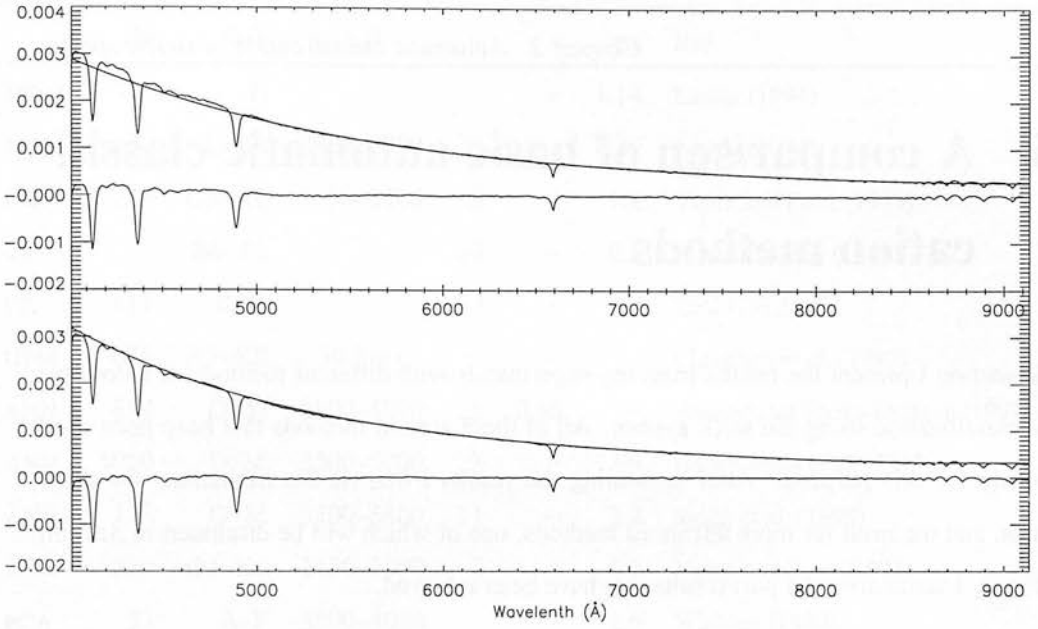

Figure 2.10: Top: An A0IV type spectra from the Pickles catalogue and a 5th order polynomial fit. Also plotted is the continuum-subtracted spectrum. Bottom: The same spectrum with the fit resulting from the iterative fitting method described in the text.

allocated was the average numerical value. So the source o7b1iii in the Silva-Cornell catalogue has value $\frac{7+11}{2} = 9$. In Bailer-Jones et al. (1998a) the spectral types are assigned integer values,

O1	O2	O3	···	B9	A9	F9	G9	K9	M9
1	2	3	···	19	29	39	49	59	69

Table 2.4: The numerical value assigned to each spectral subtype.

going up by one for each spectral type. However, when one subtype is missing the number still goes up by one. For example, if the type F7 was missing, F5, F6, F8 would be assigned 35, 36, 37 rather than 35, 36, 38 as in my numbering system. This results in different values for the quoted errors. For example, in the next section I obtain an error of $\sigma_{rms} = 2.43$ using basic correlation on the Pickles catalogue. Recalculating this using Bailer-Jones' numbering scheme gives an error of $\sigma_{rms} = 1.37$. This should be kept in mind when comparing the results in the next section.

2.6 A comparison of basic automatic classification methods

In this section I present the results from my experiments with different methods of automatic stellar classification using the MKK system. All of these are old methods that have been used previously for this purpose. After presenting the results I discuss the limitations for these methods, and the need for more advanced methods, one of which will be discussed in Section 2.7. Firstly I summarise the past results that have been achieved.

2.6.1 Summary of past results

The performance of each system is assessed using some form of error measurement based on the difference between the obtained classifications SpT_{ob} and the 'real' classifications SpT. To do this, a decimal value is assigned to each spectral subtype as described in Section 2.5.3. Then the RMS value of the residuals

$$\sigma_{RMS} = \sqrt{\frac{\sum(SpT_{ob} - SpT)^2}{n}} \tag{2.23}$$

or the mean absolute value of the residuals

$$\epsilon = \frac{1}{n}\sum |SpT_{ob} - SpT| \tag{2.24}$$

is used as a measure of the accuracy of the system. Table 2.5 shows a summary of results for various automatic stellar spectral classification methods. When looking at the quoted error, σ_{RMS}, it is important to note that only a few of these experiments have been carried out on spectra encompassing the full range of spectral types (namely Weaver and Torres-Dodgen, 1997; Bailer-Jones et al., 1998b; Singh et al., 1998). Limiting the sample, for example using only hot or only cool stars, generally results in a higher classification accuracy than when the whole range of O–M type spectra is used. Hence the most significant results are the ones that consider all main sequence stars from O–M. The current state-of-the-art system is `statnet`, which obtained a classification accuracy of $\sigma_{RMS} = 1.09$.

	N	SpT	λ ()		ϵ	σ	Ref
MDM	350	B			–	1.14	Lasala (1994)
MDM	80	F8–G8	3500–4800		–	0.4?	Lasala (1994)
MDM	229	O3–K0	1150–3200	2	–	1.4	Vieira and Ponz (1995)
CE		B0–F2		14	–	0.5	Schmidt-Kaler (1979)
CE	117	B–K		3	–	0.7	Zekl (1982)
GPM	671	A5–K0	10 lines	–	–	–	Christlieb et al. (1997)
ANN	817	O–M	5800–8900	15	0.56	–	Weaver and Torres-Dodgen (1997)
ANN	5000	O–M	3500–5200	3	–	1.09	Bailer-Jones et al. (1998b)
ANN	213	O–M	3500–6800	11	–	2.2	Singh et al. (1998)
ANN	229	O3–K0	1150–3200	2	–	1.1	Vieira and Ponz (1995)
PCA	53	A–F	3500–4000		–	1.6	Whitney (1983)
V					–	0.44	Houk (1979)

Table 2.5: Summary of classification results from the literature. *Column 1*: the general classification method used (MDM = Minimum Distance Method; CE = Criteria Evaluation; GPM = Gaussian Probabilistic Method; ANN = Neural Network; PCA = Principal Component Analysis; V = Visual). *Column 2*: the number of spectra used. *Column 3*: the range in spectral types used. *Column 4*: the wavelength range. *Column 5*: the sampling. *Columns 6 & 7* are given by equations 1.1 and 1.2 respectively. *Column 8* gives the references.

2.6.2 Correlation

The most straightforward approach is to correlate each spectrum with every template spectrum and then assign the unknown spectrum the class of the spectrum with the highest correlation coefficient. I then tested the effect of wavelet transforming the spectra and truncating the wavelet coefficient vector so as to speed up the classification process. To do this, I selected the n coefficients with the highest absolute value, and recalculated the correlation coefficient.

Minimum distance methods have no interpolation potential. In other words, a spectrum must be given the classification of one of the spectra in the template set. This is different to neural networks in which the class of the unknown spectrum can be found by interpolating

	GS		SC		JHC		PI		BJ	
	σ_{rms}	ϵ	σ_{rms}	ϵ	σ_{rms}	ϵ	σ_{rms}	ϵ	σ_{rms}	ϵ
100%	**3.79**	2.78	3.07	2.39	3.47	2.53	**2.29**	1.68	1.56	1.05
50%	3.89	2.83	**3.06**	2.36	**3.38**	2.47	2.35	1.76	**1.53**	1.03
10%	4.30	3.13	3.35	2.47	3.49	2.42	2.43	1.82	1.58	1.03
5%	4.53	3.38	3.07	2.42	3.54	2.50	2.36	1.77	1.67	1.07

Table 2.6: Results for truncated correlation: the error in classification as a function of the percentage of wavelet coefficients kept when calculating the correlation. The best result for each catalogue is shown in bold.

between two spectra in the template set. Since the pre-classified datasets I have are so small (with the exception of the Bailer-Jones catalogue) my method of testing the MDM's is to take one spectrum out and treat it as the unknown, using all the other spectra as template spectra. In a sense this is cheating, as the results obtained will be better than if the data was split into disjoint training and testing sets. Because of this, the results in this section should not be compared with results obtained using the correct training/testing procedure.

Table 2.6 shows the variation in classification error with the percentage of wavelet coefficients kept. There are several points that come from these results:

- There is significant variation in the results between catalogues. This is due to important differences such as the sampling resolution — the GS catalogue classifications have the lowest accuracy and the catalogue has the coarsest sampling at 20 /pix; the initial classification of the sources — in the SC catalogue, 22 out of 72 sources have a classification that covers more than one spectral subtype (*e.g.* o7b0v, g9k0v); coverage of the spectral types — obviously not having a template available for each spectral type will make the classification accuracy worse. Since each time one spectrum is taken out as the test case, this problem effects all spectral subtypes where there is only one representative spectrum in the catalogue (see Figure 2.7).

- The Bailer-Jones catalogue gives by far the best results, the most significant factors in this probably being the coverage and the quality of the classifications.

		GS		SC		JHC		PI		BJ	
		σ_{rms}	ϵ	σ_{rms}	ϵ	σ_{rms}	ϵ	σ_{rms}	ϵ	σ_{rms}	ϵ
–	100%	3.79	2.78	3.07	2.39	3.47	2.53	2.29	1.78	1.56	1.05
Var	50%	3.96	2.84	3.07	2.39	3.51	2.56	**2.25**	1.65	**1.52**	1.02
Var	10%	4.05	2.93	**3.07**	2.36	3.32	2.43	2.30	1.78	1.60	1.03
Var	5%	4.46	3.22	3.09	2.39	**3.29**	2.47	2.72	1.88	1.66	1.07
Ent	50%	3.64	2.69	3.10	2.45	3.74	2.76	2.41	1.80	1.54	1.05
Ent	10%	**3.64**	2.84	3.89	2.95	3.58	2.62	2.42	1.87	1.65	1.08
Ent	5%	3.95	2.88	4.07	2.93	3.68	2.60	2.60	1.89	1.77	1.17

Table 2.7: Results for weighted correlation: the error in classification as a function of the percentage of wavelet coefficients kept when calculating the correlation.

- Decreasing the number of wavelet coefficients kept when making the classification does not significantly reduce the accuracy of the classifications. This demonstrates that wavelet analysis is useful as a data compression and information extraction technique.

As an improvement to basic truncation and correlation, I tried to select the wavelet coefficients which carried the most information. One way of measuring the information is to calculate the variance of each pixel, over the set of templates $t_1 \ldots t_n$

$$\mathrm{Var}(t_1 \ldots t_n) = \frac{1}{n-1} \sum_{j=1}^{n} (t_j - t)^2 \,. \tag{2.25}$$

Another is to use the entropy of each pixel, i, calculated over the set of templates $t_1 \ldots t_n$

$$S_i = -\sum_{j=1}^{n} \alpha_{ij}^2 \log \alpha_{ij}^2 \tag{2.26}$$

where

$$\alpha_{ij} = \frac{w_{ij}}{\sqrt{\sum_j w_{ij}^2}} \tag{2.27}$$

and w_{ij} is the value of the wavelet coefficient at pixel i, in template j. The pixels with the highest variance or entropy are kept and used to do the correlation as before. Results from these methods are shown in Table 2.7. Using the coefficients with the highest variance allows a factor of 10 data compression without any significant change in the classification accuracy.

The best result for each catalogue in this section are all equal or better than the best result for each catalogue using straight correlation.

It is interesting to see whether the wavelets with the greatest variance across the training set correspond to features that we would expect to be useful in classifying spectra. Figure 2.11 shows a segment of a spectrum from the Bailer-Jones catalogue. Underneath it are plotted the variance values for wavelet coefficients at various resolution levels, where the variance is calculated across the set of wavelet-transformed Bailer-Jones spectra. The variance is higher in regions with strong spectral lines — each of the four main spectral lines marked can be clearly identified at one of the resolution levels — showing that the wavelets do pick out important features.

2.6.3 Criterion evaluation + correlation

As discussed in Section 2.3.1, criterion evaluation is the approach taken by human classifiers and hence was the method used in the first automatic classification systems. Since an automatic approach should be adaptable and fast, it is preferable to avoid calculating any specific properties of the spectra such as line widths or line ratios. However, I did test a slightly more general variation on the approach — using a filter to select the sections of the spectrum known to have important features. Since the intensity of the major lines used to classify spectra varies greatly across the range of spectral types, it seems that they will provide good discrimination between types.

The method is straightforward. Each continuum subtracted spectrum is multiplied by a weighting vector, consisting of 1's around the important features and 0's everywhere else. Then the spectrum is wavelet transformed and cross-correlated with the template spectra as described earlier. To make the weighting vectors I used various combinations of the lines of H, HeI, HeII, OI, OII, CaI, CaII, FeI, FeII and FeIII. I obtained the best accuracy (σ_{rms} = 2.28) using a combination of H, CaII, OI and FeII lines. This is not as good as selecting the wavelet coefficients on the basis of those with the greatest variance, highlighting one of the problems with this method – the difficulty of selecting the 'best' features for use in classification.

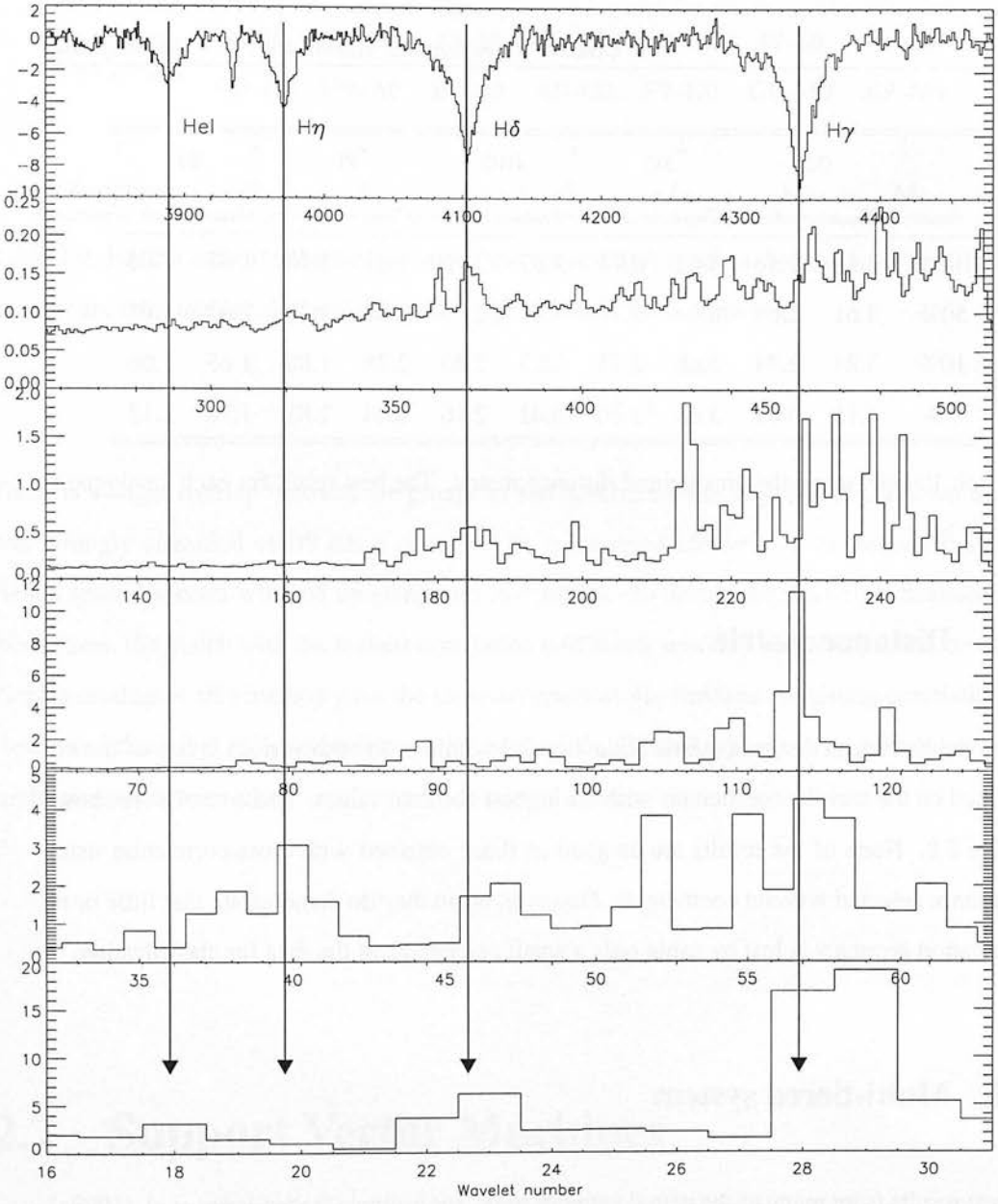

Figure 2.11: The variance of the wavelet coefficients across the set of Bailer-Jones spectra. The top panel shows a section of spectrum ($\lambda = 3801 - 4480$) with four spectral lines labelled. The second panel shows variance values for wavelet coefficients at the highest resolution level. The variance is quite low as this level mainly picks out noise in the spectra. The following panels show the variance for the coefficients at increasingly coarse resolution levels.

	GS		SC		JHC		PI		BJ	
	σ_{rms}	ϵ	σ_{rms}	ϵ	σ_{rms}	ϵ	σ_{rms}	ϵ	σ_{rms}	ϵ
100%	**3.56**	2.56	3.62	2.73	3.57	2.56	2.31	1.78	1.62	1.06
50%	3.61	2.64	3.63	2.77	3.51	2.50	**2.31**	1.78	**1.62**	1.05
10%	3.84	2.74	**3.60**	2.75	3.52	2.40	2.38	1.80	1.65	1.06
5%	4.15	3.01	3.68	2.80	**3.41**	2.36	2.38	1.81	1.76	1.13

Table 2.8: Results using the unweighted distance metric. The best result for each catalogue is shown in bold.

2.6.4 Distance metric

I tested the Euclidean distance metric (Equation 2.3 with $\alpha = 1$) with various levels of truncation based on the wavelet coefficients with the highest absolute values. These results are shown in Table 2.8. None of the results are as good as those obtained with cross-correlation using the variance selected wavelet coefficients. However, again they do demonstrate that little or no classification accuracy is lost by using only a small percentage of the data for classification.

2.6.5 Multi-tiered system

The best results from many of the neural network trials, for example Bailer-Jones et al. (1998a), are obtained by first classifying the spectra into general spectral type (O–M) and then classifying each class separately to obtain the spectral subtype. This has the advantage that the important information is reassessed, leading to a better classification. For example, a particular region of the spectrum may be useful for distinguishing between A and B stars, but not useful for distinguishing between A1 and A2 stars. To try and incorporate this into the basic methods, I developed a two-tier system which works as follows. The spectra are truncated based on the wavelet coefficients with the highest variance over the complete set of templates and then classified. Based on these initial classifications, the spectra are split into 7 groups, one for each spectral type, as shown in Table 2.9. Then the variance is calculated across each of these groups separately and each spectrum is reclassified using only the spectra in its group.

Test spectra	00–10 O0–B0	09–20 O9–A0	19–30 B9–F0	29–40 A9–G0	39–50 F9–K0	49–60 G9–M0	59–69 K9–M9
↓	↓	↓	↓	↓	↓	↓	↓
Templates	O	B	A	F	G	K	M

Table 2.9: For the second classification stage, test spectra with types in the ranges shown in the top row are correlated with templates of the type shown in the bottom row.

There is a slight overlap between the groups of test spectra so that, say, an A1 spectrum that was wrongly classified as B9 has a chance to be reclassified correctly in the second round. Hence several spectra will end up going into two groups. To decide the final classification in these cases, the match with the highest correlation coefficient was chosen. When tested on the Pickles catalogue, this method gave the same accuracy as the variance weighting correlation. However, I think that with a template set that covered the spectral type space more evenly, this could give superior results.

2.7 Support Vector Machines

The use of Support Vector Machines (SVM) have been proposed and used for astronomical applications in several conference papers (Goderya and McGuire, 2000; Humphreys et al., 2001; Wozniak et al., 2001) but other than this have not yet been used in astronomy. However, SVMs are known to outperform ANNs on many standard machine learning tasks. In this section I will briefly outline the theory behind SVMs and explain why they have the potential to improve on the methods more commonly used in astronomy, such as neural networks and decision trees. Then I will show the results of my application of SVMs to stellar spectral classification.

2.7.1 Theory

The basis of SVMs (and also ANNs) is the linear learning machine. As discussed earlier, in supervised learning the machine is given a training set which have already been classified by experts. The training set consists of the data (input) and the pre-assigned classifications (output). The learning process consists of finding a *target function* that maps the input data to the resulting output. For input $\mathbf{x} \in X$ where X is the set of possible input vectors, the linear learning machine has the form

$$f(\mathbf{x}) = \mathbf{w} \cdot \mathbf{x} + b \tag{2.28}$$

where $\mathbf{w}$ is the *weight vector* for the linear combination and b is the *bias* ($-b$ is often called the *threshold* in neural networks). $f(\mathbf{x})$ defines a hyperplane that divides the input space into two halves. Hence, the linear learning machine assigns inputs to the positive or negative class according to the sign of $f(\mathbf{x})$.

The *margin* of an example $(\mathbf{x}_i, y_i)$ where y_i is the correct classification, measures the distance from the hyperplane defined by $(\mathbf{w}, b)$ and is given by

$$M_i = y_i(\mathbf{w} \cdot \mathbf{x}_i + b) \, . \tag{2.29}$$

If $M_i > 0$ then the hyperplane correctly classifies example $(\mathbf{x}_i, y_i)$. The *geometric margin* is defined in a similar way with the normalised hyperplane $(\frac{1}{\|\mathbf{w}\|}\mathbf{w}, \frac{1}{\|\mathbf{w}\|}b)$ and gives the Euclidean distance to the plane. The margin of a training set is the maximum geometric margin over all hyperplanes.

Frank Rosenblatt proposed the first iterative algorithm for setting the weights of a linear learning machine in 1956. This *perceptron* algorithm formed the basis of early neural networks and involved updating the weights vector and bias directly using misclassified training examples. The final weights vector is a linear combination of the training examples

$$\mathbf{w} = \sum_{i=1}^{m} \alpha_i y_i \mathbf{x}_i \, . \tag{2.30}$$

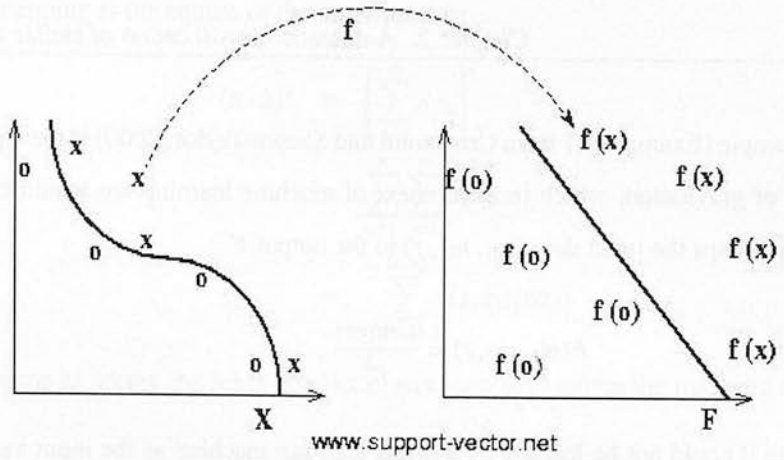

Figure 2.12: Attributes (**x** and **o**) that are not separable in linear space **X** are transformed (by a kernel **f**) into a space **F** in which they are separable. Image source: Cristianini and Shawe-Taylor (2000)

We can therefore rewrite the linear learning machine in *dual form*

$$f(\mathbf{x}) = \mathbf{w} \cdot \mathbf{x} + b \tag{2.31}$$

$$= \sum_{j=1}^{m} \alpha_j y_j \mathbf{x}_j \cdot \mathbf{x} + b \tag{2.32}$$

$$= \sum_{j=1}^{m} \alpha_j y_j \mathbf{x}_j \cdot \mathbf{x} + b \,. \tag{2.33}$$

Notice that $f(\mathbf{x})$ is now defined solely in terms of inner products of input examples. The dual perceptron algorithm only uses inner products of training examples. An advantage of the dual representation is that it is not dependent of the number of input parameters.

Since linear learning machines consider only functions that form linear combinations of the input variables they have limited computational power, because in many real world situations the object attributes can not be separated linearly. One approach to solving this problem was to have multiple layers of thresholded linear functions, which led to the development of neural networks. An alternative approach is to introduce *kernel representations* which project the data into a high dimensional space in which it is possible to separate the attributes linearly. This is demonstrated in Figure 2.12.

A concrete example (Example 3.1 from Cristianini and Shawe-Taylor, 2000) is the equation for Newton's law of gravitation, which in the context of machine learning we would call the target function, as it maps the input data (m_1, m_2, r) to the output F

$$F(m_1, m_2, r) = \frac{Cm_1m_2}{r^2} . \tag{2.34}$$

It its standard form it could not be learned by a linear learning machine as the input variables are related in a non-linear way. However, by transforming it into different coordinates

$$(m_1, m_2, r) \longmapsto (x, y, z) = (\ln m_1, \ln m_2, \ln r) \tag{2.35}$$

it is now in the form

$$\begin{aligned} g(x, y, z) &= \ln F(m_1, m_2, r) \\ &= \ln C + \ln m_1 + \ln m_2 - 2 \ln r \\ &= c + x + y - 2z \end{aligned}$$

which could be learned by a linear machine. This process can also be considered *feature selection* as a new set of quantities, features, are introduced to represent the original data. In this way, it is similar to transforming the data into its principal components before running a neural network. An advantage of SVMs is that they allow more generality in how you do the feature selection.

In the dual form the training examples never appear isolated, but always in the form of inner products between pairs of examples. By replacing this inner product by a kernel function, the mapping to higher dimensional feature space is done implicitly in the learning process without increasing the number of tunable parameters (weights). The definition of a kernel is a function K, such that for all $\mathbf{x}, \mathbf{z} \in X$

$$K(\mathbf{x}, \mathbf{z}) = \psi(\mathbf{x}) \cdot \psi(\mathbf{z}) \tag{2.36}$$

where $\psi(\mathbf{x})$ is a mapping from X to an inner product feature space F. Clearly the inner product is an example of a kernel by making the mapping $\psi(\mathbf{x})$ the identity function. An example of a

non linear mapping is the square of the inner product

$$(\mathbf{x} \cdot \mathbf{z})^2 = \left(\sum_{i=1}^{n} x_i z_i\right)^2 \tag{2.37}$$

$$= \sum_{i=1}^{n}\sum_{j=1}^{n} x_i x_j z_i z_j \tag{2.38}$$

$$= \sum_{(i,j)=(1,1)}^{(n,n)} (x_i x_j)(z_i z_j) \,. \tag{2.39}$$

This is the same as taking the inner product of $\psi(\mathbf{x})$ and $\psi(\mathbf{z})$ where the mapping function is

$$\psi(\mathbf{x}) = (x_i x_j)_{(i,j)=(1,1)}^{(n,n)} \,. \tag{2.40}$$

In this case the new features are all of the products of the existing features. We have implicitly increased the feature space with very little additional computation. In practice kernels are often defined directly and the feature space is implicitly defined. However, it is possible to explicitly define a feature space and take the inner product.

The problem of finding a separating hyperplane has non-unique solutions. Support vector classification aims to efficiently select a good separating hyperplane in high dimensional feature space. There are many alternative definitions of 'goodness'. The simplest example of an SVM algorithm is the Maximal Margin Classifier which aims to find the maximal marginal hyperplane. This reduces to a convex optimisation problem of minimising a quadratic function under linear inequality constraints.

Given a linearly separable training sample

$$S = ((\mathbf{x}_1, y_1), \ldots, (\mathbf{x}_m, y_m)) \tag{2.41}$$

find the hyperplane $(\mathbf{w}, b)$ that solves

$$\min_{(\mathbf{w},b)} \mathbf{w} \cdot \mathbf{w} \tag{2.42}$$

subject to

$$y_i(\mathbf{w} \cdot \mathbf{x}_i + b) \geq 1 \quad i = 1, \ldots, m \tag{2.43}$$

This optimisation problem is solved using Langrangian multipliers on the dual representation. In practice the maximal margin classifier is not used because the data is generally noisy and so not linearly separable without very powerful kernel functions which tend to lead to overfitting

of the data. However, they form the basis of many other SVM methods. For more details of how the algorithm works and a complete treatment of this field see Cristianini and Shawe-Taylor (2000).

2.7.2 Results

The particular SVM software that I have chosen to use is SVMTorch (Collobert and Bengio, 2001)[5] which I have used to do all my experiments. SVMTorch does multi-class classification and was chosen mainly because of ease of use. I used the Bailer-Jones catalogue for testing because, as discussed in Section 2.5, this is the only pre-classified catalogue currently available, with reasonable coverage of parameter space. There were a total of 5219 spectra which satisfied the quality flags that Bailer-Jones et al. (1998a) uses.

The most significant step in training the SVM is choosing the kernel to use. In an example like the one in Equation 2.34, there is a theoretical basis for choosing the transformation into a new space, since it obvious how the input quantities are related. However, for stellar classification there is no obvious theoretical reason for choosing a particular mapping, and so as with many machine learning problems it is necessary to experiment empirically to find a successful one. I ran initial experiments with three standard kernels: the polynomial kernel

$$K(x,z) = (sx \cdot z + r)^d \tag{2.44}$$

where s,r and d are constants, the Gaussian kernel

$$K(x,z) = e^{-\|x-z\|^2/2\sigma} \tag{2.45}$$

where σ is the standard deviation and the sigmoidal kernel

$$K(x,z) = \tanh(sx \cdot y + r) \tag{2.46}$$

where s and r are constants. I also experimented with a χ^2 kernel

$$K(x,z) = e^{-d(x,z)/\sigma^2} \tag{2.47}$$

[5]available from `http://www.torch.ch/`.

where $d(x, z) = \sum_{i=1}^{n} \frac{(x_i - z_i)^2}{x_i + z_i}$. I found that only the Gaussian kernel was successful for this task, and so I will use that throughout rest of this chapter.

For the initial testing I split the catalogue into a training set of 4696 spectra and a testing set of 523 spectra. Because the SVM uses the kernel representation, I hypothesised that doing dimensionality reduction using wavelets or PCA would make very little, if any difference to the results. However, I decided to test them anyway, and hence had 3 different forms for the input data:

Raw data Line only and line+continuum spectra, each with 820 pixels.

Principal components I used various numbers of project coefficients from the line only spectra [5, 10, 15, 25, 40, 50, 75, 100] as the input vectors.

Wavelet coefficients I used various numbers of wavelet coefficients [25, 50] as input vectors, selected in terms of greatest variance across the training set.

For the Gaussian kernel the free parameter is the standard deviation, σ. The results for different values for σ for the Gaussian kernel, using various numbers of principal components as inputs are shown in Figure 2.13. The most successful result was RMS = 1.83, for $\sigma = 2300$ and $n_{pc} = 100$, as shown in the right hand panel of the figure. Similar plots in Figure 2.14 show the results using wavelet coefficients as inputs. The best result was RMS = 2.14 for $n_{wvt} = 50$ and $\sigma = 15$ as shown in the right hand panel of the figure. Figure 2.15 show the results using the raw 820 pixel spectra directly as inputs to the SVM. I experimented with both the line-only and line+continuum data, with the best result being RMS = 1.729 for $\sigma = 40$ and using the line-only data. Pre-processing the data using principal components or wavelets did not improve the results, and in fact made them slightly worse than simply using the raw data.

To accurately compare two machine learning systems it is necessary to carry out some form of cross-validation, as described by Mitchell (1997). In this, the data is partitioned into k subsets, of equal size, where the size of each is at least 30. Then each learning system is trained and tested k times, each time using one of the subsets as the test set and the rest as the training data. This allows an accurate estimate of the systems performance to be determined. Although

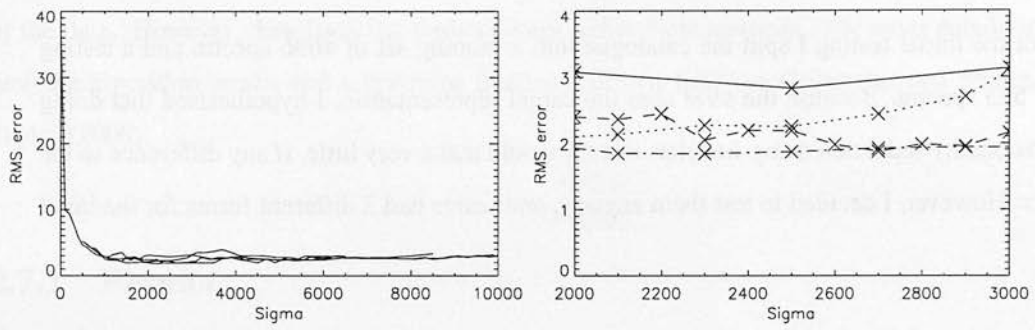

Figure 2.13: Left: Results for the Gaussian kernel shown across the entire range of σ values that I experimented with. Right: A zoomed in portion of the plot in the region that the best results were obtained, with various values of σ for inputs of: 10 principal components (solid line), 25 principal components (dotted line), 50 principal components (dashed line) and 100 principal components (dot-dash line).

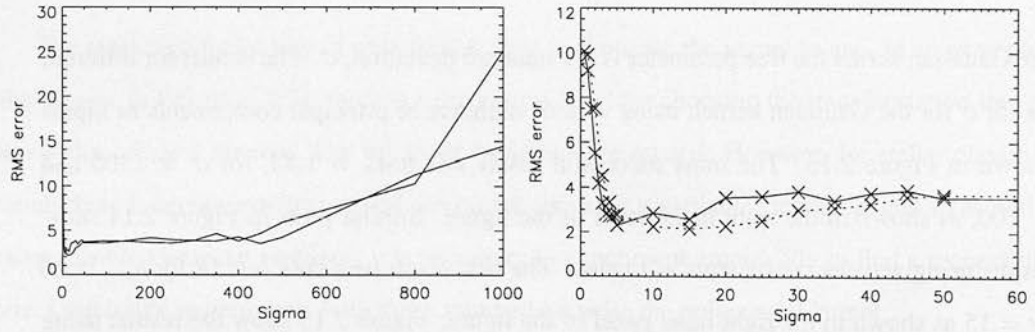

Figure 2.14: Results for the Gaussian kernel with various values of σ for inputs of: 25 wavelet components (solid line) and 50 wavelet components (dotted line). As in the previous plot, the left and right hand plots show the entire range of σ values and a zoomed in portion respectively.

none of the results above were as good as the `statnet` results I have done cross-validation on both `statnet` and SVMTorch to quantify how different the systems are. I divided the catalogue 5219 spectra into 20 different training and testing sets. Each training set consisted of 4959 spectra and each testing set had 260 spectra. I then ran the neural network (with settings as close to those used by Bailer-Jones as possible) and the SVM (with a Gaussian kernel) on each training/test set pair. I used several different values of the σ for the Gaussian, based on which ones performed best in the initial experiments done above. The results are shown in

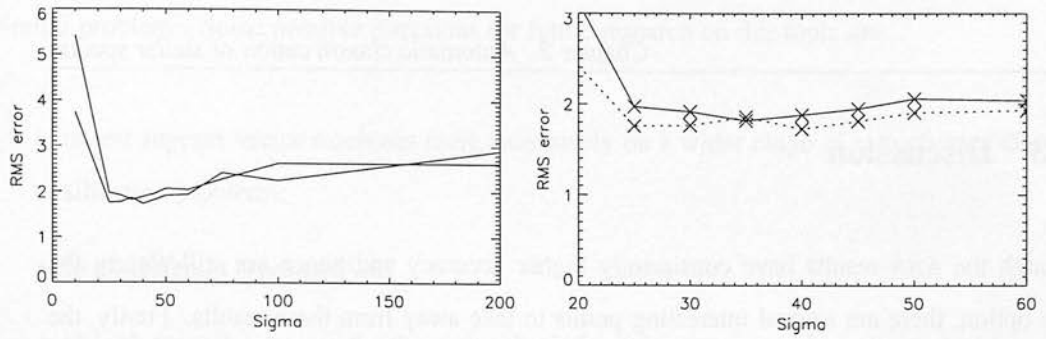

Figure 2.15: Results for the Gaussian kernel with various values of σ and using the raw spectra directly as inputs. The results for the normal spectra are shown with the solid line and the line-only spectra with the dotted line. As in the previous plot, the left and right hand plots show the entire range of σ values and a zoomed in portion respectively.

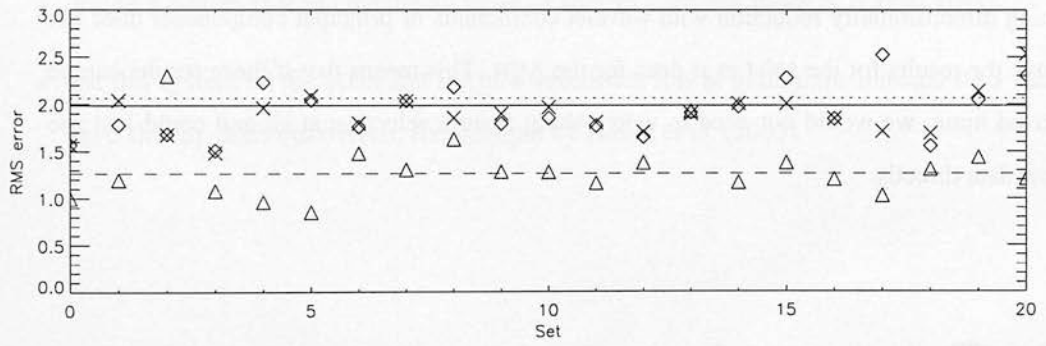

Figure 2.16: Cross-validation results for SVMTorch and `statnet`. The results for each set are denoted by points and the average for each method by a line as follows: SVM, Gaussian with $\sigma = 40$ (diamonds and solid line); SVM, Gaussian with $\sigma = 50$ (crosses and dotted line); committee of 10 ANN (triangles and dashed line).

Figure 2.16. The average RMS over all the sets is RMS = 1.98 for the SVM with $\sigma = 40$ and RMS = 1.21 for the neural network.

2.7.3 Discussion

Although the ANN results have consistently higher accuracy and hence are still clearly the better option, there are several interesting points to take away from these results. Firstly, the variation in the accuracy between each run shows the importance of proper comparisons on a range of test and training sets when testing any machine learning method. For example, the best result from the 20 trials of the ANN was RMS = 0.85 but the average over all the trials for the ANN was RMS = 1.21. In each case, only 260 spectra have been removed and yet the classification accuracy varies from between 0.85 and 1.79 for the neural network and between 1.51 and 2.30 for the SVM. This demonstrates the sensitivity of the systems to the exact nature of the training and testing data. Unless machine learning methods have been tested in this way, the quoted accuracy achieved is not necessarily reliable. Secondly, pre-processing the data by doing dimensionality reduction with wavelet coefficients or principal components does not improve the results for the SVM as it does for the ANN. This means that if these results can be improved upon, we would not need to worry about feature selection at all and could just use the raw data directly.

2.8 Future work

In this chapter I have shown that the traditional ways of classifying stellar spectra would not be practical for current and future datasets in which there may be millions of spectra. Old techniques such as minimum distance methods are not successful enough compared with machine learning techniques such as neural networks. Neural networks have massively increased the classification accuracy achievable in stellar spectra classification, as well as many other areas of astronomy. However, even neural networks have their limitations — one being their sensitivity to small changes in the training data or network parameters.

There are many other machine learning techniques, which have been underused in astronomy. I have demonstrated the use of one of these techniques, support vector machines, which, with further experimentation I believe will improve the results in stellar classification and other

similar problems. Some possible directions for future research on this topic are

- to test support vector machines more extensively on a wider range of astrophysics classification problems;
- to try different types of SVM;
- to look more deeply into the theoretical basis for selecting a good kernel;

Another problem that exists in stellar classification is the difficulty with developing a robust classification system. Most classification systems focus solely on main sequence stars, not including the more unusual stars such as Carbon stars and White Dwarfs. Any truly automatic system will have to work across a range of spectral types. Hence I think another direction for this research would be to

- design a system that can handle all types of spectra - not just those of normal stars;
- test this system on the SDSS and see how successful it is at finding the unusual stars that have already been discovered, for example by Harris et al. (2003).

CHAPTER 3

A library of high resolution Kurucz spectra

3.1 Introduction

Progress in population synthesis and automatic classification of stellar spectra has been limited by the spectral resolution of the available synthetic stellar spectra. The existing synthetic libraries are not at high enough resolution to be useful for classifying stars from recent surveys such as the SDSS (Stoughton et al., 2002) ($\lambda/\Delta\lambda \sim 1800$), or future surveys such as RAVE (Steinmetz, 2002) and GAIA (Lindegren and Perryman, 1996). Most classification techniques smooth the observed spectra to the resolution of the synthetic spectra. This means much of the detailed information in the observed spectra is lost, which may reduce the quality of the classifications. Population synthesis packages such as PEGASE (Fioc and Rocca-Volmerange, 1997) or GISSEL (Bruzual and Charlot, 1993) use a grid of stellar spectra to generate galaxy spectra. The resulting galaxy spectra are limited by the resolution of the input stellar spectra. To study the high resolution features, it is necessary to have a grid of observed or synthetic

stellar spectra which match the resolution of the observed galaxy spectra. For example, galaxy spectra synthesised from 20 spectra cannot be used to measure standard line indices like the Lick indices.

Perhaps the most widely used library of synthetic spectra are the flux distributions from the Kurucz ATLAS9 model atmospheres (Kurucz, 1993a). It is important to note that while these are usually referred to as spectra, they are flux distributions predicted directly from the model atmospheres, rather than spectra generated by a spectral synthesis program. This distinction will be made clearer in Section 3.2.4. The Kurucz atmospheres have several disadvantages which are discussed in various sources such as Kurucz (1992). However, one of their advantages is the wide range of parameter space that they cover, which is important for generating a grid of stellar spectra for population synthesis. The need for higher resolution spectra has been recognised for some time but, because of the immense computational expense involved, the synthesis of the spectra has been limited to partial wavelength ranges and specific regions of parameter space. Several groups have generated libraries of spectra from the Kurucz model atmospheres. For example, Chavez et al. (1997) provide a set of 711 Kurucz spectra at $\lambda/\Delta\lambda = 250\,000$ in the wavelength region $4850-5400$ and Castelli and Munari (2001) have generated a set of 698 Kurucz spectra at $\lambda/\Delta\lambda = 20\,000$, in the wavelength region $7650-8750$ for use with GAIA spectra. González Delgado and Leitherer (1999) have generated synthetic spectra in very small spectra regions necessary for a particular application. They created a grid of synthetic profiles of stellar H Balmer and HeI lines at $\Delta\lambda = 0.3$ for the purposes of evolutionary synthesis.

There are also several libraries of observed spectra now available at much higher resolution. For example, the ELODIE database (Prugniel and Soubiran, 2001), consists of 709 stars observed in the wavelength range $4100-6800$ with a resolution of $\lambda/\Delta\lambda \sim 42\,000$. STELIB (Le Borgne et al., 2003) provides spectra for 249 stars observed in the wavelength range $3200-9500$ with a resolution of $\lambda/\Delta\lambda \sim 2000$. These observed libraries are crucial for evaluating the accuracy of synthetic spectra and can also be used directly for population synthesis and classification. STELIB has been used by Kauffmann et al. (2003) with a new version of GISSEL, and ELODIE has been used to assign physical parameters to stars observed by the SDSS. However, a limitation of the observed spectral libraries is that they do not cover the full range in parameter space needed for galaxy population synthesis. Complete coverage of the

parameter space is even more important for stellar spectral classification. The most successful approaches to classification have used methods from machine learning (Bailer-Jones, 2001). As discussed in Chapter 2, in these methods, the distribution of spectra in the training set has a direct impact on the accuracy of the classification assigned to new spectra.

There are several efforts to generate higher resolution Kurucz spectra that are currently in progress. Bertone et al. (2002) have generated a grid of 832 spectra at $\lambda/\Delta\lambda = 500\,000$ over the wavelength range 3500 – 7000 . They intend to extend the wavelength range down to 850 at a resolution of $\lambda/\Delta\lambda = 50\,000$. Zwitter et al. (2002) are in the process of generating a grid of Kurucz spectra at $\lambda/\Delta\lambda = 20\,000$ over the wavelength range 2500 – 10 500 for use in radial velocity correction work.

I have generated a larger library of 6410 spectra from the Kurucz model atmospheres at a resolution of $\lambda/\Delta\lambda = 250\,000$. Previously these spectra were only available either at much lower resolution (20) or over small wavelength ranges. My spectra were generated from ATLAS9 model atmospheres, using John Lester's Unix version of the SYNTHE spectral synthesis package (Lester 2002, private communication). I have modified this package to improve the efficiency of the code, making it possible to generate the complete range of Kurucz spectra in a reasonable time.

In the next section I give some background to the theory of model stellar atmospheres and the atomic and molecular line data necessary for spectral synthesis. In Section 3.3 I describe the main characteristics of the new library of spectra. In Section 3.4 I compare the spectra with the 20 Kurucz spectra from Kurucz (1993a). Finally, in Section 3.5 I compare the spectra with observed spectra from the STELIB library. I will make this library of spectra available for general use on request.

3.2 Theory of stellar atmosphere modelling

3.2.1 Model atmospheres

Grids of model atmospheres have been around since the 1970's, starting with MARCS (Gustafsson et al., 1975) and ATLAS9 (Kurucz, 1979). These original grids were used in a range of applications for the next couple of decades. However, the limitations of these systems (mainly due to inadequate line lists) became more obvious as observational techniques improved. The next generation of model atmospheres came with the release of ATLAS9 (Kurucz, 1993a) (a subset of which were later improved by Castelli et al. (1997)) and NMARCS (Bessell et al., 1998). For a full derivation and analysis of the processes involve in modelling stellar atmospheres, the definitive reference is Milhalas (1978). Here I will give a greatly simplified summary, based partly on Ostlie and Carroll (1996) and Boehm-Vitense (1989), to cover the main points it is necessary to understand when using synthetic atmospheres and spectra. I then give some specific details of the Kurucz software packages, ATLAS9 and SYNTHE and the data they use.

The series of emission and absorption processes that result in photons travelling from the centre of a star out to the surface are collectively referred to as *radiative transfer*. The specific intensity, I_λ, is the amount of energy transported per unit of surface area, solid angle, wavelength and time

$$I_\lambda = E_\lambda d\omega^{-1} d\sigma^{-1} d\lambda^{-1} dt^{-1} \; . \tag{3.1}$$

For radiation travelling in a direction s, the change in specific intensity is the sum of the energy gains and losses along that path

$$dI_\lambda = -I_\lambda k_\lambda ds + S_\lambda k_\lambda ds \tag{3.2}$$

where S_λ is the source function

$$S_\lambda = \frac{e_\lambda}{k_\lambda} \tag{3.3}$$

which is the ratio of emission and absorption coefficients (e_λ and k_λ respectively). Equation 3.2 is the *radiative transfer equation* and solving it forms the backbone of all stellar atmosphere modelling. Usually it is not possible to solve the radiative transfer equation analytically and so the challenge of modelling stellar atmospheres is to solve it numerically, with the least number

of assumptions. The assumptions fall into three main categories: approximations of the thermodynamic state of the atmosphere, approximations of the opacity sources in the atmosphere and approximations of the geometry of the atmosphere.

The simplest model of a star is the case of gas confined within a box. The gas particles and blackbody radiation will come into equilibrium and hence the system has a single temperature. The system is in a *steady state* as there is no net flow of energy through the box, or between the matter and the radiation. Every process occurs as the same rate as its inverse process (*i.e.* photons are absorbed and emitted at the same rate). This system is said to be in *thermodynamic equilibrium*. Obviously this system is far too simple, as in a star there is a net flow of energy from the centre and the temperature changes with location. At any given position there is a mixture of gas particles that have travelled there from hotter and cooler regions. However, if the scale on which the temperature changes is much larger than the mean free path of the particles and photons, the approximation of *local thermal equilibrium* (LTE) can be used. This assumption makes the source function S_λ in the radiative transfer equation equal to the Planck function B_λ where

$$B_\lambda = \frac{2hc^2}{\lambda^5} \frac{1}{e^{hc/\lambda kT} - 1} \,. \tag{3.4}$$

In most cooler, main sequence stars model atmospheres which assume LTE are usually sufficient. However, for hot stars or those with very low density atmospheres (supergiants) this assumption breaks down, and non local thermal equilibrium (NLTE) models are required (*e.g.* the differences between LTE and NLTE are obvious for an O type star of $T_{\rm eff} \sim 35\,000$ K).

The absorption coefficient k_λ in Equation 3.2 is related to the *opacity* κ_λ by

$$\kappa_\lambda = k_\lambda / \rho \tag{3.5}$$

where ρ is the density. The opacity of a gas is a function of its composition, density and temperature. The slow variations in opacity with wavelength are what determines the shape of the continuum in a stellar spectrum. The small scale variations result in the absorption features in the spectrum. The four processes that contribute to the opacity are: bound-bound transitions, bound-free absorption, free-free absorption and electron scattering, with the total opacity being the sum of these

$$\kappa_\lambda = \kappa_{\lambda,bb} + \kappa_{\lambda,bf} + \kappa_{\lambda,ff} + \kappa_{\lambda,es} \,. \tag{3.6}$$

In most stellar atmospheres the photo-ionisation of H^- ions is the main source of continuum opacity. For hotter stars (spectral types B and A) the photo-ionisation of hydrogen atoms and free-free absorption are the main sources of continuum opacity. In extremely hot stars (spectral type O), electron scattering becomes more important, as well as the photo-ionisation of helium. In cooler stars molecules contribute to the bound-bound and bound-free opacities. An example of the effect of opacity can be seen in the Balmer jump at 3647 . To eject an electron from the $n = 2$ orbit of a hydrogen atom, a photon must have an energy of at least 3.40 eV which corresponds to a wavelength of $\lambda = 3647$. Hence at wavelengths $\lambda \leq 3467$ the opacity of the stellar atmosphere suddenly increases and the measured flux decreases, giving the observed jump in the continuum.

The optical depth, τ_λ, is effectively how far into the stellar atmosphere you could 'see', and is given by

$$d\tau_\lambda = -\kappa_\lambda \rho ds \; . \tag{3.7}$$

It varies with wavelength because the opacity κ_λ varies with wavelength. To simplify the system so that each atmospheric level has a single optical depth, a wavelength independent opacity is assumed — usually the Rosseland mean opacity which is the average opacity over all wavelengths. Models that use this assumption are referred to as *gray atmospheres* and are a good approximation for a majority of stars, in which photo-ionisation of H^- is the main source of opacity. However, this assumption is too limiting for more accurate modelling.

The main geometrical assumptions involve reducing the model atmosphere from a three-dimensional to a one or two-dimensional problem and using some kind of symmetry to further simplify the system. The most common assumption is of a *plane-parallel atmosphere* with horizontally homogeneous layers. The horizontality assumption is made on the basis that the atmospheres of main sequence stars are very thin compared with the size of the star. Hence the atmosphere's radius of curvature is much larger that its thickness and so it can be considered to be flat. The homogeneity assumption is made to simplify the system — it does not have an empirical or theoretical basis, and in fact observational evidence suggests that the assumption of homogeneous layers is not valid. A more complex, but still one-dimensional model is that of *spherical symmetry*. This is necessary for stars with extended atmospheres (giants, supergiants and hot stars) for which the atmospheric thickness is not negligibly thin compared with the

radius of the star. Current research focuses on modelling atmospheres in 2D or 3D, which is extremely computationally intensive.

3.2.2 Spectral lines

The shape of each spectral line is an indicator of the environment it formed in. At the central wavelength is the *core* of the spectral line and the sides, which curve up to the continuum, are its *wings*. The strength of the line is usually measured by its equivalent width

$$W = \int \frac{F_c - F_\lambda}{F_c} d\lambda \tag{3.8}$$

which is the width of a box, reaching the continuum, which has the same area as the line. Three main processes cause the broadening of spectral lines, each affecting the line shape in a different way. These are

Natural broadening which is a result of the uncertainty principle and gives rise to a Lorentzian line shape;

Doppler broadening which is due to the random motions of the atoms in the gas and results in a Gaussian line shape for a Maxwellian velocity distribution;

Pressure broadening which is due to collisions with neutral atoms or close encounters with the electric field of ions and results in an approximately Lorentzian line shape. The specific case of collisions with ions and electrons is called *Stark broadening*.

Generally the Doppler profile is dominant in the core of the absorption line and the Lorentzian is dominant in the wings. The total line profile is a convolution of a Gaussian and a Lorentzian and is called a *Voigt profile*.

3.2.3 Atomic and molecular data

The success of model stellar atmospheres depends heavily on atomic physics. To produce a synthetic spectrum it is necessary to have accurate values for energy levels, wavelengths, Gaunt

factors[1], damping constants, photo-ionisation cross-sections and collisional cross-sections for atomic and molecular lines. Kurucz has developed many of these resources, which are available in his line lists (see, for example Kurucz, 1995). Some of the data is empirical, however most of the lines are 'predicted' lines, obtained theoretically.

Kurucz provides a range of different files with line lists for different purposes. All the atomic line information is grouped together in LOWLINES. This massive line list is necessary to reproduce the total opacity in a spectrum, however for individual lines this is not necessarily the most accurate source of spectral line information. There are more up to date line lists available in separate files, however these do not have all the predicted lines and so do not reproduce the opacity accurately.

An alternative source is the Vienna Atomic Line Database (VALD) (Kupka et al., 2000), which is a compilation of atomic line information from a wide range of sources. It was developed to provide a highly accurate set of line data in a standard format. Another source of line data is the Opacity Project (Seaton, 1995), which is concerned with calculating atomic properties for the large number of lines required to model opacity. Lines from these sources can be used to update or supplement the Kurucz line lists.

3.2.4 ATLAS9 and SYNTHE

One of the main difficulties in calculating LTE model atmospheres is that the absorption and emission coefficients (j_ν and κ_ν) depend heavily on frequency. This means that atoms like iron, which have millions of spectral lines, require radiative transfer equation to be solved for a massive number of different frequencies. The opacity resulting from all the spectral lines changes the temperature gradient in the atmosphere, an effect known as *line blanketing*. There are three possible approaches to calculating the opacity. The first is to calculate all of the spectral lines directly, but this is too computationally expensive as for a typical spectrum it would involve millions of points (Kurucz, 1996). The second approach is to tabulate statistical distribution functions for the opacity, in terms of temperature and pressure. The opacity spectrum is then

[1]Gaunt factors (gf) are quantum mechanical corrections to the absorption coeffi cients.

divided into small wavelength intervals and a distribution function calculated for each interval. This method is referred to as the *opacity distribution function* (ODF) technique and is what is done in the ATLAS9 software. It is well suited to LTE models as all the opacity contributions from different sources can be combined. The standard grid of Kurucz model atmospheres have the opacity calculated in bins of 10 – 20 width. Hence the flux distributions produced directly from the atmosphere code are also at this resolution. The third method is to sample the spectrum at a small number of wavelength points and do a detailed calculation for these values. Then these are used to obtain the overall opacity distribution. This technique is called *opacity sampling* and is used by the new Kurucz model atmosphere software ATLAS12 (Kurucz, 1996).

Once the atmospheres have been calculated, high resolution spectra can be generated using the spectral synthesis package, SYNTHE (Kurucz, 1993c). In SYNTHE the spectral line profiles are calculated for each line (or wavelength region). Then the LTE opacity, NLTE opacity, continuum opacity are added together to compute the flux at each wavelength point and each line centre. Incorporating the line profiles and continuum information then results in the final synthesised spectrum. SYNTHE uses the same set of line lists as ATLAS9, but obviously in spectral synthesis it is more important that specific line data is accurate than when calculating opacities in the model atmosphere process. ATLAS12 will incorporate the model atmosphere and spectral synthesis procedures into one process.

3.3 Generating the Kurucz spectra

The library presented here has been created using the updated versions of the ATLAS9 model atmospheres from Kurucz (1993a). These are available from Kurucz's website [2] (labelled `.dat`). Kurucz advises that the Kurucz (1993a) models (labelled `.datCD`) should not be used as they have a discontinuity in the fluxes and colours as a function of $T_{\rm eff}$ and $\log(g)$ that was corrected for the revised version.

The models assume plane parallel homogeneous layers in steady state and local thermal

[2] `http://kurucz.harvard.edu`

Linelist	N_{lines} included
NLTELINES	12 283
LOWLINES	7 896 400
DIATOMICS	3 549 230
TIOLINES	31 473 051

Table 3.1: Number of lines included from each linelist for a spectrum covering the wavelength range 3000 – 10 000 . The TiO lines are from the Schwenke linelist on Kurucz (1999). Note that for the spectra I generated, the TiO lines were not actually included.

equilibrium. A microturbulence velocity of 2 kms^{-1} and a mixing-length value of $\ell/H_p = 1.25$ are used. Castelli et al. (1997) give a detailed discussion of whether the mixing length theory for convection is dealt with adequately in the standard Kurucz atmospheres. They have calculated an alternative set of atmospheres in which the Kurucz 'overshooting' approximation is not used (NOVER models). These models have been shown to predict more accurate observable properties (*e.g.* colours) for some atmospheres (Heiter et al., 2002; Smalley and Kupka, 1997; Smalley et al., 2002). However, since they are currently available only for some metallicity values (-2.5, -2.0, -1.5, -1.0, -0.5, 0.0, +0.5 dex) I decided not to use these atmospheres for population synthesis. I have generated a small subset of spectra from the NOVER models for comparison purposes.

The adopted atomic line lists for all my spectra are LOWLINES and NLTELINES from Kurucz (1994), and the adopted molecular line list is DIATOMIC from Kurucz (1993b). I have included both predicted and measured lines. The inclusion of the predicted lines is necessary to reproduce accurate flux distributions. However, it does mean that care should be taken when using the high resolution spectra, as the properties of individual lines may not be as accurate as if Kurucz's more up to date linelists (which do not include predicted lines) were used. The molecular lines have been included for spectra with $T_{\mathrm{eff}} \leq 7000$ K. To give some idea of the number of lines involved in generating a spectrum in the wavelength range 3000 – 10 000 , Table 3.1 gives the numbers for each of the linelists used.

The original programs making up the Kurucz package were written in FORTRAN77 for

the VAX. John Lester has written a Unix version based on the original Kurucz code, in FORTRAN77 and a more recent Unix version in Fortran90 (Lester 2002, private communication). However, this code could only be used to generate small sections of a spectrum at a time because it required massive quantities of disk space. The complexities in generating spectra with SYNTHE has restricted researchers to creating either a small number of spectra, or a large number over a very small wavelength range. I have modified the Lester code to dramatically reduce the disk usage of SYNTHE which makes it feasible to generate large spectral ranges on standard hardware in a relatively short period of time. I have not yet generated spectra for values of $T_{\rm eff} \leq 5000$ K. These spectra require TiO lines to be included which makes the program significantly slower (Table 3.1 shows that the number of TiO lines required in this wavelength range is an order of magnitude larger than the number of other molecular lines) and requires more disk space. I am investigating whether further optimisations may be made.

Of the 7216 model atmospheres available in Kurucz's standard distribution, I have generated a grid of 6410 spectra, which excludes the lowest temperature spectra (Figure 3.1). The spectra cover the wavelength range 3000 – 10 000 which was chosen to be useful for comparisons with SDSS spectra. The spectra were generated at a resolution of $\lambda/\Delta\lambda = 250\,000$, using the updated versions of the ATLAS9 model atmospheres from Kurucz (1993a). It is important to note these are not the same set of atmospheres as the ones from which the widely used 20 Kurucz flux distributions were generated from.

3.4 Comparisons with the 20 Kurucz spectra

In this section I compare my library of spectra with the revised version of the 20 Kurucz flux distributions. There have been several changes to the software and data between the original release of the 20 Kurucz flux distributions, and the present. Also, the flux distributions are predicted directly from the model atmosphere code, so it is not possible to compare them directly with the spectra generated by spectral synthesis. Because of this, I did not expect the spectra I have generated to match the flux distributions exactly, but it is an important check to make sure there was broad agreement between the spectra.

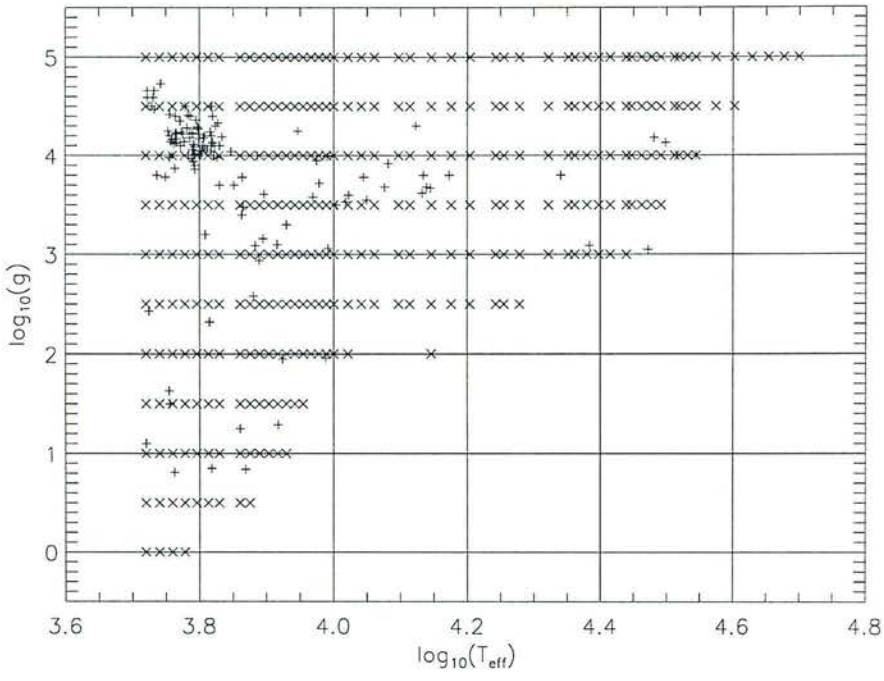

Figure 3.1: The distribution of my Kurucz spectra in $\log(T_{\rm eff}) - \log(g)$ space (×). Also plotted is the distribution of the STELIB spectra with $T_{\rm eff} > 5000$ K (+). The Kurucz spectra cover 19 metallicities in the range -0.5 to 1.0. The STELIB spectra have metallicities ranging from -2.24 to 2.07.

3.4.1 Direct comparisons

Firstly I compared the higher resolution Kurucz spectra with the 20 flux distributions. Figure 3.2 shows several examples of these comparisons. For the purposes of this comparison, I re-binned the new spectra to 20 using a simple top-hat function. There are several differences between the two sets of spectra:

1. There is an extra dip in the new spectra at around 3700 . This is due to inadequate treatment of the Balmer jump. In the model atmosphere code, the way the Balmer jump is dealt with has been modified in order to remove the dip (Kurucz, private communication).

2. In some of the lower temperature spectra, the shape of the Ca H/K doublet is not identical. This is largely due to the fact that for the model atmospheres, the Stark broadening

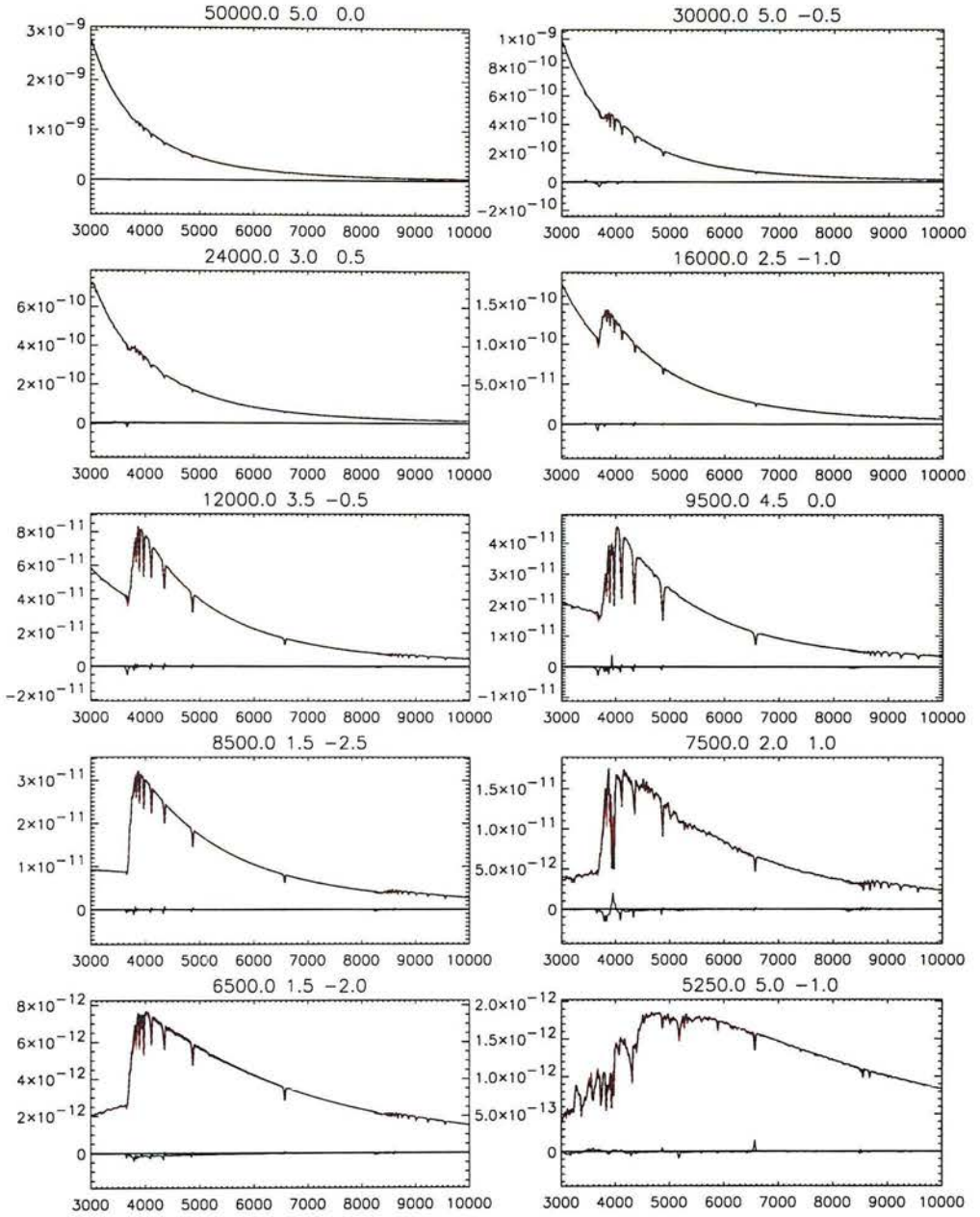

Figure 3.2: Comparison between a sample of the 20 Kurucz flux distributions (black) and the newly generated Kurucz spectra (red) top-hat smoothed to $\Delta\lambda = 20$. These spectra cover a range of physical parameters: the title of each plot gives the values for $T_{\rm eff}$, log(g) and [M/H]. The x-axis is the wavelength in and the y-axis is flux, $F(\lambda)$, in arbitrary units. Underneath each pair of spectra is $\Delta F = F(\lambda)_{\rm new} - F(\lambda)_{\rm old}$.

was artificially increased to make up for missing lines in computing the distribution function (Kurucz, private communication). This was changed back to generate the synthetic spectra, and also for the flux distributions generated from atmospheres more recent than the ones I used to generate my spectra.

3. In lower temperature spectra ($T_{\rm eff} \leq 7000$ K) there is a systematic difference in flux in the G-band. This is likely to be due to changes in the molecular line lists since the flux distributions were produced.

4. Most of the strong lines have slightly different depths. These small peaks are likely to be unresolved line cores, caused by the fact that the 20 flux distributions are undersampled, whereas my new synthetic spectra are generated at high resolution.

Probably the most significant of these points for my applications is the difference in the G-band flux.[3] This affects individual lines, and the U band magnitude of the spectra. In the following sections I will quantify this.

3.4.2 Colours

Comparing the $UBVRI$ magnitudes is important for checking that the broadband properties of the spectra are reproduced. I have used the Johnson-Cousins bandpasses, as defined by Bessell (1990) and shown in Figure 3.3. Figure 3.4 shows the offset in magnitudes calculated for the new spectra and the 20 flux distributions. The RMS errors for the magnitudes for the two sets of spectra are: $\Delta U = 0.05$ mag, $\Delta B = 0.01$ mag, $\Delta V = 0.01$ mag, $\Delta R = 0.01$ mag and $\Delta I = 0.01$ mag. The B, V, R and I magnitudes are in good agreement. However, the differences are greater for the U magnitudes at lower temperatures ($T_{\rm eff} \leq 7000$ K). For higher temperature spectra the U magnitudes are also in good agreement. The U band discrepancy is a consequence of the differences in the spectra noted in Section 3.4.1.

The question is how important these magnitude offsets are for the applications I am interested in. A difference in measured colour is largely degenerate with a difference in $T_{\rm eff}$.

[3]Note that in recent literature, the term G-band has been reserved for the feature around 4300, which does not really stand out in Figure 3.2.

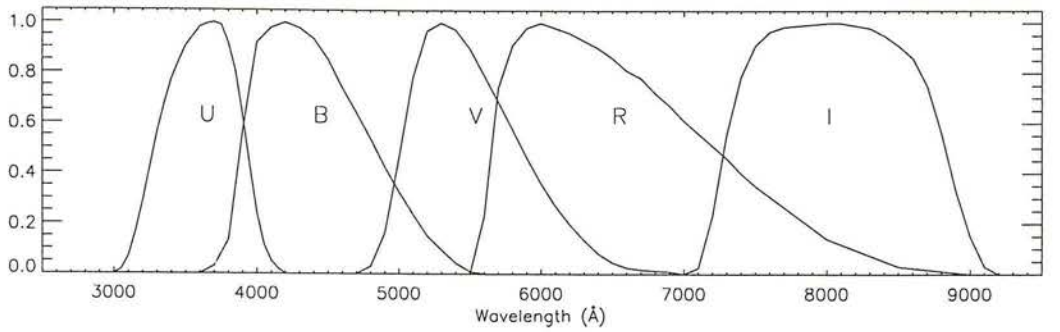

Figure 3.3: The *UVBRI* Johnson-Cousins bandpasses, as defined by Bessell (1990).

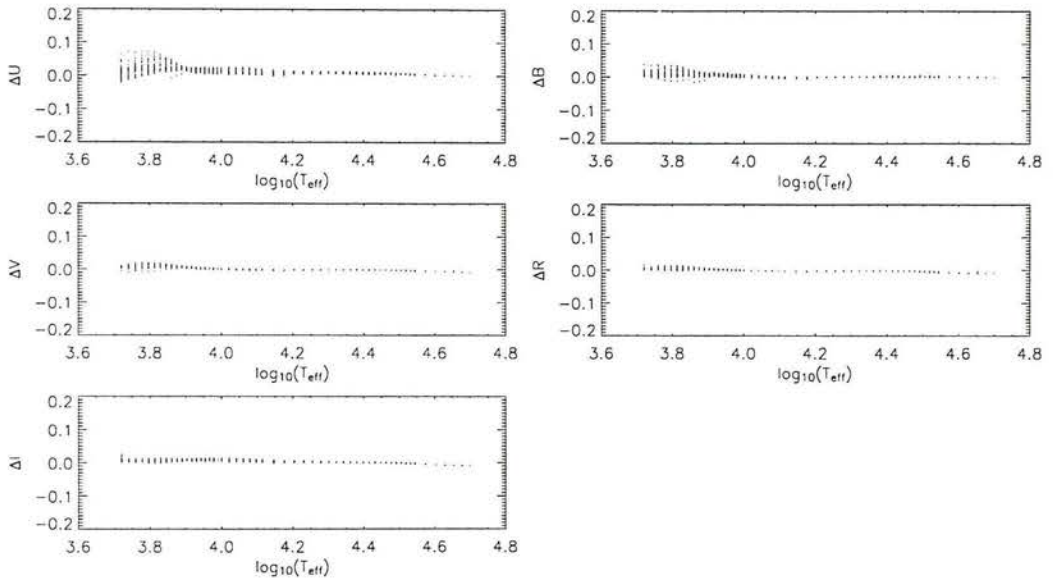

Figure 3.4: Magnitude offsets between my Kurucz spectra and the 20 flux distributions. The x-axis is $\log_{10}(T_{\rm eff})$ and the y-axis shows the difference (in magnitudes) between the Kurucz spectra I have generated and the 20 flux distributions.

For example, Lejeune et al. (1997) find that the colour versus temperature relations for Kurucz spectra do not match those derived empirically. To fix the problem, they developed a method for adjusting the shape of the continuum (in other words change the magnitudes) for spectra of a certain $T_{\rm eff}$ (this will be discussed further in Section 4.2.2). However, an alternative approach is to leave the shape of the spectrum unchanged and reassign a $T_{\rm eff}$ to the spectrum. For example, a solar metallicity spectrum with $T_{\rm eff}$ = 7500 and $\log(g)$ = 1.0 has a U magnitude offset of 0.05. This difference in colour between my new spectrum and the Kurucz flux distribution

corresponds to a change of $T_{\rm eff}$ by less than 30 K. Since quoted errors for temperatures on observed spectra are typically around 40 – 100 K (see, for example Katz et al., 1998; Alonso et al., 1999), the spectra agree to within usual measurement errors. However, this approach may not be as successful when dealing with near-IR colours.

3.5 Comparisons with observed spectra

Having shown that the new spectra agree reasonably well with the 20 flux distributions, the next step is to evaluate them against observed spectra. This serves two purposes. Firstly, there are some differences between the two sets of Kurucz spectra, especially in the blue. However, if these differences are smaller than the differences between the Kurucz spectra and an observed spectrum with the same physical parameters, then they may be neglected. Secondly, I want to evaluate what kind of applications the synthetic spectra can be used for. The aim is to demonstrate that my new Kurucz spectra are as suitable for use in population synthesis as the commonly used 20 Kurucz flux distributions, but with the advantage of higher resolution. There are already various comparisons of Kurucz spectra with observed spectra in the literature. For example, the colour–$T_{\rm eff}$ correlation for the spectra has been analysed by Lejeune et al. (1997) and the 20 spectra have been compared with observed spectra by Straižys et al. (1997) and Straižys et al. (2002). Here I make my own comparisons to focus on properties such as the Lick indices which are relevant to the specific applications I am interested in.

3.5.1 Direct comparisons

I have compared the spectra to those in the STELIB library (Le Borgne et al., 2003), which consists of 250 spectra in the visible range (3200 – 9500) with a spectral resolution of $\Delta\lambda \lesssim 3$ and covering a wide range in parameter space. As well as a direct comparison of the SEDs, I compare the measured colours and Lick indices to confirm that the spectra meet my requirements. Many of the STELIB stars do not have values for all three physical parameters ($T_{\rm eff}$, log(g) and [M/H]), have large sections of the spectrum missing, or do not lie close to a point on my grid of

spectra. Hence I have selected a subset of 125 of the spectra that have tabulated values for $T_{\rm eff}$, $\log(g)$ and [M/H] in Le Borgne et al. (2003), $T_{\rm eff} > 5000K$, and which have a good χ^2 match to the corresponding Kurucz spectrum. The values for most of the physical parameters were obtained from the Cayrel de Strobel et al. (1997) and Cayrel de Strobel et al. (2001) catalogues. However, some were obtained from the ELODIE database (Prugniel and Soubiran, 2001) and several were calculated using the TGMET method (Katz et al., 1998).

The STELIB spectra have not been corrected for interstellar reddening, which is the extinction due to the intervening matter in the Milky Way. The extinction A_X of an object in some waveband X is defined to be the difference between the observed magnitude $m(X)$ in that waveband and the magnitude $m_0(X)$ that would be observed in the absence of dust

$$A_X \equiv (m - m_0)_X \ . \tag{3.9}$$

The *reddening* or colour excess, $E(X-Y)$, in some colour $X-Y$, is defined as the difference between the observed colour $m(X) - m(Y)$ and the intrinsic colour $m_0(X) - m_0(Y)$

$$E(X-Y) \equiv [m(X) - m(Y)] - [m_0(X) - m_0(Y)] = A_X - A_Y \ . \tag{3.10}$$

The extinction is different along different lines of sight and at different frequencies. Empirically measured *extinction curves* give the relationship between the ratio A_λ/A_J (extinction at that wavelength over extinction in the Johnson J band) and wavelength for any given line of sight. The slope of the extinction curve near the V band is $A_V/(A_J R_V)$ where

$$R_V \equiv \frac{A_V}{A_B - A_V} = \frac{A_V}{E(B-V)} \ . \tag{3.11}$$

Empirical studies show that $R_V \approx 3.1$ for lines of sight that do not pass through dense clouds[4]. I corrected the spectra for interstellar reddening using the values of A_V from Le Borgne et al. (2003) and the reddening curve from Cardelli et al. (1989), as implemented in the IDL ASTROLIB routine CCM_UNRED.PRO.

A selection of the dereddened STELIB spectra are plotted against the closest matching Kurucz spectra (the Kurucz spectrum with the closest physical parameters) in Figure 3.5. When looking at these plots there are several points to note. Firstly, the parameters of the Kurucz

[4]The preceding discussion and equations are based on that in Binney and Merrifield (1998).

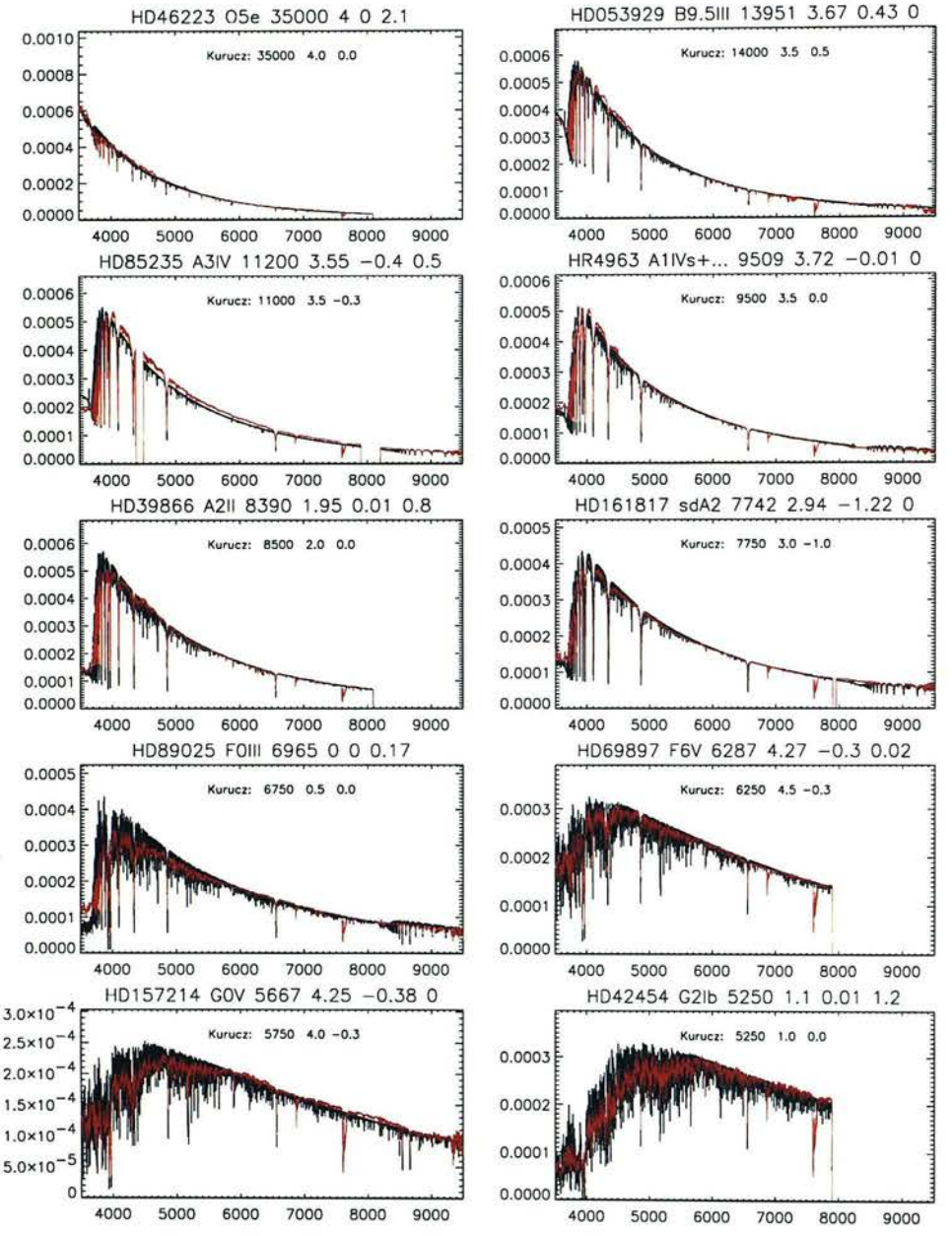

Figure 3.5: Comparison between a sample of the STELIB spectra (red) and the newly generated Kurucz spectra (black). These spectra cover a range of physical parameters: the title of each plot gives the values for $T_{\rm eff}$, $\log(g)$, [M/H] and $A_{\rm V}$ for the STELIB spectrum. The annotation gives the physical parameters for the Kurucz spectrum. The x-axis is the wavelength in angstroms and the y-axis is flux, $F(\lambda)$, in arbitrary units.

spectra do not match the STELIB parameters exactly (there is up to 100 K difference in temperature), they are just the closest match on the grid. Secondly, there are sections missing from some of the STELIB spectra, so I have not plotted these regions. Also, the STELIB spectra have not been corrected for atmospheric absorption, so they have strong absorption features (most noticeably in the Oxygen A-band around 7600) which are not present in the synthetic spectra.

3.5.2 Colours

I have calculated colours for all of the STELIB spectra and their closest Kurucz matches. Since the wavelength range of the STELIB spectra is 3200 – 9500 , I have calculated a modified U band magnitude (denoted U^*) which is truncated at 3200 for both the STELIB and Kurucz spectra. Figure 3.6 shows the magnitude offsets between the STELIB spectra and their Kurucz matches. The RMS error between the two sets of spectra are: $\Delta U^* = 0.14$ mag, $\Delta B = 0.05$ mag, $\Delta V = 0.02$ mag, $\Delta R = 0.03$ mag and $\Delta I = 0.04$ mag. For comparison, I also calculated the magnitude offsets for the STELIB spectra and their closest Kurucz matches, using the 20 flux distributions. The RMS error between these two sets of spectra are: $\Delta U^* = 0.11$ mag, $\Delta B = 0.05$ mag, $\Delta V = 0.02$ mag, $\Delta R = 0.03$ mag and $\Delta I = 0.04$ mag. This demonstrates that, with the exception of U^*, the scatter in the magnitudes is no worse for my new spectra than for the 20 spectra that are in standard use.

Some differences are expected due to the mismatch between the STELIB temperatures and those of the closest Kurucz match – many of the spectra have a difference in temperature of about 100 K, corresponding to a difference of a few hundredths in magnitude. However, the important point for this work is that my new spectra are as well matched to the observed spectra as the 20 spectra that are often used for population synthesis. Figure 3.7 shows various colour comparisons. There is some scatter in each of the plots and a slight systematic offset in $R - I$. Again however, this is no worse than when comparing the 20 spectra with the STELIB spectra.

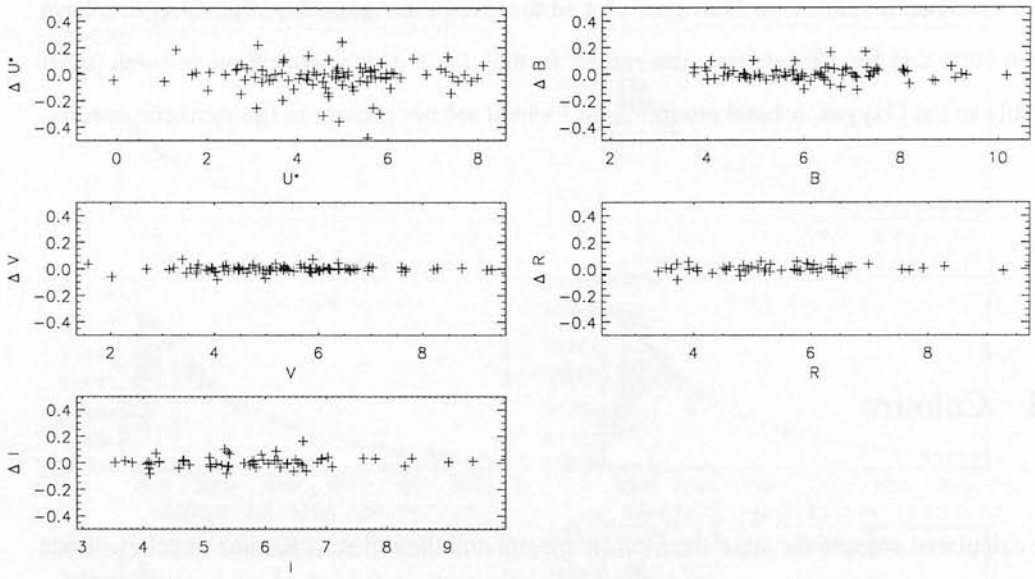

Figure 3.6: Magnitude offsets between the STELIB spectra and their closest matches from the Kurucz grid.

3.5.3 Line indices

I have calculated Lick indices for each of the 125 STELIB spectra in my sample, and for the matching Kurucz spectra. The process of calculating Lick indices will be discussed in detail in Section 4.5 so in this section I will just give the basic equations and bandpass definitions. There are two types of index, atomic (I_a) and molecular (I_m) which I have calculated from the standard formulae

$$I_a \equiv \int_{\lambda_{c1}}^{\lambda_{c2}} \left[1 - \frac{S(\lambda)}{C(\lambda)}\right] d\lambda \tag{3.12}$$

$$I_m \equiv -2.5 \log_{10} \frac{\int_{\lambda_{c1}}^{\lambda_{c2}} \frac{S(\lambda)}{C(\lambda)} d\lambda}{\lambda_{c2} - \lambda_{c1}} \tag{3.13}$$

where λ_{c1} and λ_{c2} are the limits of the central bandpass defining the index, $S(\lambda)$ is the object spectrum and $C(\lambda)$ is the linearly interpolated pseudo-continuum, defined by

$$C(\lambda) \equiv S_b \frac{\lambda_r - \lambda}{\lambda_r - \lambda_b} + S_r \frac{\lambda - \lambda_b}{\lambda_r - \lambda_b}. \tag{3.14}$$

Here,

$$S_b \equiv \frac{\int_{\lambda_{b1}}^{\lambda_{b2}} S(\lambda) d\lambda}{\lambda_{b2} - \lambda_{b1}}, \quad \lambda_b \equiv (\lambda_{b1} + \lambda_{b2})/2 \tag{3.15}$$

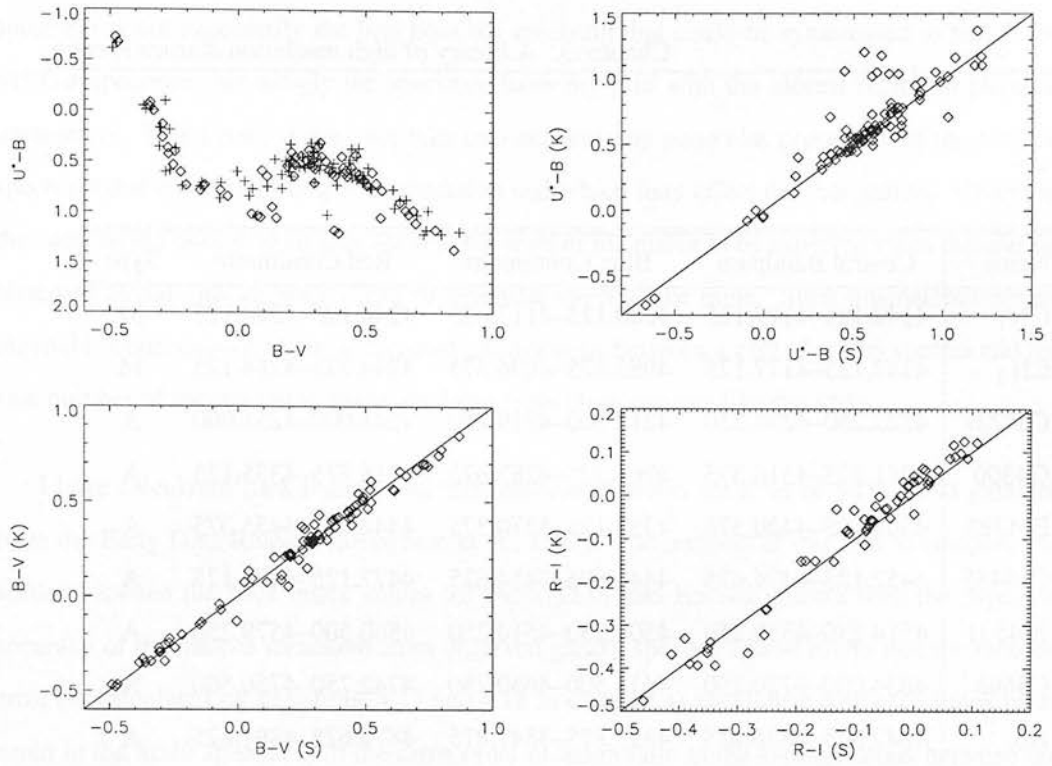

Figure 3.7: Top Left: $U^* - B$ vs. $B - V$ for STELIB spectra (+) and their Kurucz matches ($\diamond$). Top Right: $U^* - B$ colours for STELIB spectra (x-axis) and their Kurucz matches (y-axis). The solid line is the line '$x = y$' for comparison. Bottom Left: Comparison of $B - V$ colours. Bottom Right: Comparison of $R - I$ colours.

$$S_r \equiv \frac{\int_{\lambda_{r1}}^{\lambda_{r2}} S(\lambda) d\lambda}{\lambda_{r2} - \lambda_{r1}}, \quad \lambda_r \equiv (\lambda_{r1} + \lambda_{r2})/2 \tag{3.16}$$

and λ_{b1}, λ_{b2}, λ_{r1} and λ_{r2} are the limits of the blue and red continuum bands. The bandpass definitions for the Lick indices and the red and blue pseudo-continua are those defined in Trager (1997) and are given in Table 3.2. These bandpasses have been refined since Worthey et al. (1994), and are also available on Guy Worthey's website [5].

Figure 3.8 shows the correlation between the Lick indices calculated from the STELIB spectra and the Kurucz spectra. I have not calculated the two TiO indices since TiO lines are switched off in these spectra. The average absolute offsets $\left(\sum \frac{|I_k - I_s|}{n}\right)$ for the correlations are given in Table 3.3. It should be noted that the Kurucz spectrum paired with a given STELIB

[5] http://astro.wsu.edu/worthey/html/system.html

Name	Central Bandpass	Blue Continuum	Red Continuum	Type
CN_1	4142.125–4177.125	4080.125–4117.625	4244.125–4284.125	M
CN_2	4142.125–4177.125	4083.875–4096.375	4244.125–4284.125	M
Ca4227	4222.250–4234.750	4211.000–4219.750	4241.000–4251.000	A
G4300	4281.375–4316.375	4266.375–4282.625	4318.875–4335.125	A
Fe4383	4369.125–4420.375	4359.125–4370.375	4442.875–4455.375	A
Ca4455	4452.125–4474.625	4445.875–4454.625	4477.125–4492.125	A
Fe4531	4514.250–4559.250	4504.250–4514.250	4560.500–4579.250	A
C4668 †	4634.000–4720.250	4611.500–4630.250	4742.750–4756.500	A
Hβ	4847.875–4876.625	4827.875–4847.875	4876.625–4891.625	A
Fe5015	4977.750–5054.000	4946.500–4977.750	5054.000–5065.250	A
Mg_1	5069.125–5134.125	4895.125–4957.625	5301.125–5366.125	M
Mg_2	5154.125–5196.625	4895.125–4957.625	5301.125–5366.125	M
Mg *b*	5160.125–5192.625	5142.625–5161.375	5191.375–5206.375	A
Fe5270	5245.650–5285.650	5233.150–5248.150	5285.650–5318.150	A
Fe5335	5312.125–5352.125	5304.625–5315.875	5353.375–5363.375	A
Fe5406	5387.500–5415.000	5376.250–5387.500	5415.000–5425.000	A
Fe5709	5696.625–5720.375	5672.875–5696.625	5722.875–5736.625	A
Fe5782	5776.625–5796.625	5765.375–5775.375	5797.875–5811.625	A
Na D	5876.875–5909.375	5860.625–5875.625	5922.125–5948.125	A
TiO_1	5936.625–5994.125	5816.625–5849.125	6038.625–6103.625	M
TiO_2	6189.625–6272.125	6066.625–6141.625	6372.625–6415.125	M

Table 3.2: Bandpass definitions for the Lick indices calculated here (as defined in Trager, 1997). Each index has a type A or M signifying atomic and molecular indices, respectively. Atomic indices are measured in and molecular indices are measured in magnitudes. Note that these are air wavelengths. Also note that the Fe4668 index has been renamed C4668 as it is more sensitive to carbon that iron (Tripicco and Bell, 1995).

spectrum is not necessarily the best possible spectrum that could be synthesised to match the STELIB spectrum, but simply the spectrum from my grid with the closest match in physical parameters. This means it does not take into account any particular properties of the STELIB spectrum that could in principle be modelled and which may affect the line indices. However, the comparison does give an indication of the level of mismatch to be expected when comparing observed stellar spectra with a grid of synthetic spectra like mine. Such mismatches are an inevitable consequence of any automated comparisons between a grid of model spectra and the vast number of spectra being made available from large surveys like the SDSS.

I have calculated Lick indices and their associated errors for a set of 9473 SDSS galaxies from the Early Data Release (Stoughton et al., 2002). The purpose of this was to compare the scatter between the Lick index values for the STELIB and Kurucz spectra with the expected accuracy of the indices measured from observed galaxy spectra. I have found that the random error (as calculated by Equations 4.17 and 4.18 in Chapter 4) associated with each index measured in the SDSS spectra, is of the same order of magnitude as the average offset between the Kurucz and STELIB index measurement. This suggests that the indices measured from galaxy spectra synthesised from the Kurucz spectra will have at least comparable accuracy to those measured with SDSS, and so my grid of stellar spectra is well matched to the SDSS galaxies.

3.6 Discussion

I have generated a grid of theoretical spectra from the Kurucz model atmospheres. Since the intended use of these spectra is in population synthesis and stellar classification, I have made several comparisons to check the validity of using the spectra for these purposes. The broad-band properties of the spectra compare well with observed spectra, as do the line index measurements. The comparisons do not guarantee the detailed accuracy of the Kurucz spectra as models of observed stellar spectra. Rather, they demonstrate that my new, high resolution Kurucz spectra are as good for use in population synthesis as the commonly used library of 20 spectra. The advantage of these spectra over the previously available Kurucz spectra is that they allow the modelling of spectral line features such as the Lick indices.

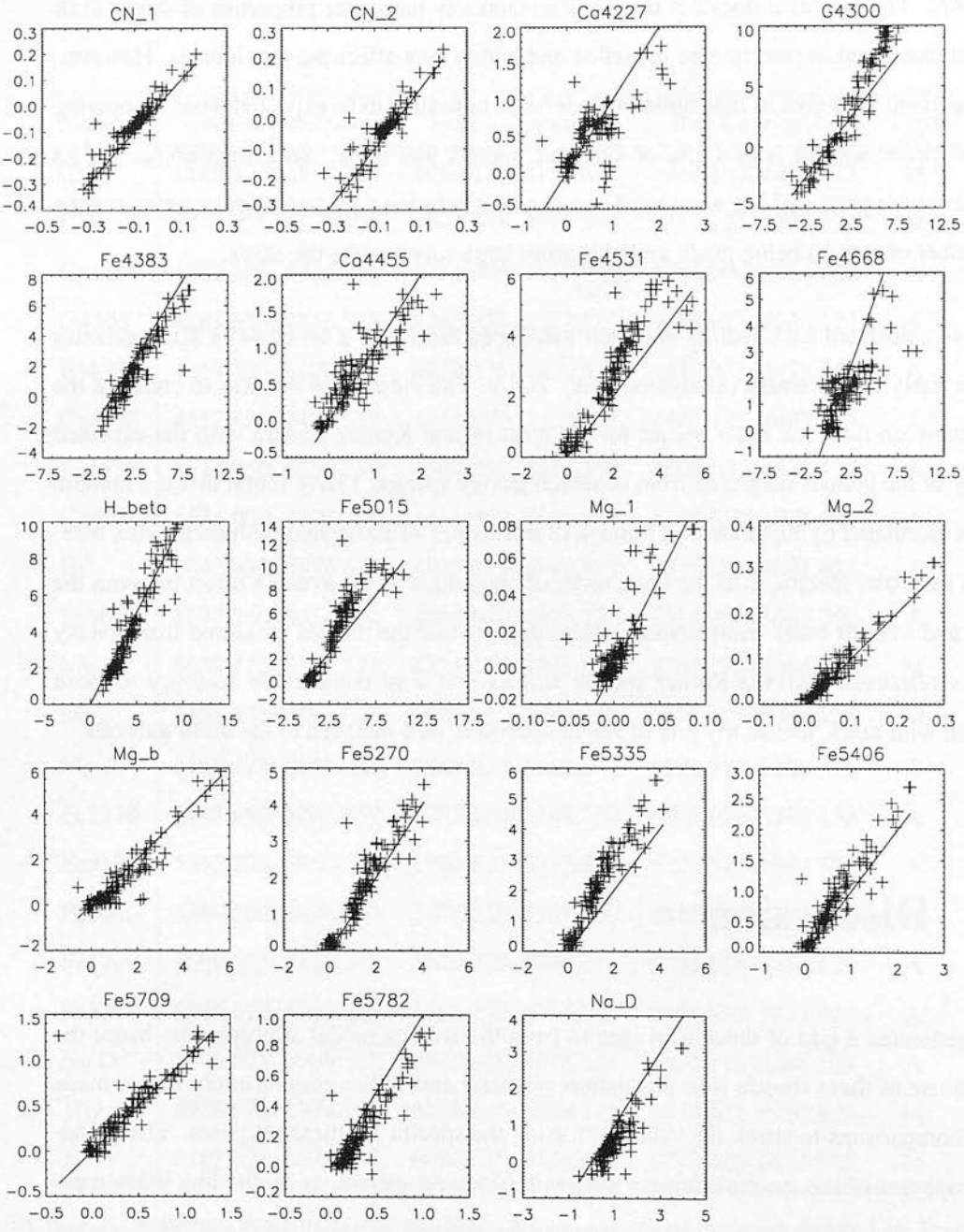

Figure 3.8: Each plot shows the correlation between the Lick index calculated on the STELIB spectrum (x-axis) and the closest matching Kurucz spectrum from my grid (y-axis). The solid line is the line '$x = y$' for comparison. I have not included the TiO indices for reasons discussed in the text. The offset for each index is given in Table 3.3.

Name	Mean value	Av. Abs. Err.	Med. Abs. Err.	Type
CN_1	−0.105	0.03	0.03	M
CN_2	−0.055	0.03	0.01	M
Ca4227	0.552	0.25	0.03	A
G4300	2.350	1.49	0.42	A
Fe4383	2.724	0.86	1.01	A
Ca4455	0.599	0.22	0.30	A
Fe4531	1.880	0.74	0.05	A
C4668	1.794	0.96	2.38	A
Hβ	4.456	0.68	0.60	A
Fe5015	3.444	1.35	0.09	A
Mg_1	0.004	0.01	0.00	M
Mg_2	0.061	0.01	0.02	M
Mg *b*	1.314	0.37	0.06	A
Fe5270	1.419	0.34	0.05	A
Fe5335	1.302	0.78	0.14	A
Fe5406	0.622	0.23	0.06	A
Fe5709	0.399	0.09	0.07	A
Fe5782	0.333	0.12	0.49	A
Na D	1.051	0.48	1.81	A

Table 3.3: Statistical comparison between the STELIB Lick indices and those of their Kurucz matches. *Column 2* shows the mean value of the STELIB index. *Column 3* shows the average absolute offset between the Kurucz and STELIB indices. *Column 4* shows the median absolute offset between the Kurucz and STELIB indices.

One this to note is that these stellar spectra have been generated with scaled-solar abundance ratios (*i.e.* based on the stars in the solar neighbourhood). Abundance ratios measure the proportions of specific elements with respect to each other and so give a more detailed information about a galaxy, rather than just a overall metallicity (*e.g.* [Mg/Fe] and [Na/Fe] rather than [M/H]). As both observational and synthetic spectra have become available at higher resolutions, the more subtle effects of varying abundance ratios have become apparent. This is

important when using synthetic stellar spectra to model observed stellar populations as observational evidence shows that the abundance ratios in other galaxies (or in fact in other regions of our own galaxy) are often very different from those in the solar neighbourhood. For example, measurements of the Lick indices in elliptical galaxies showed that the relationship between magnesium and iron abundances is different to that obtained using population synthesis models which assumed solar abundance ratios (Worthey et al., 1992). Following studies also supported the fact that the abundance of magnesium for a given iron abundance was higher in elliptical galaxies than in the synthetic models. For a review of observational studies of abundance ratios in galaxies see Peletier (1999) and Worthey (1998). Most current libraries of spectra have been generated with scaled-solar abundance ratios. However, producing grids of high resolution spectra with alternative abundance ratios (such as Oxygen-enhanced, light element enhanced or alpha-enhanced) is an important current area of research (see, for example Barbuy et al., 2003; Houdashelt and Bell, 2003; Thomas et al., 2003).

When using my new spectra at high resolutions, it should be recognised that the spectra were generated using line lists that include 'predicted' lines. This is necessary to reproduce the broadband colours of the spectra accurately. However, it does mean that many of the individual lines present at high resolutions do not have measured properties. Also, the line lists that I used (such as LOWLINES) are known to have problems with the values for specific lines. As this mostly involves weak lines, it should not present any difficulties for population synthesis at the resolution of the SDSS. More accurate properties for these lines could be obtained using alternative values, for example from the Vienna Atomic Line Database (VALD) (Kupka et al., 2000).

I intend to extend the library to the lower temperature models in which TiO lines become important and also generate spectra for the NOVER models as these are more accurate. In the next chapter I include the Kurucz spectra in a larger library for population synthesis — a higher resolution version of that done by Lejeune et al. (1997).

CHAPTER 4

Properties of composite stellar systems

4.1 Introduction

In the first two chapters I have focused on stellar spectra. One of the main aims of generating the high resolution Kurucz spectra was to use them as input spectra in population synthesis software and hence generate galaxies at a higher resolution that what has previously been available. In this chapter I investigate different methods of parameterising galaxies, taking advantage of these high resolution spectra. In this section I will give some background to different types of parameterisation methods and how galaxy classification relates to stellar classification. In Section 4.2 I create a library of stellar spectra for use in population synthesis, which incorporates my high resolution Kurucz spectra as well as several other libraries. Then in Section 4.3 I investigate two methods of empirical population synthesis for working out the stellar content of a galaxy based on its spectrum: least squares minimisation and direct inversion. In Section 4.4 I discuss the population synthesis package PEGASE. Finally, in Section 4.5 I discuss issues associated with measuring the Lick indices, in preparation for the applications in Chapter 5.

The aim of galaxy parameterisation is to obtain useful physical information about a galaxy

by studying its spectrum. This can range from measuring specific emission lines, to doing principal component analysis. In Chapter 2 I investigated different methods of stellar classification, partly because it is an interesting problem in its own right and partly as a precursor to studying galaxy classification. However, although many of the same techniques can be applied to both problems, galaxy parameterisation is actually quite a different problem to stellar classification. Stars are simpler systems than galaxies and have a well defined classification system (the MKK system) which means that classifying them is a supervised learning problem. If we want to obtain the physical parameters of stars, there is also a well defined three dimensional plane of effective temperature, surface gravity and metallicity in which all the stars lie. Hence, again, this is a supervised learning problem. However galaxies are much more complex systems, and the only comprehensive classification schemes (such as Hubble type) are based on morphology. This makes parameterising and classification of galaxy spectra an unsupervised learning problem. In other words, it is necessary to discover or define parameters that will be useful for determining the properties of a galaxy from its spectrum.

Probably the most commonly used method of classifying galaxies is by morphology. The aim of morphological classification is to gain insight into the formation and evolution of galaxies. Almost all morphological classification systems are based on the original scheme by Hubble (1926) and involve looking at properties such as the presence and nature of bars, rings and spiral arms or measurements of the bulge-to-disk ratio and similar properties. A simplified schematic of the Hubble classification system is shown in Figure 4.1. At one end of the scheme are elliptical galaxies and at the other are spiral galaxies. The usefulness of morphological classification is limited for a number of reasons: orientation of the galaxy relative to the observer can make it hard to establish the ellipticity; the quality of the image affects greatly the ability to pick out potentially faint features like bars and spiral arms; and when going to higher redshifts it also becomes much harder to determine the morphology of the galaxies. Modern morphological classification generally involves quantifying the morphology by some statistic, which is necessary to encompass the subtle variations that you get with a massive survey. See for example Abraham et al. (2003) who have morphologically classified galaxies from the SDSS.

Provided the signal to noise ratio is good enough, spectra provide a much more robust source of information than images for classifying galaxies. This is particularly true for large

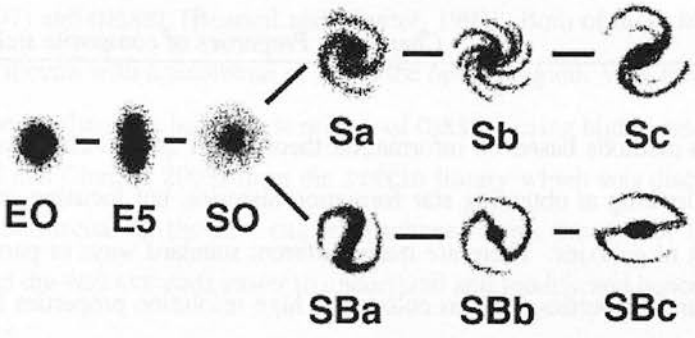

Figure 4.1: The Hubble *tuning fork* diagram for morphological classification of galaxies. Image source: `http://btc.montana.edu/ceres/html/galhubble.html`.

surveys since spectra work equally well at any redshift. Also, galaxy morphology does not directly give us any information about what types of stars a galaxy is comprised of. Morgan (1958) first proposed a classification scheme to unite morphological type and spectral type of galaxies. This system was based on how well the galaxies correlated with stars of different spectral types. In other words, it was a measure of what type of stars made up the greatest portion of the light emitted from the galaxy. One result from combining Hubble's scheme with spectral type was the observation that most of the light from giant elliptical galaxies came from red giant stars and most of the light from spiral galaxies came from the younger hotter stars. Studies of large numbers of galaxies show a relatively tight relationship between colour and morphology (Roberts and Haynes, 1994), with the colour going from red to blue as you move along the Hubble tuning fork from elliptical galaxies to spirals and irregulars. Using this relationship, the morphological class can be estimated from the photometric colours of a galaxy, rather than having to analyse the morphology directly.

If we want to know in more detail what makes up a given galaxy we need to look at its spectrum. The spectrum is essentially just the integrated light of all the stars in a galaxy (as well as the effects of dust absorption *etc.*) and so in principle contains all the information about the galaxy's composition. In practice, the problem is how to extract this information effectively. Most of the work in this area focuses on trying to determine either the star formation histories or the stellar composition of the galaxies. Methods for obtaining star formation histories range from more traditional methods such as using absorption line indices (see, for example Kauff-

mann et al., 2003) to methods based on information theory such as MOPED (Heavens et al., 2000). I will not be looking at obtaining star formation histories, but focusing on determining the stellar content of galaxies. There are many different standard ways of parameterising spectra, from broadband properties (such as colours) to high resolution properties (such as the Lick indices). Then, the usual way for determining their stellar composition or star formation history is through comparison with a grid of synthetic galaxy spectra for which these properties are known, for example, Kauffmann et al. (2003).

There are two different types of population synthesis, empirical population synthesis and evolutionary population synthesis. Empirical population synthesis was first done by Whipple (1935). Its main aim is to determine the relative proportions of stars of different spectral types and luminosities that make up the galaxy. Two different empirical population synthesis techniques will be discussed in Section 4.3. Evolutionary population synthesis refers to the use of population synthesis code such as PEGASE (Fioc and Rocca-Volmerange, 1997) and GISSEL (Bruzual and Charlot, 1993, 2003). These start with an initial mass function and stellar evolutionary tracks. These methods (specifically focusing on PEGASE) will be discussed further in Section 4.4.

4.2 A library of stellar spectra for population synthesis

A galaxy synthesis package can use either a grid of synthetic spectra, or a grid of observed spectra. Using synthetic spectra has the advantage that they have even coverage over a wide range of physical parameters. However, the galaxies generated are of course subject to any problems and inaccuracies with the input stellar spectra. Using observed spectra guarantees that they are representative of real spectra, but has the disadvantage that is it hard to get a homogeneous observed catalogue. Also, the spectra are subject to observational and calibration issues.

The two most commonly used population synthesis packages are PEGASE (Fioc and Rocca-

Volmerange, 1997) and GISSEL (Bruzual and Charlot, 1993). Both of these libraries allow the user to generate spectra with a resolution of 20 in the optical region. Very recently (during the writing of this thesis) there has been a new release of GISSEL, using higher resolution observed spectra (Bruzual and Charlot, 2003) from the STELIB library which was discussed in Section 3.5. I will not be discussing the new GISSEL package in this thesis. Of the two software packages, I found the PEGASE code easier to understand and modify and hence I chose to work with this package.

PEGASE has two input libraries of synthetic stellar spectra. The first (`stellibLCB-cor.dat`) is the Lejeune et al. (1997, 1998) library (referred to hereafter as L98). The L98 library is a compilation of several spectral libraries covering different ranges in parameter space and has 4422 spectra in total. The bulk of the main sequence stars are the model flux distributions from the grid of Kurucz atmospheres. The coverage of the Kurucz synthetic spectra is shown in Figure 3.1. For comparison, I have also plotted the coverage of the new observational library used by Bruzual and Charlot (2003) in the latest release of GISSEL. The M-giants (low $T_{\rm eff}$, low log(g)) are constructed from the spectra of Bessell et al. (1989, 1991). The M-dwarfs (low $T_{\rm eff}$, high log(g)) are from the Allard and Hauschildt (1995) grid of spectra. The coverage of these three libraries is shown in Figure 4.2 which is taken from Lejeune et al. (1998). The second input library (`stellibCM.dat`) consists of 31 extremely hot stars with $T_{\rm eff} \geq 60\,000$ K, taken from Clegg and Middlemass (1987). All the spectra in the PEGASE input library cover the wavelength range $\lambda = 91 - 1\,600\,000$. The resolution of the spectra varies with wavelength, as shown in the top panel of Figure 4.3. In the optical region the resolution is 20 .

One limitation of the available libraries is that the resolution (20) is insufficient for comparisons with high resolution observed galaxy spectra. To overcome this I attempted to build a high resolution version of the L98 library, for use in population synthesis with PEGASE. Where possible I replaced the optical region of each spectrum ($\lambda = 3010 - 9990$), which was previously at 20 resolution, with a 2 resolution section. This is demonstrated in the bottom panel of Figure 4.3. Due to limitations in the 2 spectra available, this was possible for only 3538 out of the 4422 PEGASE spectra. I falsely interpolated the remaining spectra (884 from L98, plus the 31 extremely hot stars) to the higher resolution grid. The full grid of spectra used by PEGASE

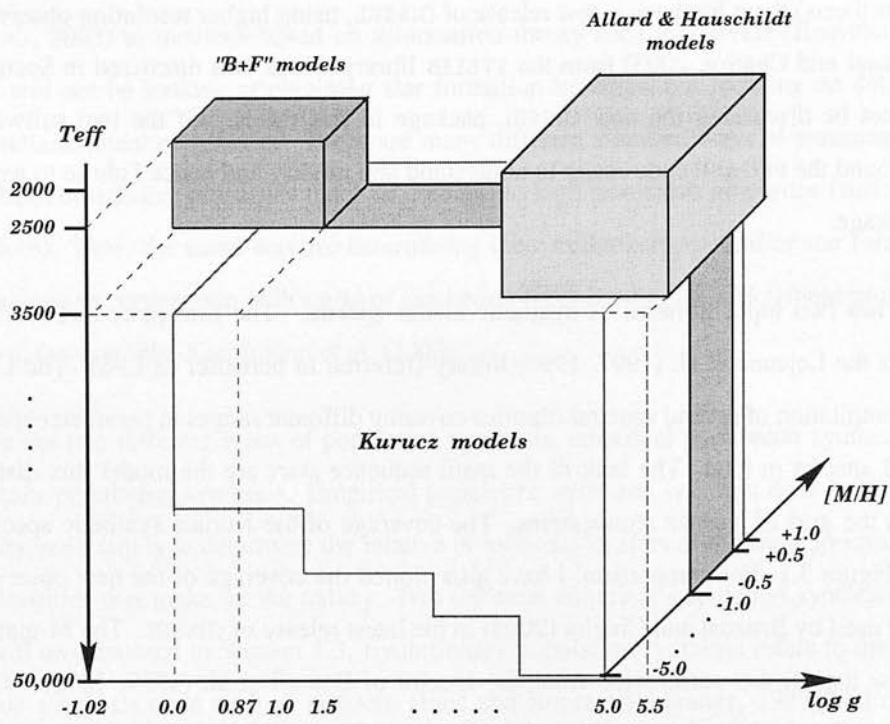

Figure 4.2: Coverage of the L98 library in stellar parameter space. The B+F models are M-giants and the Allard & Hauschildt models are M-dwarfs. Image source: Lejeune et al. (1998).

is shown in Figure 4.4. The 884 spectra that are not available at the higher (2) resolution, and hence that have been interpolated, are shown in Figure 4.5. Most of the missing spectra are the low temperature Kurucz spectra. These spectra require the inclusion of TiO lines, and hence take a long time to generate (as discussed in Chapter 3). However, it is possible to generate these spectra, and I plan to do at a later date when I get the time and computing resources. I will discuss each of the catalogues that the spectra have been obtained from in the following section.

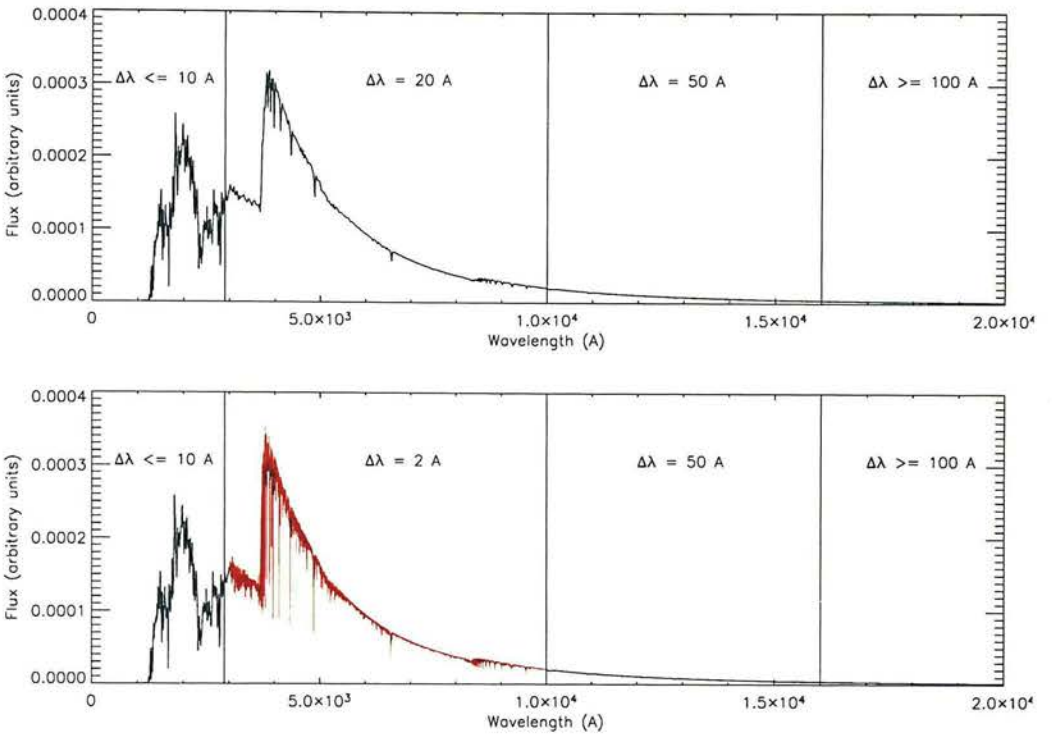

Figure 4.3: Top panel shows a typical input spectrum for PEGASE (with parameters $T_{\rm eff}$ = 9000, log(g) = 2.0, [Fe/H] = 1.0). The vertical lines divide sections with different resolutions. The bottom panel shows the new spectrum, with the optical section (λ = 3010 – 9990) replaced with a 2 spectrum.

4.2.1 The stellar spectra

Kurucz spectra

Most of the PEGASE input spectra have been generated from the Kurucz model atmospheres. As discussed in Chapter 3, I have generated a new grid of high resolution ($\lambda/\Delta\lambda$ = 250 000) Kurucz spectra. This covers most of the original grid of stellar spectra. Due to the length of time needed to generate the spectra with TiO lines included (which affects all low temperature spectra) I have not covered the entire grid and am still missing spectra with $T_{\rm eff} \leq$ 5000 K. The process of generating these spectra is described in detail in Chapter 3. Once generated at high resolution, the spectra were top-hat smoothed to 2 for use in PEGASE. A high resolution

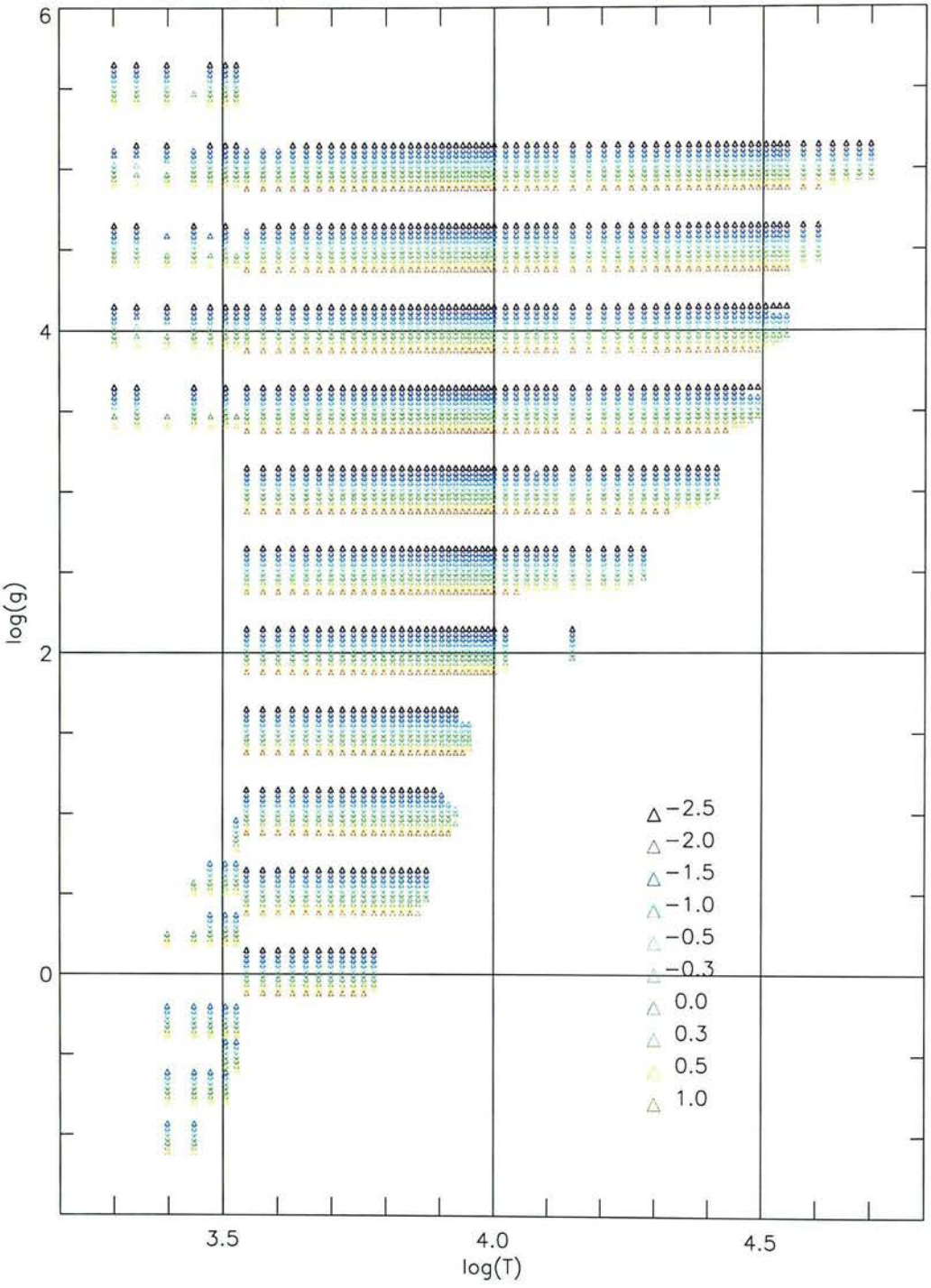

Figure 4.4: The coverage of the PEGASE input spectra in parameter space. The different colours show the metallicity for a given $\log(T)$ and $\log(g)$ as shown in the key. Most of the spectra are from the Kurucz grid. The M-giants (bottom left) are the Fluks spectra, the M-dwarfs are from the NextGen grid.

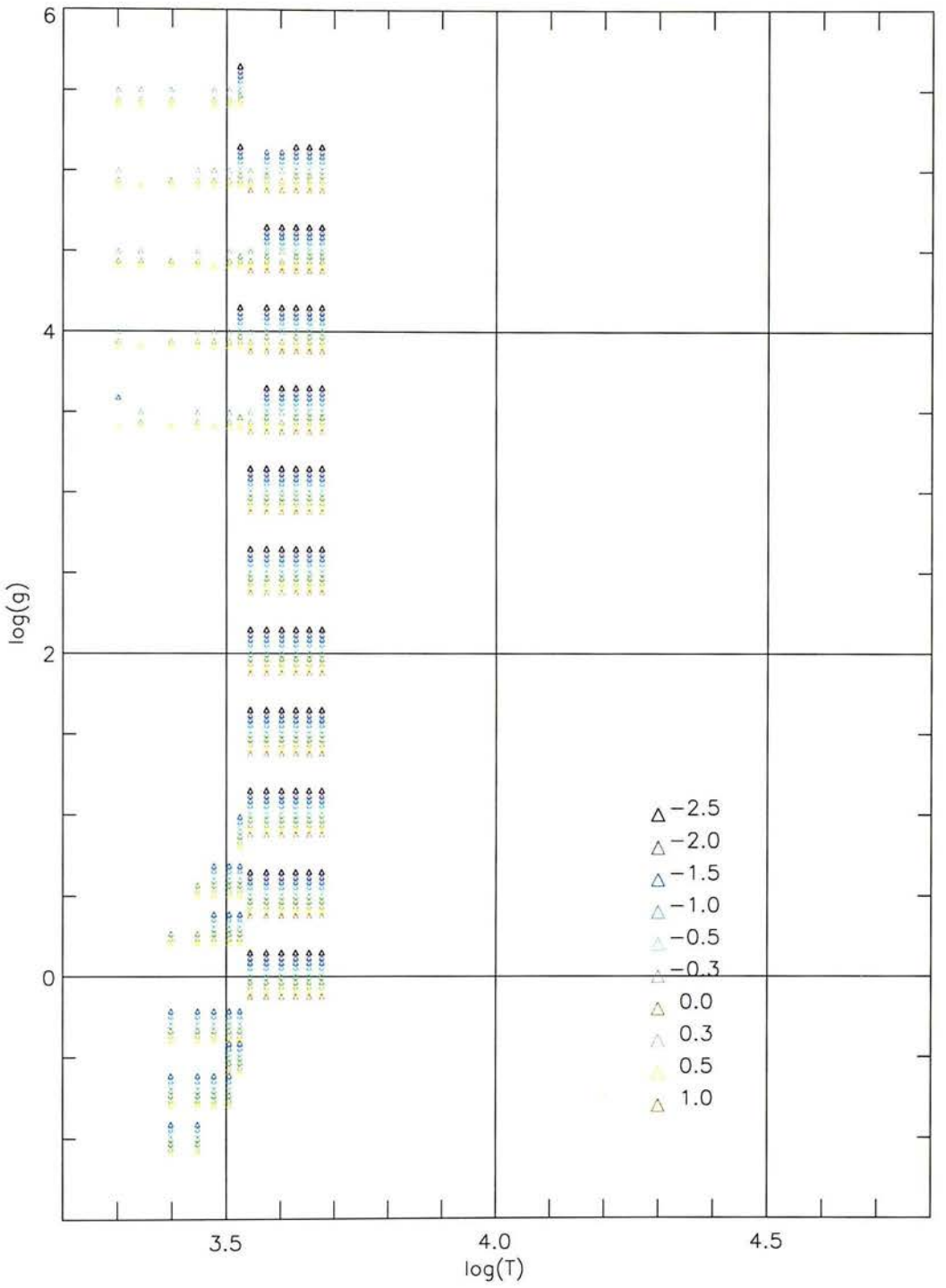

Figure 4.5: The same as the previous figure, but showing only the 884 spectra that were not available at the higher resolution.

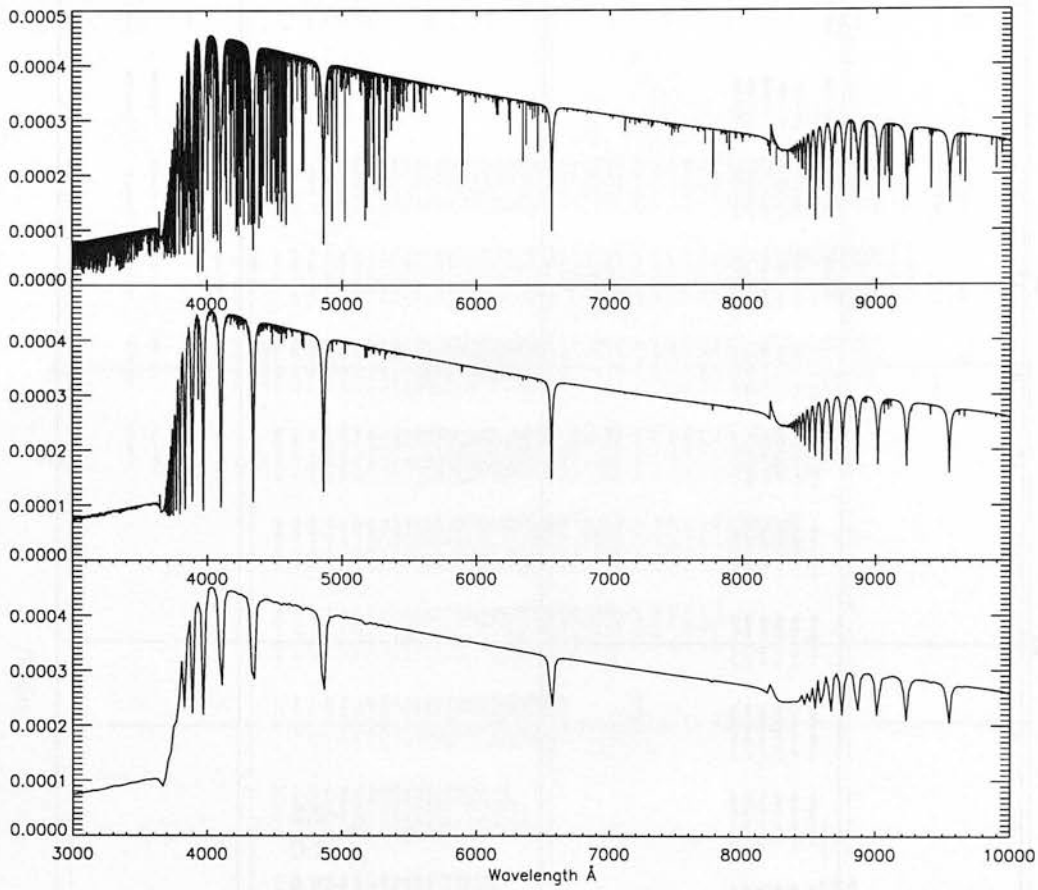

Figure 4.6: A high resolution Kurucz spectrum (top) and its smoothed versions at 2 (middle) and 20 . The spectrum has parameters (8200, 3.0, -1.5). The flux is in arbitrary units.

spectrum and its smoothed counterparts are shown in Figure 4.6.

Clegg and Middlemass spectra

The very hot stars with $T_{\rm eff} \geq 60\,000$ K were obtained from Clegg and Middlemass (1987). These are NLTE synthetic spectra, which were generated to model the central stars in planetary nebulae, where the assumptions of gray-like atmospheres and LTE are not valid. These spectra are essentially black body curves, as can be seem from the sample spectra in Figure 4.7. They were not available at higher resolution, however since they are almost featureless, I have simply resampled these spectra to 2 resolution for inclusion in my high resolution library.

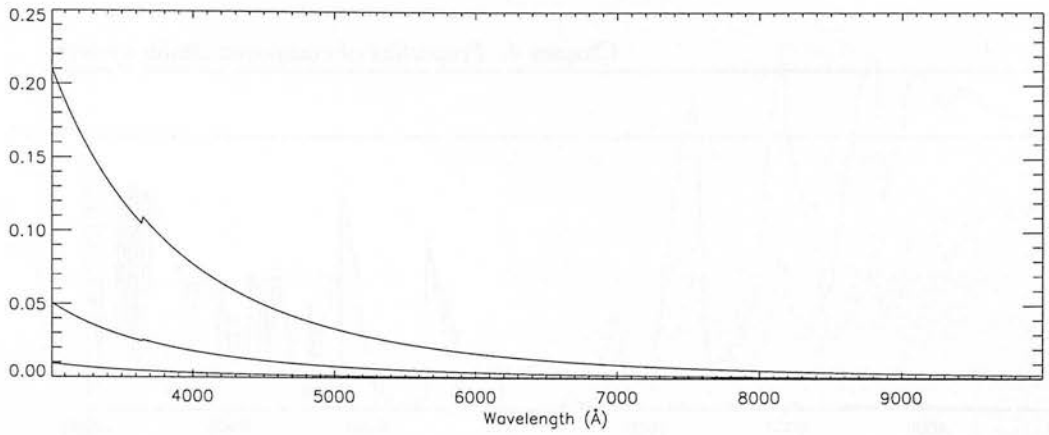

Figure 4.7: Three examples of NLTE spectra from the Clegg and Middlemass (1987) catalogue. The spectra have ($T_{\rm eff}$,log(g)) = (60 000, 5.0), (100 000, 5.0) and (180 000, 6.5) going from the bottom curve to the top curve respectively. The flux is in arbitrary units.

Hauschildt spectra

Most of the M-dwarfs in L98 are synthetic spectra from Allard and Hauschildt (1995). These spectra are known as the 'Extended (version 3.0)' models and are now obsolete (see Peter Hauschildt's webpage[1].) They have been superseded by the 'NextGen (version 5.0)' models (Hauschildt et al., 1999a,b). The NextGen models with solar metallicity were available when L98 was created, and so they were incorporated into that library. More of the NextGen models are now available, but do not cover exactly the same range in parameter space as the old set of models. One possibility was to continue using the version 3.0 spectra but this was not recommended (Hauschildt, private communication). Hence I decided to use the NextGen spectra where available. This does mean that some of the spectra are still being taken from the old models. However, since many people use the current L98 catalogue for population synthesis, this will be no worse that what is already being done. Figure 4.8 demonstrates the kind of differences between the Extended (version 3.0) models and the NextGen (version 5.0) models. The differences between the two sets of spectra are quite significant, particularly for the lower temperature stars. The NextGen spectra are already on a 2 grid and so no smoothing or resampling was required.

[1] `http://dilbert.physast.uga.edu/~yeti/mdwarfs.html`

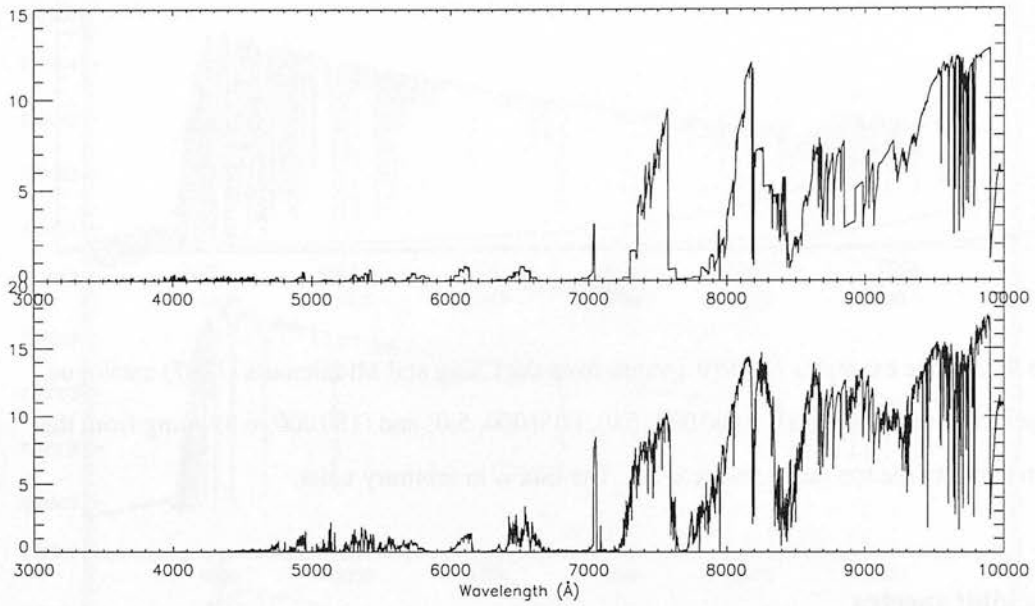

Figure 4.8: A comparison of the old 'version 3.0' (top) and new 'version 5.0' (bottom) Hauschildt spectra. The spectrum has parameters (2200, 3.5, -2.0). Note that there is also a resolution difference: the old spectra are at 20 resolution whereas the new spectra are at 2 resolution. The flux is in arbitrary units.

Bessell and Fluks spectra

The M-giants (covering the temperature range 2500 – 3800 K) in L98 come from a combination of the Fluks et al. (1994) and Bessell et al. (1989, 1991) catalogues. These catalogues were combined by Lejeune et al. (1997) in order to compensate for the weaknesses in both of them. The Fluks et al. (1994) catalogue is based on observations of 97 M-giants. These spectra were observed between 3800 and 9000 at a resolution of $1300 < R < 9000$ over that range. This is equivalent to sampling of 1 – 3 / pix. A set of synthetic spectra were then generated using the SOSMARCS and POSMARCS code (Plez et al., 1992; Plez, 1992) with 10 912 sampling points between 990 and 125 000 . The observed spectra were used to calibrate the synthetic spectra, and then combined with them to create a grid of M-giant spectra over a wide wavelength range. The main limitation of the Fluks et al. (1994) library is that it is limited to stars of solar metallicity. The Bessell et al. (1989, 1991) spectra were computed from model atmospheres and have 405 wavelength points in the range 4910 – 40 900 . The library covers a range of

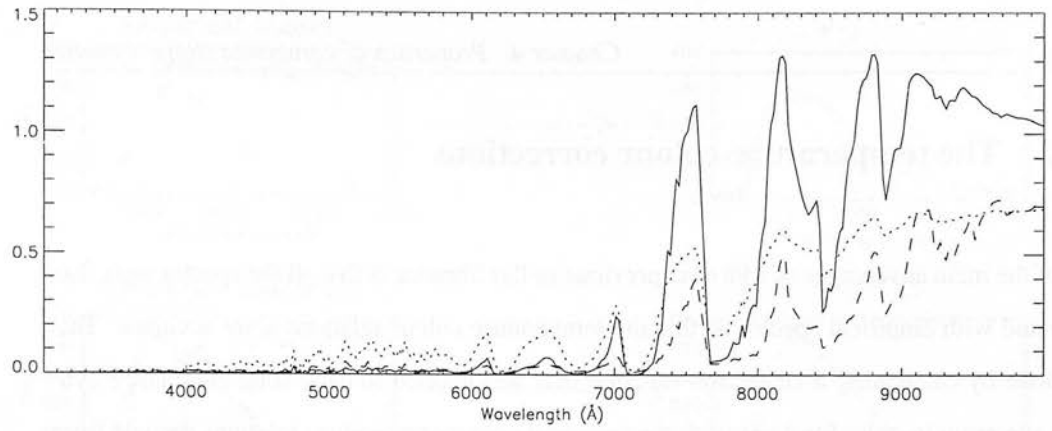

Figure 4.9: Examples of the B+F hybrid spectra made by combining the Bessell and Fluks libraries. The spectra have physical parameters ($T_{\rm eff}$, log(g), [M/H]) equal to *solid line*: (2800, -1.0, -1.5), *dotted line*: (3350, -0.3, -0.5) and *dashed line*: (3200, 0.6, 0.5) respectively.

metallicities and surface gravities, its main limitation being the wavelength range.

By interpolating over metallicities and making use of the overlapping wavelength ranges Lejeune et al. (1997) created a grid of 'B+F' hybrid spectra to cover the M-giants adequately. However, these spectra are not available at a high enough resolution for my requirements and so in this region of the parameter space I have falsely interpolated the spectra to 2 resolution. This is clearly not ideal, but M-giants only contribute a significant fraction of the total light from a galaxy in the latest stages of its evolution and so any errors caused by this will not significantly affect younger galaxies. Figure 4.9 shows examples of some of the B+F hybrid spectra that are used in L98. The spectra are dominated by TiO absorption, particularly in the red. Note that these spectra have already been corrected by Lejeune, as described in Section 4.2.2 below.

I investigated the possibility of covering this region of parameter space with spectra from a different source, such as the Houdashelt et al. (2000) models. However, there were no spectra with the appropriate resolution and wavelength coverage that covered the same region of physical parameters as the B+F spectra.

4.2.2 The temperature-colour corrections

One of the main advantages of L98 over previous stellar libraries is that all the spectra were flux calibrated with empirical spectra so that the temperature-colour relations were accurate. This was done by calculating a correction function that was applied to each solar-abundance synthetic spectrum in order for it to match the empirical colour-temperature relations derived from observed spectra. The empirical colour-temperature relations were obtained from a variety of sources (see, for example, Ridgway et al. (1980) for giants and supergiants, Schmidt-Kaler (1982) for main sequence stars). Broadband $UBVRIJHKL$ magnitudes were measured for each of the synthetic spectra, and a pseudo-continuum fit to these points. Then a correction function Φ_λ was derived by dividing the pseudo-continuum obtained from the empirical calibrations by the pseudo-continuum for the appropriate synthetic spectrum. This correction was applied by convolving with the original synthetic spectrum to obtain the corrected synthetic spectrum. This process is outlined in Figure 4.10 which is taken from Lejeune et al. (1997). For most of the main sequence spectra, this correction has a negligible effect. However, at lower temperatures there are significant changes to the shape of the continuum. This is demonstrated in Figure 4.11 which shows the result of correcting the spectra from a main sequence star and an M-dwarf.

In creating my high resolution library I have tried to maintain consistency with the 20 library as far a possible. Hence I experimented with an empirical correction procedure that would modify the continuum shape of the optical region of the spectrum to match that done by Lejeune et al. (1997). There are two versions of the L98 catalogue available, both the uncorrected and corrected spectra [2]. I measured the $UBVRIJ$ broadband magnitudes for each of the uncorrected and corrected spectra and created a pseudo-continuum for each spectrum by fitting the magnitude points with a polynomial function. I then defined a correction function by dividing the pseudo-continuum of the corrected spectrum by the pseudo-continuum for the uncorrected spectrum. I interpolated this correction function up to the same resolution as my new spectra (2) and then applied it by convolving it with the appropriate synthetic spectrum from my new library. Figure 4.12 shows a flow chart of this process.

[2]Data is available from the BaSeL ftp site `ftp://tangerine.astro.mat.uc.pt/pub/BaSeL`

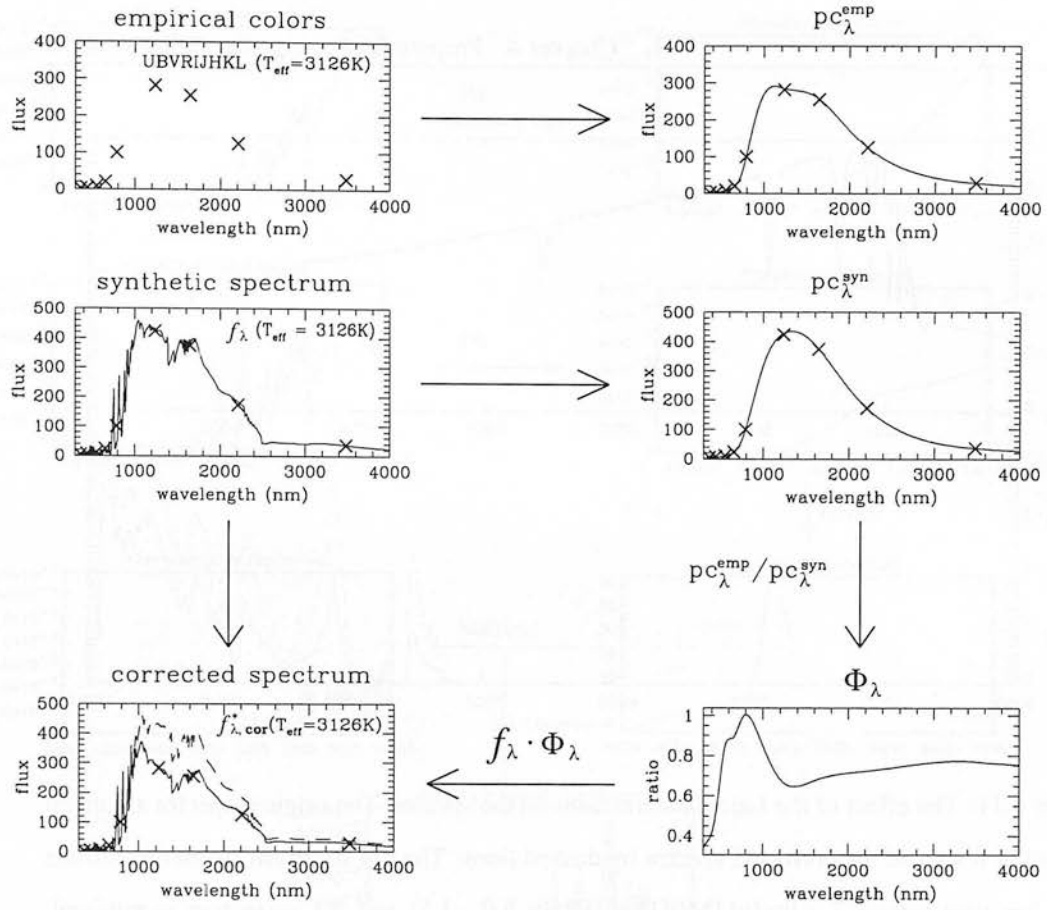

Figure 4.10: Outline of the correction procedure used by Lejeune et al. (1997).

For the higher temperature spectra this process was quite successful as fitting the broad-band fluxes gave pseudo-continua that accurately reflected the continuum shape. However, for lower temperature spectra it was more problematic. Applying the correction function at these temperatures resulted in the exaggeration of some features in the spectrum, which can be seen in Figure 4.12. This is because it is hard to fit an accurate continuum to the low temperature spectra, which are affected strongly by TiO absorption bands. This problem is also evident in the original corrections made by Lejeune et al. (1997) which, although resulting in agreement with the empirical temperature-colour relations, significantly modify the continuum shape of the low temperature stars (see Figure 4.11).

One alternative to these empirical corrections of the spectrum is to make a correction to the temperature of the spectrum. The problem with the synthetic spectra is that they do not fit the

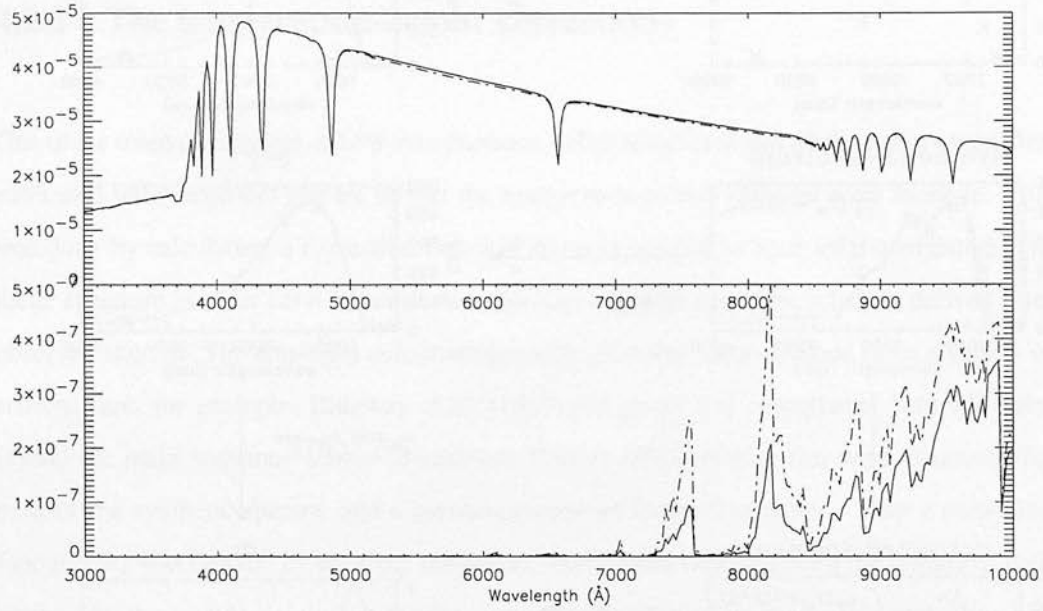

Figure 4.11: The effect of the Lejeune correction on the spectra. The original spectra are given by a solid lines and the corrected spectra by dashed lines. The top spectrum (from the Kurucz grid) has parameters ($T_{\rm eff}$,log(g),[M/H]) = (9250, 5.0, -1.5) and the correction is minimal. The bottom spectrum (from the NextGen grid) has parameters (2200, 3.5, -1.5) and here the correction is significant.

temperature-colour relations accurately. L98 has dealt with this by correcting the colours of the spectrum by adjusting the continuum. However, this process is subject to errors, such as in fitting the pseudo-continua. One possible alternative I considered was to make a correction to the temperature of the input spectra, rather than the spectra themselves.

To do this I first determined what size temperature correction was equivalent to the continuum change made by Lejeune's corrections. I took a corrected spectrum from L98 with parameters ($T_{\rm eff}$, log(g), [M/H]) equal to (7500, 1.0, 0.0) and then compared it with uncorrected spectra of different temperatures (and the same values of log(g) and [M/H]) to find which was the closest match (in terms of χ^2 difference). The corrected spectrum was closer to the uncorrected spectrum with the same temperature (7500 K) than to either of the neighbouring spectra (with temperatures 7250 K and 7750 K). I then interpolated between the 7250 K and 7750 K spectra to create a finer grid of spectra (with $T_{\rm eff}$ step equal to 50 K) and compared

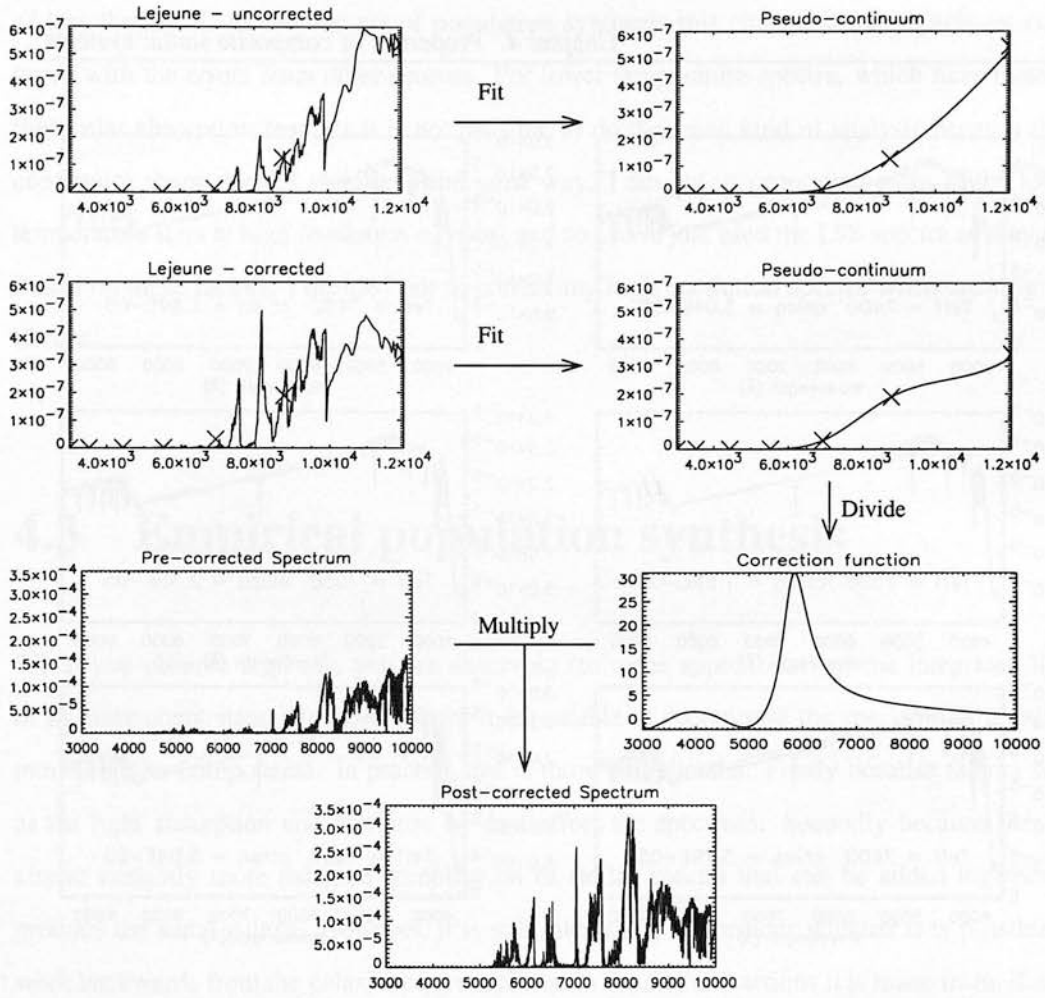

Figure 4.12: My correction process for the high resolution spectra. This example is for a spectrum with parameters (2200, 3.5, -1.5). The crosses show the measured broadband fluxes for the *UBVRI* bands, as well as the end points for the section of the spectrum I am correcting (3000 and 12 000).

the corrected spectrum with each of these. Figure 4.13 shows a set of these interpolated spectra (between 7400 K and 7650 K) overplotted with the corrected spectrum at 7500 K. It is clear from visual inspection that the best matching spectrum is the one with $T_{\rm eff}$ = 7500 K, the same as the corrected spectrum. To quantify this I have also shown the value for χ^2 for each pair of

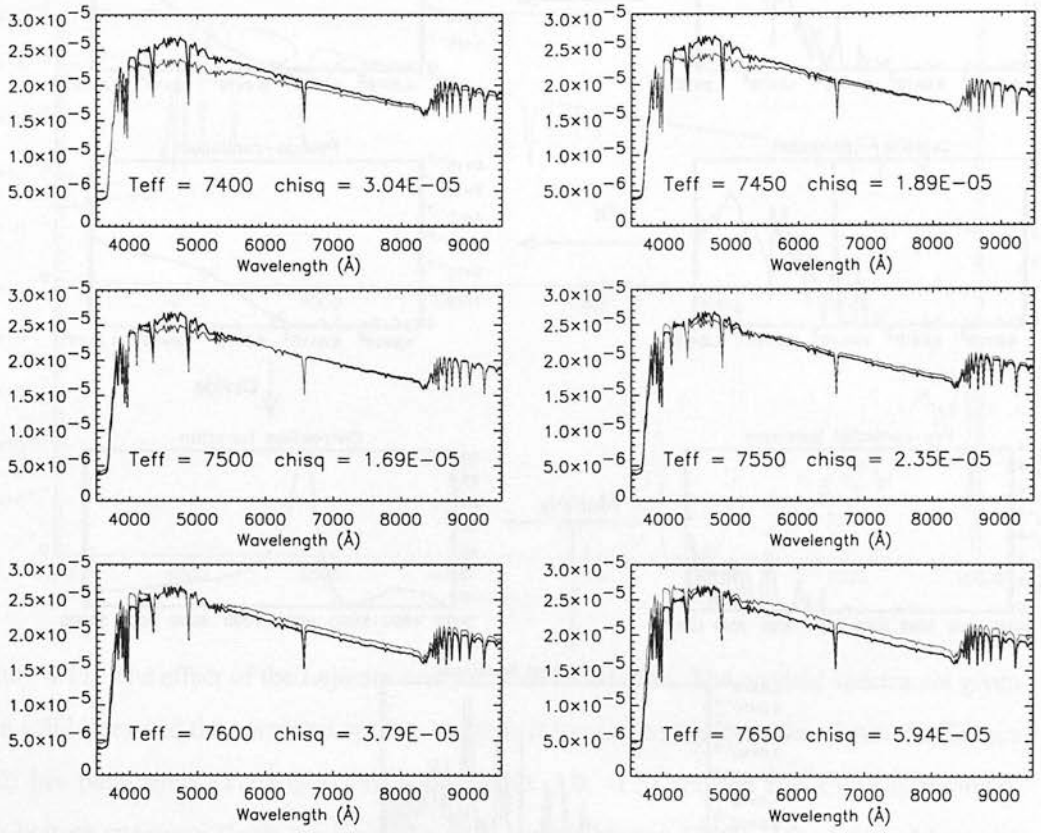

Figure 4.13: Kurucz temperature-colour corrections. The black spectrum is the same in each plot — a corrected spectrum from L98, with parameters ($T_{\rm eff}$, log(g), [M/H]) = (7500, 1.0, 0.0). The red lines are uncorrected spectra for the same surface gravity and metallicity but for a different temperature in each case (as given in the plot annotation). The χ^2 difference between each pair of spectra is also given. The flux is in arbitrary units.

spectra,[3] where

$$\chi^2 = \sum_{i=0}^{n} \frac{(S_i - C_i)^2}{C_i} \,. \tag{4.1}$$

These comparisons show that the difference introduced in the continuum is equivalent to a change in temperature of less that 50 K, for a spectrum of this temperature.

For the higher temperature spectra the L98 corrections correspond to a temperature change

[3]It should be noted this is not entirely accurate as a measure of goodness of fit, since it assumes that the error is proportional to the square root of the signal which does not apply here. Hence, the values of χ^2 shown here will be artificially lower for spectra with fit better in the blue than for those that fit better in the red.

of less that 50 K. In the context of population synthesis this change is not significant compared with the errors from other sources. For lower temperature spectra, which have massive molecular absorption features it is not possible to do the same kind of analysis because their continuum shape doesn't change in the same way. I am not incorporating most of the lower temperature stars at high resolution anyway, and so I have just used the L98 spectra as they are. Based on these factors, I decided not to correct my high resolution spectra when creating my library.

4.3 Empirical population synthesis

When you observe a galaxy, you are observing (to some approximation) the integrated light of its component stars. Hence in theory it is possible to decompose the spectrum of a galaxy into its stellar components. In practice this is more complicated. Firstly because factors such as the light absorption and emission by dust affect the spectrum. Secondly because there is almost certainly more that one combination of stellar spectra that can be added together to produce the same galaxy. However, it is still interesting to consider whether it is possible to work backwards from the galaxy spectrum to obtain the stellar fractions it is made from, if only to demonstrate that more sophisticated methods are needed.

Empirical population synthesis was first proposed by Whipple (1935). Early work focused on determining the nature and distribution of the two main populations of stars (Population I and Population II) in each galaxy (Baade, 1944, see, for example). Population I stars tend to be luminous, hot and young, concentrated in the disks of spiral galaxies. They are particularly found in the spiral arms. Population II stars tend to be older, less luminous and cooler than Population I stars, and are found in globular clusters and in the central regions of galaxies. These efforts were developed later by various people including Faber (1972, 1973), Aaronson et al. (1978) and Gunn et al. (1981) so that a galaxy's composition could be found in terms of all different types of stars, rather than just Population I and II. The most successful results have been obtained by Pickles (1985). One more recent attempt at this type of approach is by Goerdt and Kollatschny (1998) who use a modified linear simplex algorithm to fit synthetic

galaxy spectra. Another is presented in the series of papers by Pelat (1997, 1998); Moultaka and Pelat (2000) who also provide a formalism for error analysis in the resulting solutions.

Empirical population synthesis is so named because it is based on working only with the spectra of the galaxies and of stars and hence is largely independent of theory. For example, the work by Pickles (1985) uses stellar evolution theory only to set limits on the acceptable ranges of good fits to the composite population. This is in contrast to the evolutionary approach (discussed in the next section) which assumes perfect knowledge of stellar evolution. The biggest problem affecting both methods is trying to determine a unique solution. This problem is examined by Schmidt et al. (1991) in a review of the multi-minimisation procedures used by Bica (1988) and Schmidt et al. (1989). They find that input fractions can be reproduced reasonably well for some simple populations but worsen significantly when more complex populations (for example blue composite populations where spectral features below 3500 are important) are tried. The accuracy of the solutions obtained is determined primarily by the completeness of the stellar library and the accuracy of both the library spectra and the galaxy spectra.

In this section I discuss two methods for obtaining the stellar content of a galaxy spectrum, *least squares minimisation* (LSM) and *direction matrix inversion*. The least squares minimisation is essentially the same as that used by Pickles (1985), the aim being to see if having a larger library of stellar spectra at higher resolution make a difference to the kind of results we can obtain. To evaluate the accuracy of these methods, I have modified the PEGASE software so that it is possible to obtain the fractional contribution of each input stellar spectrum at any stage in the galaxy synthesis. There are 69 timesteps in the PEGASE evolutionary process and at each stage it is possible to get the galaxy (at a certain age) and also its stellar content at that age. For example, Figure 4.14 shows how the distribution of stars in $T_{\rm eff}$ changes as a galaxy ages. Initially the galaxy is made up primarily from hot stars, but as it ages this population decreases and a population of cool stars starts to dominate the light of the galaxy. We can then take a 'snapshot' of the composition at various ages, as demonstrated in Figure 4.15. In this figure the distribution in $T_{\rm eff}$ and $\log(g)$ is shown for a young galaxy and an older galaxy.

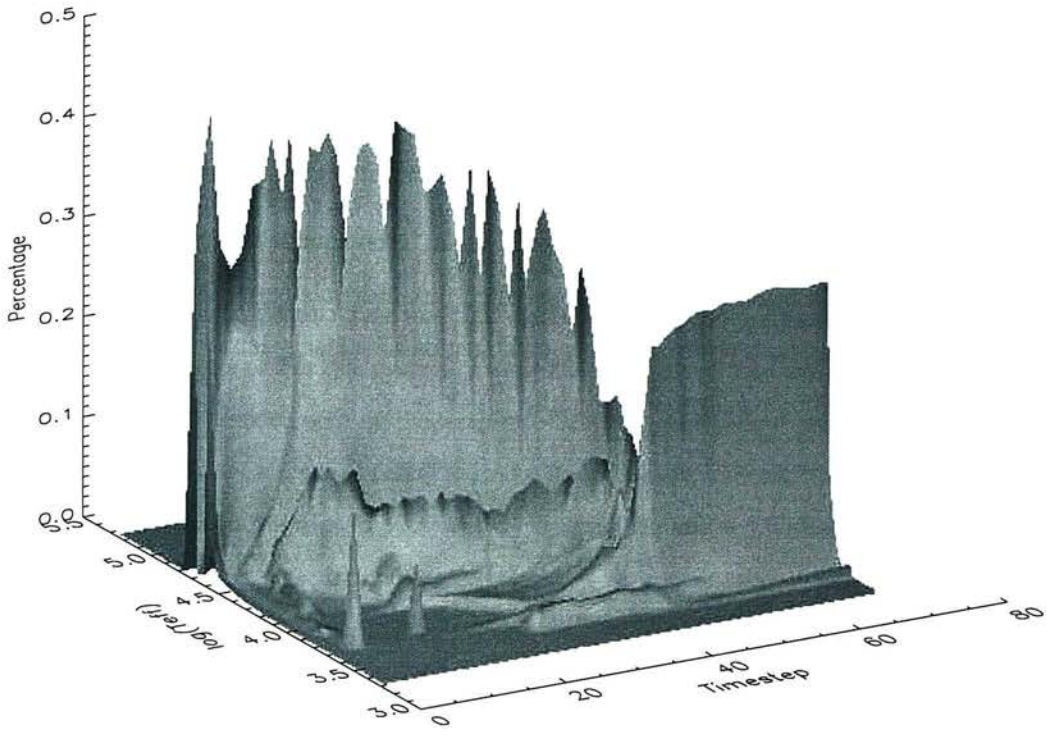

Figure 4.14: The distribution of starlight in $\log(T_{\rm eff})$ (y-axis) as it changes with the galaxy age, represented in PEGASE timesteps (x-axis). The z-axis gives the percentage of light contributed to the total by stars at each point on the $x-y$ grid, *i.e.* summing all the points gives 100%.

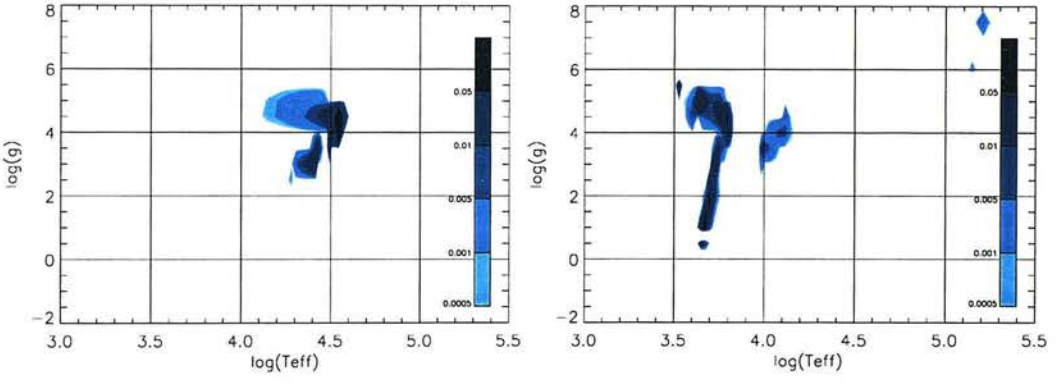

Figure 4.15: Two snapshots of the distribution of starlight in $T_{\rm eff}$ and $\log(g)$ for galaxies aged 0.01 Gyr (left) and 19 Gyr (right). The contour levels show the fraction of the galaxy's total light that is contributed by spectra in that region of parameter space.

4.3.1 Least squares minimisation

My approach here is based on that in Pickles (1985). Pickles' technique is to minimise a merit function which is the root mean square of the weighted flux residuals between the observed spectrum and the spectrum built up from a given combination of stellar spectra

$$\text{Merit} = \left(\frac{1}{n} \sum_{i=1}^{n} R_i^2 \right)^{1/2} \tag{4.2}$$

where

$$R_i = W_i \left(1 - \frac{S_i}{G_i} \right) . \tag{4.3}$$

In these equations G and S are flux vectors for the observed galaxy spectrum and the synthetic spectrum respectively. W is an optional weighting vector, specified at each flux point. At each point the synthetic flux vector, S, is given by

$$S_i = \sum_{j=1}^{g} X_j \cdot F_{ij} \tag{4.4}$$

where there are g stellar spectra, F_{ij} is the flux at wavelength point i of stellar spectrum j and X_j is the fractional light contribution of the j^{th} stellar spectrum. The weighting function W can be used to make sure certain properties of the synthetic spectrum (such as the shape of parts of the continuum) are made the most important factor in producing a good match to the observed spectrum. The only astrophysical constraint that Pickles applied when minimising the merit function was to disallow negative values of the fraction vector X.

A typical synthesis for Pickles and Visvanathan (1985) involved 48 standard stellar spectra, each with 530 wavelength points (resolution 12). With this they were able to achieve convergence after 50 – 100 iterations. I am considering higher resolution observed and synthetic spectra – so there are many more wavelength points. The standard galaxy spectra generated with PEGASE have 1221 wavelength points and are made up from a grid of 4422 stellar spectra. The spectra generated with my high resolution catalogue have 4361 wavelength points.

To perform the least-squares minimisation I used the NAG library routine E04NCF [4]. This solves linearly constrained linear least-squares problems of the form:

$$\text{minimise} \quad F(x) \quad \text{subject to} \quad l \leq \begin{Bmatrix} x \\ Cx \end{Bmatrix} \leq u \tag{4.5}$$

[4] documentation at `http://www.nag.co.uk/numeric/fl/manual/pdf/E04/e04ncf.pdf`

where C is a constraints matrix with upper and lower bounds u and l respectively. I used two constraints to stop non-physical solutions, no negative values and no values greater than 1, and also the constraint that all the fractions must sum to 1. This routine requires you to specific an initial estimate of the solution. I found that specifying a random distribution of stellar fractions worked well.

The first step is to demonstrate that this method works on the simplest case: a synthetic spectrum with no noise. For this purpose I used PEGASE to generate galaxies at several ages, using a simple SSP model with no dust. I used the entire wavelength range of the spectrum generated by PEGASE ($\lambda = 91 - 1\,600\,000$) to recover the composition. The results from doing this least squares minimisation are shown in Figures 4.16 and 4.17. Each figure shows the results for two galaxies, one young (PEGASE timestep 30 $\Longrightarrow$ 0.16 Gyr) and one old (PEGASE timestep 64 $\Longrightarrow$ 15 Gyr). The galaxies in Figure 4.17 were generated using the standard L98 input catalogue. The galaxies in Figure 4.16 were generated using my higher resolution catalogue, as described in Section 4.2. The galaxies recovered from the least squares minimisation match the original galaxies well. However, the differences between the fractional distribution of light coming from the different stars is quite different, demonstrating the fundamental problem with this technique: the difficulty of finding a *unique* solution.

Having demonstrated that some level of success is possible for an 'ideal' galaxy I then tried to extend the technique to a more realistic galaxy. There are two main issues here. Firstly, a real galaxy is not just a SSP, things such as dust and noise affect the spectrum. Secondly, in the above test I used the entire wavelength range of the spectrum generated by PEGASE to recover the composition. However an observed galaxy will have a much smaller wavelength range available. In my case I am interested in the SDSS spectra, and so the wavelength range will be approximately $3000 - 9000$. This results in about 3000 pixels, compared to 4361 pixels when using the whole range. Reducing the wavelength range used to do the least squares minimisation drastically reduced the quality of the results and demonstrated why this method is not suitable for 'real world' problems. When using a small region of the spectrum the problem is too under constrained and so it is not possible to recover the overall distribution with great accuracy. The spectrum and the recovered stellar composition are shown in Figure 4.18. This figure shows that although the recovered distribution does not reflect the real distribution in the

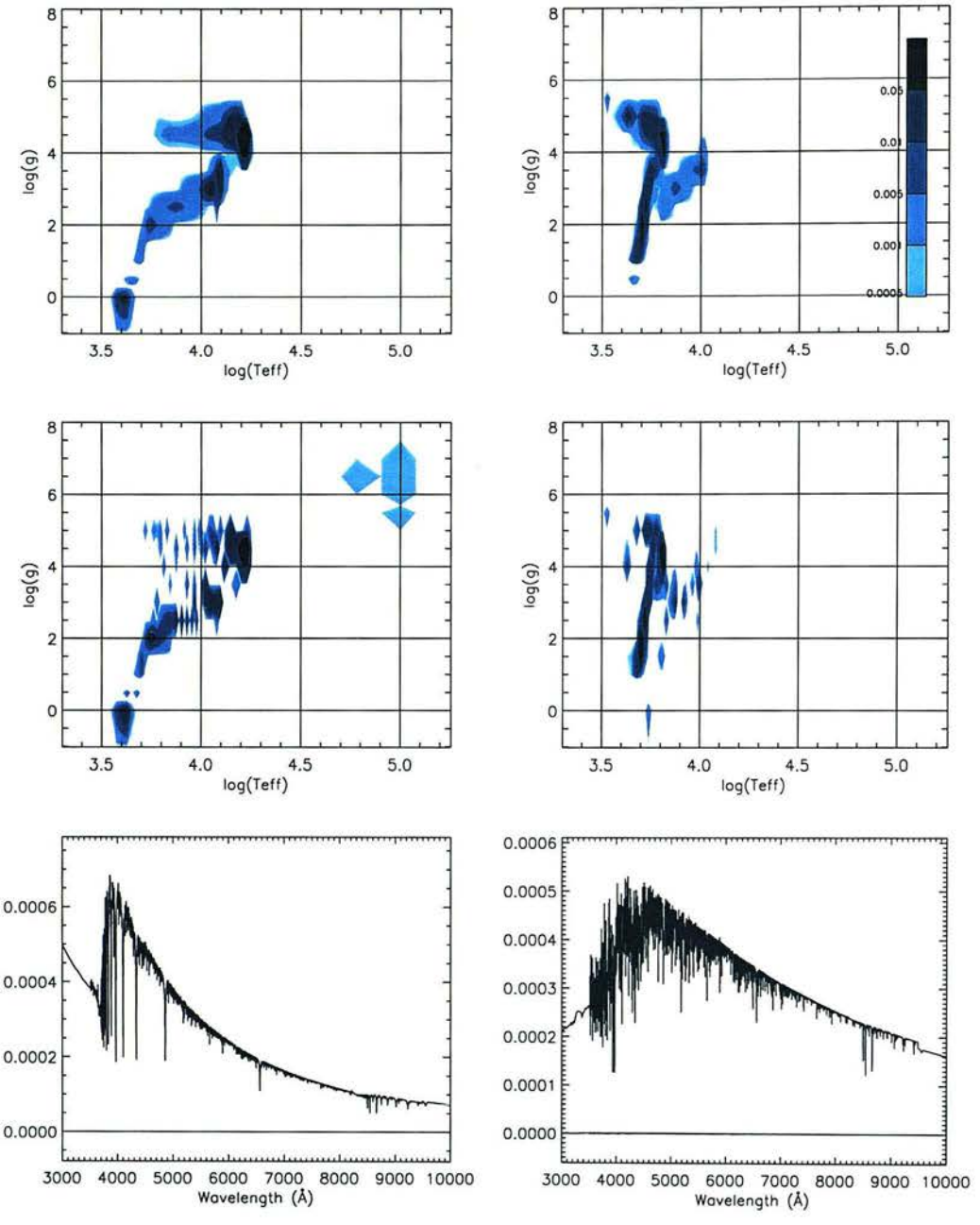

Figure 4.16: Least squares minimisation results for a galaxies aged 0.16 Gyr (left) and 15 Gyr (right), generated at 2 resolution. *Top:* the fractional content of the galaxies in $\log(T_{\rm eff})-\log(g)$ space. *Centre:* the fractional content as obtained from LSM. *Bottom:* the original galaxies overlayed with the spectra obtained from LSM and the difference spectrum. The colour bar on the top right plot applies to all the contour plots.

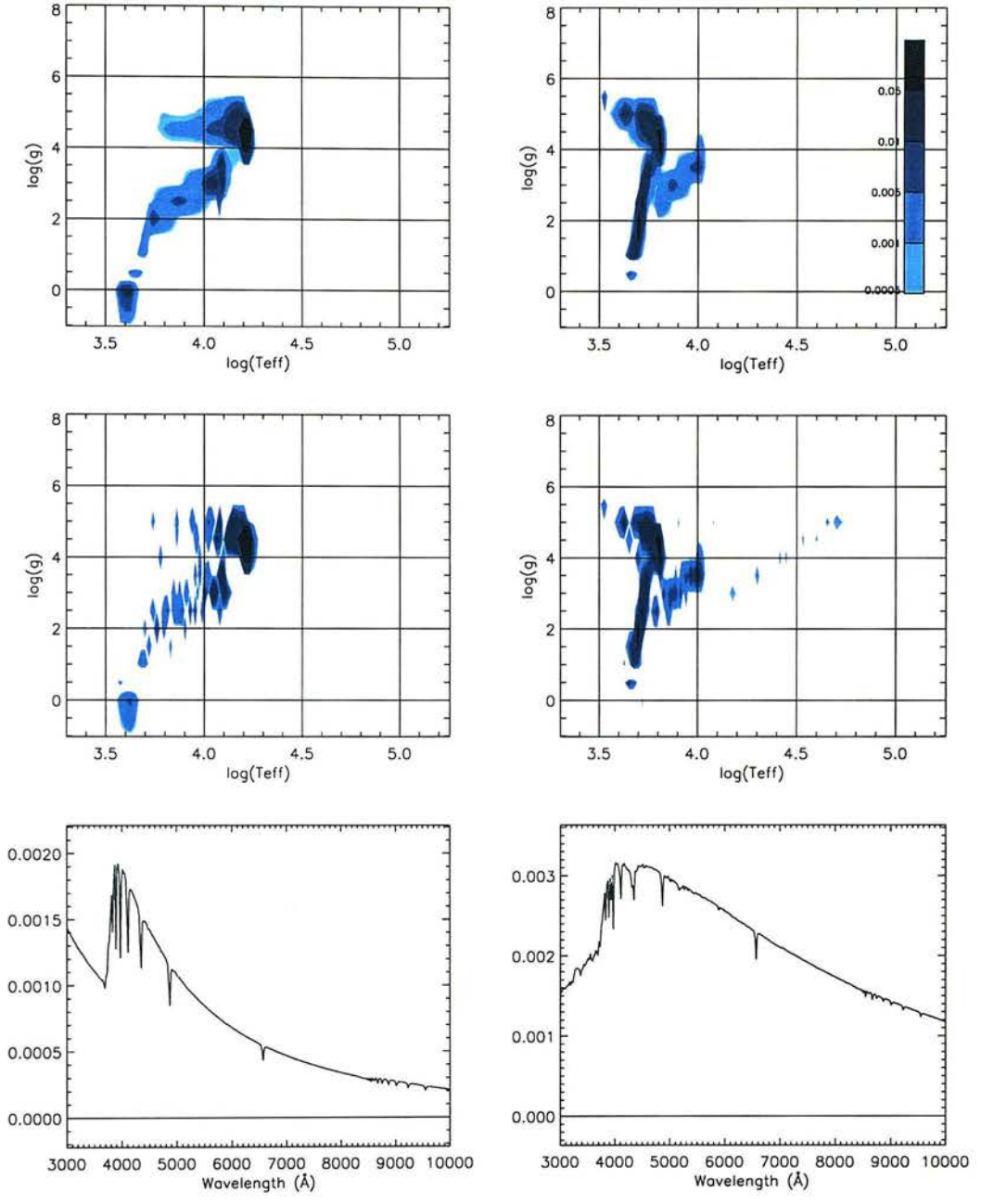

Figure 4.17: The galaxies are as in the previous figure, but generated from the standard Lejeune et al. (1998) catalogue. See the previous figure for an explanation of each plot. The colour bar on the top right plot applies to all the contour plots.

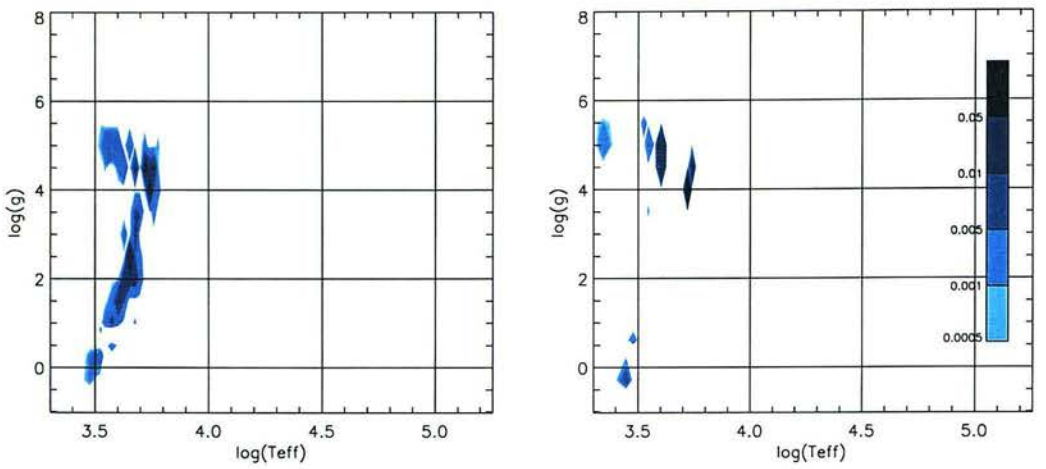

Figure 4.18: Results when only a section of the spectrum is used (3000 – 9000). The left plot is the original distribution for a 13 Gyr galaxy. The right plot shows the recovered distribution.

details, it may be possible to use this technique to discover the main features of the distribution. For example, the peak of the distribution (around $\log(T_{\rm eff}) = 3.6$, $\log(g) = 5$) shows that the majority of the light in the galaxy spectrum comes from stars of this type.

4.3.2 Direct inversion

Perhaps the most intuitive way of trying to determine the stellar content of a galaxy is simply to invert the galaxy matrix S to obtain the stellar vectors F with their relative fractions X. Here, S is the synthetic galaxy spectrum as is defined as before as:

$$S_i = \sum_{j=1}^{g} X_j \cdot F_{ij} \tag{4.6}$$

In other words it is an m by n matrix where the number of stellar spectra (m) and the number of wavelength points (n) will not typically be the same. The process of matrix inversion for a given matrix M involves finding an inverse M^{-1} such that

$$MM^{-1} = I \tag{4.7}$$

where I is the identity matrix with size the same as M. Of course, M must be a square matrix, so some rearranging is required to obtain a square matrix to apply to the galaxy matrix S.

Starting with equation 4.6 above we have

$$S = FX \implies F^*S = F^*FX \tag{4.8}$$

where F^* denotes the adjoint (inverse, transpose) of F. Introducing a square matrix $M = F^*F$ gives

$$F^*S = MX\,. \tag{4.9}$$

If the square matrix M can be inverted then

$$M^{-1}F^*S = M^{-1}MX \tag{4.10}$$

$$\implies X = M^{-1}F^*S \tag{4.11}$$

and hence the vector of fractional coefficients can be obtained. Each stellar spectrum has 4361 wavelength points, and so the matrix M is 4361×4361 pixels square. The main difficulty, then, is whether it is possible to invert this matrix. If it is possible then the inverse must be unique, since if $AB = I$ and $CA = I$ then $B = IB = (CA)B = C(AB) = CI = C$.

To do the matrix inversion I used the NAG Library routines F07ADF[5] which forms the LU factorisation of a real, m by n matrix, followed by F07AGF[6] and finally F07AJF[7] which does the actual inversion, assuming the matrix has been factorised. I first tried this with a much smaller matrix than the ones I was interested in, by creating a test 'galaxy' at 20 resolution with a wavelength range $3010-8990$. The galaxy was created by summing together 3 stellar spectra (from a subset of 300 spectra from the PEGASE input catalogue) in the proportions $1.0F_{10} + 0.5F_{26} + 0.3F_{50}$ which when normalised, corresponds to fractions of $X_{10} = 0.556, X_{26} = 0.278$ and $X_{50} = 0.167$. The original fractional contribution from each spectrum is shown in black in Figure 4.19. The fractional contribution of each of the 300 spectra obtained from inverting the matrix are shown in red (shifted slightly along the x-axis for ease of comparison). The values for the 3 spectra that contributed to the galaxy are $X_{10} = 0.560, X_{26} = 0.280$ and $X_{50} = 0.168$, which are very close to the original values. This validates the method, albeit for a very small and simple system.

[5]documentation at `http://www.nag.co.uk/numeric/fl/manual/pdf/F07/f07adf.pdf`
[6]documentation at `http://www.nag.co.uk/numeric/fl/manual/pdf/F07/f07agf.pdf`
[7]documentation at `http://www.nag.co.uk/numeric/fl/manual/pdf/F07/f07ajf.pdf`

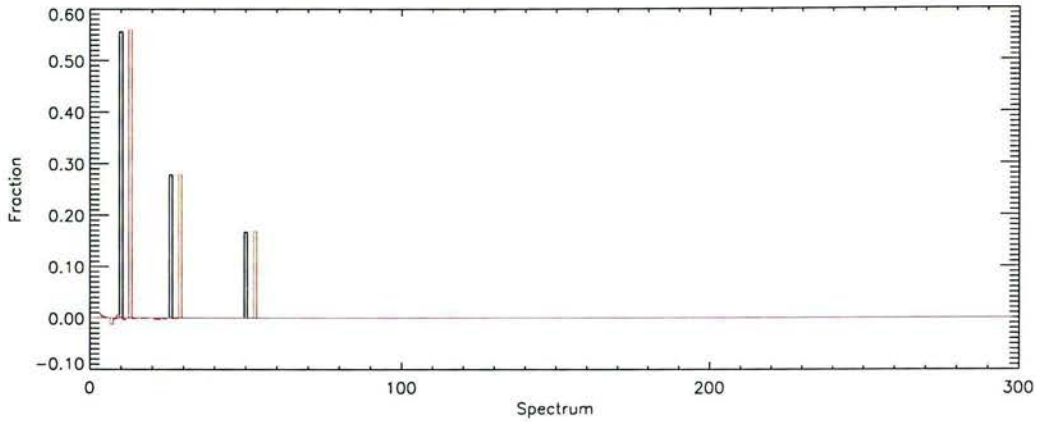

Figure 4.19: Testing direct inversion on a small (300×300) matrix. The numbers of the x-axis correspond to each of the 300 spectra in my test set. The black histogram shows the original fractional components of my test 'galaxy' spectrum. The red histogram shows the recovered components (shifted along the x-axis by several points for comparison).

When I extended the set of stellar spectra used to 400 the results were very poor, and when I extended the set further it became impossible to invert the matrix at all. Some of the computational problems could be solved by parallelising the matrix inversion, but although this would speed up the process it would not solve the problem of not being able to invert the matrix at all. I did not pursue this technique any further as it was clear that it is not practical for complicated systems. It is also very slow and so even if we were able to obtain more accurate results it would not be useful for working with large numbers of galaxies.

4.4 Evolutionary population synthesis

Evolutionary population synthesis (EPS) first appeared in the 1960's, and the work of Tinsley in the 1970's forms the basis of most of modern population synthesis (see, for example Tinsley and Gunn, 1976). EPS involves starting with some stars and evolving them into a galaxy in which the spectrum matches that of an observed galaxy. Then, since the star formation history and stellar content of the synthetic galaxy are known, these properties can be inferred for the observed galaxy.

EPS models consist of a library of stellar spectra and a set of stellar evolutionary tracks. Evolutionary tracks trace the evolution of stars of a given mass and chemical composition (see Figure 1.1). In other words they give the physical parameters of the stars ($T_{\rm eff}$, $\log(g)$, [M/H]) as a function of time. There are several standard sets of stellar tracks available, for example from the Padova (Bressan et al., 1993), Geneva (Schaller et al., 1992; Charbonnel et al., 1996) and Yale (Yi et al., 2001) groups. The accuracy of these tracks is crucial to the accuracy of the synthesised galaxies. A study by Charlot et al. (1996) showed that the main source of uncertainly in EPS is due to discrepancies in the stellar evolution tracks. A comparison of the Padova and Geneva tracks (at solar metallicity only) showed significant differences in their predictions, despite the fact that the tracks both used the same opacities, similar mixing lengths, similar helium contents and similar mass loss rates. The main cause of the differences was found to be the nature of the underlying stellar evolution models.

The basic inputs into any population synthesis system are: the Initial Mass Function (IMF) which provides the mass distribution of the original stellar population; the helium enrichment law $\Delta Y/\Delta Z$; and the amount of stellar mass-loss. Once these assumptions have been made, the process of calculating the synthesised spectrum usually involves one of two techniques, either fuel consumption theory Renzini and Buzzoni (1986) or isochrone synthesis, a technique introduced by Charlot and Bruzual (1991). Other issues that population synthesis packages deal with have less impact on the final galaxy, but are still crucial in matching observed galaxy spectra accurately. These include the nature of supernovae ejecta and stellar winds, galactic winds, the formation of substellar objects, extinction and nebular emission.

The most simple type of evolutionary population synthesis model is the *Simple Stellar Population* (SSP) which assumes all the stars are coeval (*i.e.* they formed at the same time and have evolved smoothly since that time) and have the same chemical composition. The SSP is generally a good model of globular star cluster systems. Normal galaxies are more complex than globular clusters, and are better modelled by the sum of several stellar populations of different ages. Hence they can be modelled by a sequence of instantaneous starburst models, where at certain times there is a burst of star formation that then evolves smoothly with time.

4.4.1 PEGASE

The population synthesis package that I work with throughout this thesis is PEGASE — Projet d'Étude des GAlaxies par Synthèse Évolutive — (Fioc and Rocca-Volmerange, 1997). The aim of PEGASE was to extend population synthesis into the UV region, rather than focusing solely on the optical region of the spectrum. The stellar evolutionary tracks are mainly from the Padova group (Bressan et al., 1993), supplemented with tracks from various sources to cover the AGB, post-AGB and white dwarf phases. The library of input stellar spectra is that created by Lejeune et al. (1997, 1998). PEGASE allows the user the freedom to choose from a range of standard options for each of the population synthesis assumptions:

- Initial Mass Function (*e.g.* Salpeter, Scalo, Kennicutt, ...);
- the star formation scenario (instantaneous burst, constant star formation rate, *etc.*);
- nebular emission;
- the type of supernovae ejecta;
- the nature of the stellar winds;
- the fraction of the star formation rate used to form substellar objects;
- the nature of galactic winds;
- extinction for different galaxy geometries.

I have modified PEGASE in several ways to incorporate the high resolution spectra and to provide information about the stellar content of the synthetic galaxies. I have rewritten the main spectral synthesis routine in C, factoring out all the array size dependent components so that my high resolution library can be incorporated with a flag on the command line. I have also given it the functionality to print out the fractional composition of the synthetic galaxy at any stage in its evolution, as demonstrated in Figures 4.14 and 4.15.

One of my aims in creating a new input library for PEGASE was to be able to generate a grid of higher resolution synthetic galaxy spectra for comparison with galaxy spectra observed

in the SDSS. As an example of what the higher resolution galaxy spectra are like, Figure 4.20 compares the high and low resolution spectra for galaxies at different ages. In this example I have used the simplest PEGASE model possible, an SSP with a Salpeter (1955) IMF and the default options for all other parameters (see the PEGASE `readme` file for details of these). The agreement between these spectra appears to be good, by visual inspection at least. To quantify the broadband agreement between the two sets of spectra I have plotted the *UBVRI* magnitude differences in Figure 4.21. The RMS errors for the magnitudes for the two sets of spectra are: ΔU = 0.02 mag, ΔB = 0.01 mag, ΔV = 0.00 mag, ΔR = 0.01 mag and ΔI = 0.01 mag. In the U and B magnitudes there is an offset which increase with the galaxy age. This can be explained by comparing with the magnitude offset plots for the Kurucz spectra (Figure 3.4) in Chapter 3 in which the spectra for the lowest temperature stars have the greatest offsets. Since these stars begin to dominate the light from the galaxy at the latest stages of evolution, this is where we see the greatest magnitude offsets occurring in the synthetic galaxy spectra.

4.5 Lick indices

In this section I look at another way of parameterising galaxy spectra, the Lick indices. The Lick Index system was developed using observations of stars at the Lick Observatory between 1972 and 1984 using the Cassegrain Spectrograph and Image Dissector Scanner (IDS). The entire Lick sample consists of 460 stars, 500 galaxies and 35 globular clusters, observed in the wavelength range 4000 – 6400 at a resolution of 8 – 11.5 /pix over that range.

The purpose of developing the Lick system was to have a standard, well defined way of studying the old stellar populations of galaxies and globular clusters; however, they have a much broader range of applications. The definition of each index is similar to an equivalent width, but is made more robust by measuring a pseudo-continuum based on neighbouring regions of the spectra. These regions were chosen so as to give a good representation of the spectrum continuum at the point of the particular Lick index. There were originally 11 indices (defined in Faber et al., 1985) with another 10 added later, giving 21 standard indices. In total the indices measure six molecular bands and 14 different atomic absorption lines. Full details

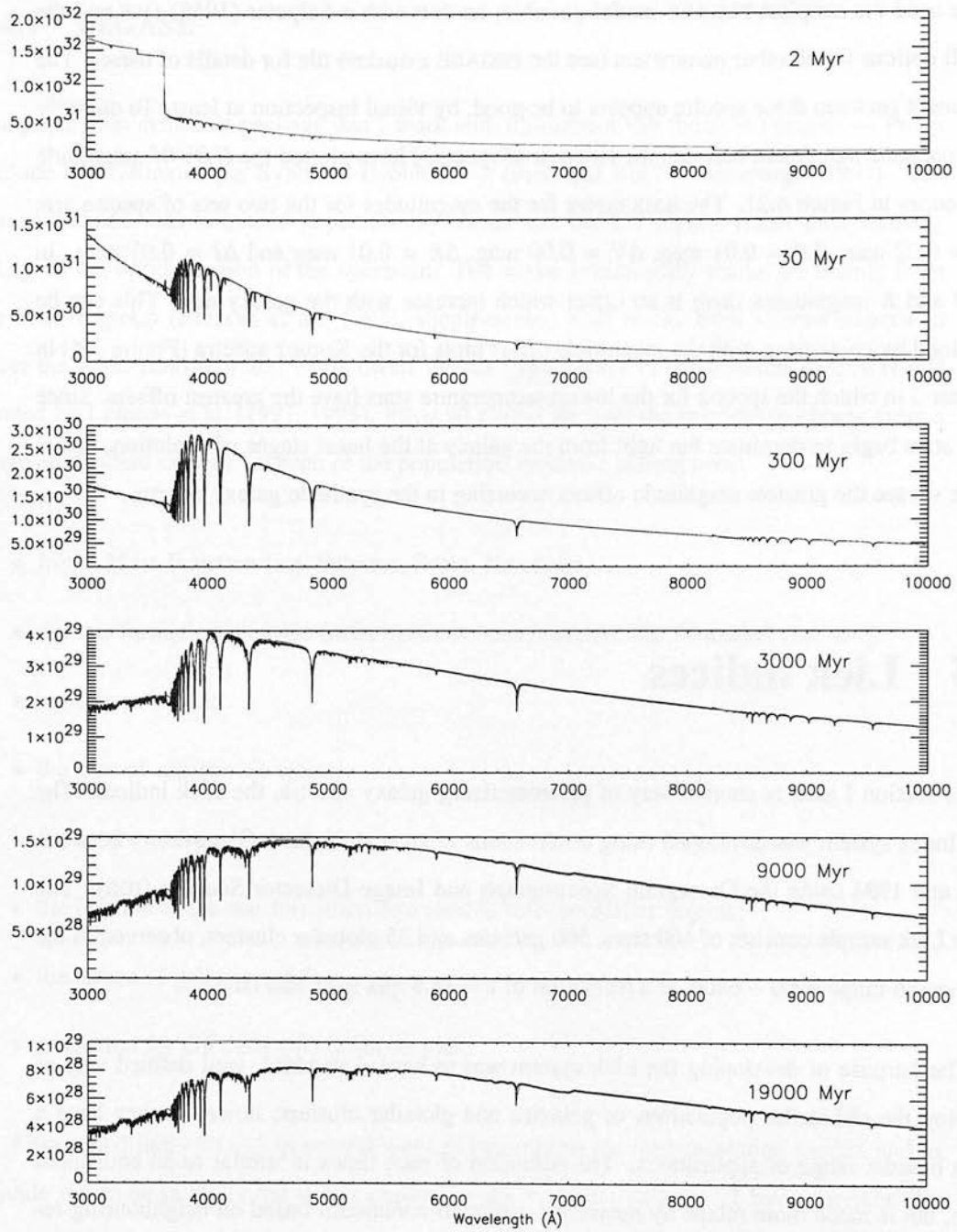

Figure 4.20: PEGASE galaxies generated with my new input library (black) overlayed with the same galaxies generated at the original 20 resolution (red). The plots show the progression of an SSP from 2 – 19 000 Myr.

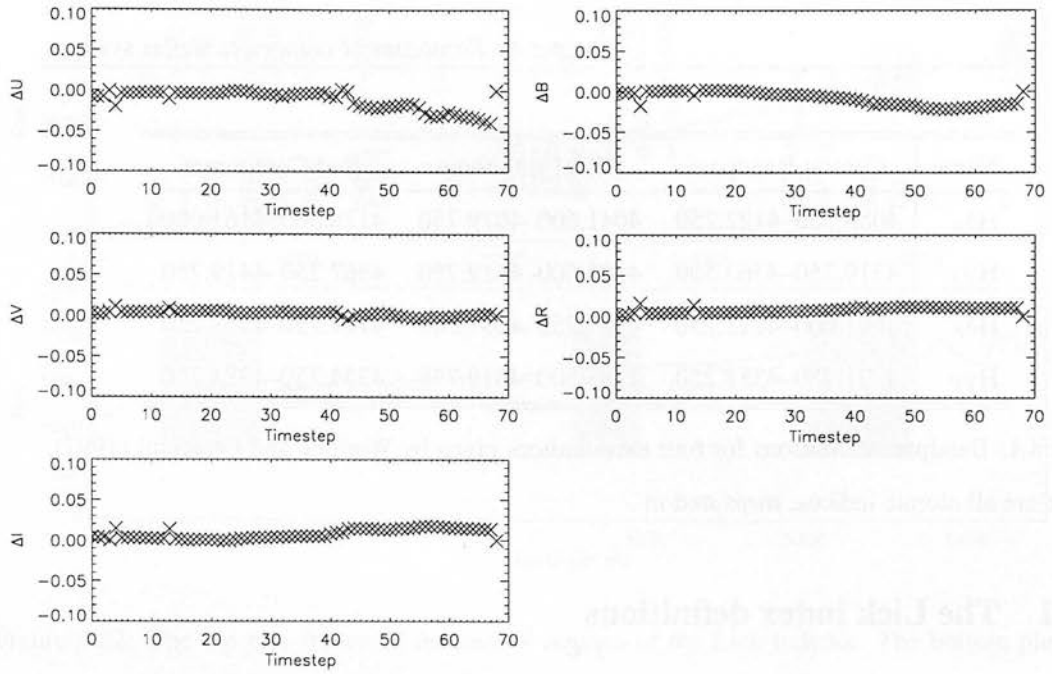

Figure 4.21: Magnitude comparisons between the galaxies generated with the original input library (20), and galaxies generated with my new input library (2).

of the development of the Lick system can be obtained from the series of papers: Burstein et al. (1984), Faber et al. (1985), Burstein et al. (1986), Gorgas et al. (1993), Worthey et al. (1994) and Trager et al. (1998). The standards are described in Worthey et al. (1994), which also summarises the previous work by the group. The latest version of the bandpass definitions is given in Trager (1997) and are available from Guy Worthey's website[8]. These are a refined version of those given in Worthey et al. (1994). Properties of the indices, in particular how they change with abundance are studied in Tripicco and Bell (1995). In the rest of the section I outline how to calculate the Lick indices, and some of the problems that arise when trying to calculate them.

[8]`http://astro.wsu.edu/worthey/html/system.html`

Name	Central Bandpass	Blue Continuum	Red Continuum
$H\delta_A$	4083.500–4122.250	4041.600–4079.750	4128.500–4161.000
$H\gamma_A$	4319.750–4363.500	4283.500–4319.750	4367.250–4419.750
$H\delta_F$	4091.000–4112.250	4057.250–4088.500	4114.750–4137.250
$H\gamma_F$	4331.250–4352.250	4283.500–4319.750	4354.750–4384.750

Table 4.1: Bandpass definitions for four extra indices given by Worthey and Ottaviani (1997). These are all atomic indices, measured in .

4.5.1 The Lick index definitions

The standard definitions of the atomic and molecular Lick indices are given by

$$I_a \equiv \int_{\lambda_{c1}}^{\lambda_{c2}} \left[1 - \frac{S(\lambda)}{C(\lambda)}\right] d\lambda \tag{4.12}$$

$$I_m \equiv -2.5 \log_{10} \frac{\int_{\lambda_{c1}}^{\lambda_{c2}} \frac{S(\lambda)}{C(\lambda)} d\lambda}{\lambda_{c2} - \lambda_{c1}} \tag{4.13}$$

where λ_{c1} and λ_{c2} are the limits of the central bandpass in , $S(\lambda)$ is the object spectrum and $C(\lambda)$ is the linearly interpolated pseudo-continuum. $C(\lambda)$ is defined by

$$C(\lambda) \equiv S_b \frac{\lambda_r - \lambda}{\lambda_r - \lambda_b} + S_r \frac{\lambda - \lambda_b}{\lambda_r - \lambda_b} \tag{4.14}$$

where

$$S_b \equiv \frac{\int_{\lambda_{b1}}^{\lambda_{b2}} S(\lambda) d\lambda}{\lambda_{b2} - \lambda_{b1}}, \quad \lambda_b \equiv (\lambda_{b1} + \lambda_{b2})/2 \tag{4.15}$$

$$S_r \equiv \frac{\int_{\lambda_{r1}}^{\lambda_{r2}} S(\lambda) d\lambda}{\lambda_{r2} - \lambda_{r1}}, \quad \lambda_r \equiv (\lambda_{r1} + \lambda_{r2})/2 \tag{4.16}$$

and λ_{b1}, λ_{b2}, λ_{r1} and λ_{r2} are the limits of the blue and red continuum bands. The regions defined by these equations are illustrated in the right hand panel of Figure 4.22. In addition to the indices defined in Table 3.2, in this section I calculate four extra indices as defined by Worthey and Ottaviani (1997). The bandpasses for these indices are given in Table 4.1.

If you wish to use any of the actual Lick index results or relationships measured by the Lick group it is necessary to transform your spectra to the Lick system before making a measurement. Ideally, repeat observations of some of the Lick standard stars can be used to calibrate

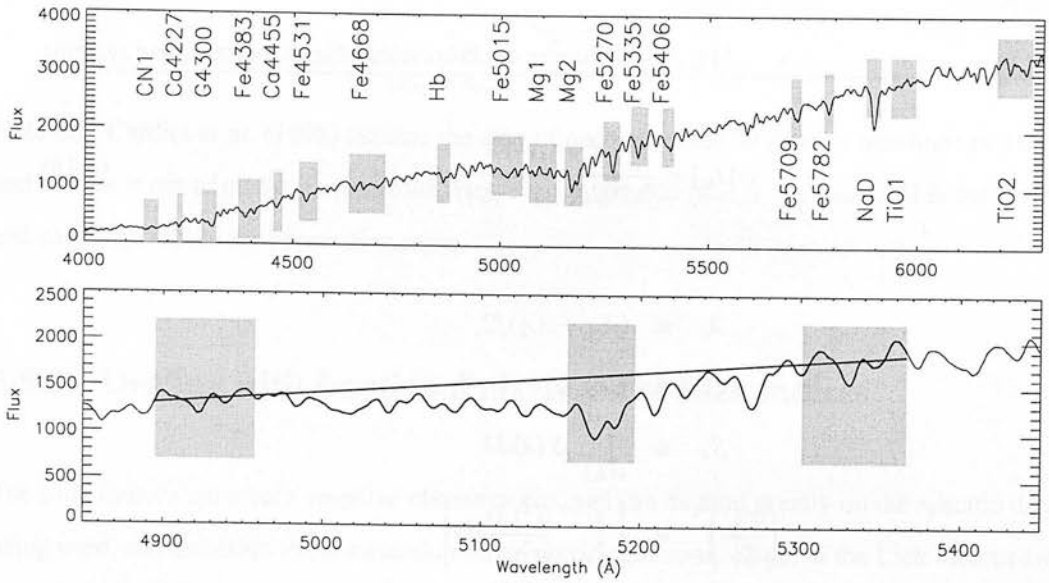

Figure 4.22: The top plot shows all the central regions of the Lick indices. The bottom plot gives an example of the regions defined in Equations 4.12 to 4.16, for Mg_2. The shaded regions represent the blue ($\lambda_{b1} - \lambda_{b2}$), central ($\lambda_{c1} - \lambda_{c2}$) and red ($\lambda_{r1} - \lambda_{r2}$) bandpasses. The straight line in the pseudo-continuum $C(\lambda)$.

your data against the Lick data. However, if this is not possible there are various other ways that some approximate calibration can be made. These issues are discussed in the Appendix of Worthey and Ottaviani (1997). In this work I am mainly concerned with measuring Lick indices for the SDSS galaxies. The SDSS pipeline measurements of the Lick indices do not transform to the Lick system and hence I will not be doing any kind of transformation with my data.

4.5.2 Calculating errors on the Lick indices

Given an estimate for the error on each pixel in the spectrum, $\sigma(\lambda)$, it is possible to calculate the random error on a Lick index using the analytic expressions derived by González (1993)

$$\sigma[I_a] = \frac{S_c}{C_c}\sqrt{\left(\frac{\sigma_{S_c}}{S_c}\right)^2 + \frac{\sigma_{S_b}^2}{C_c^2}\left(\frac{\lambda_r - \lambda_c}{\lambda_r - \lambda_b}\right)^2 + \frac{\sigma_{S_r}^2}{C_c^2}\left(\frac{\lambda_b - \lambda_c}{\lambda_r - \lambda_b}\right)^2} \tag{4.17}$$

$$\sigma[I_m] = \frac{2.5 \times 10^{0.4 I_m}}{2.3026(\lambda_{c2} - \lambda_{c1})} \sigma[I_a] \tag{4.18}$$

where

$$\begin{aligned}
\lambda_c &\equiv (\lambda_{c1} + \lambda_{c2})/2 \\
C_c &\equiv C(\lambda_c) \\
S_c &\equiv \int_{\lambda_{c1}}^{\lambda_{c2}} S(\lambda) d\lambda \\
\left(\frac{\sigma_{S_c}}{S_c}\right)^2 &\equiv \left[\int_{\lambda_{c1}}^{\lambda_{c2}} \frac{S^2(\lambda)}{\sigma^2(\lambda)} d\lambda\right]^{-1} \\
\sigma_{Sb}^2 &\equiv S_b^2 \left[\int_{\lambda_{b1}}^{\lambda_{b2}} \frac{S^2(\lambda)}{\sigma^2(\lambda)} d\lambda\right]^{-1} \\
\sigma_{Sr}^2 &\equiv S_r^2 \left[\int_{\lambda_{r1}}^{\lambda_{r2}} \frac{S^2(\lambda)}{\sigma^2(\lambda)} d\lambda\right]^{-1} .
\end{aligned}$$

Cardiel et al. (1998) derive a more accurate pair of equations for calculating the errors, based on a full analysis of the error propagation throughout the calculation process. These are given by

$$\sigma^2[I_a] = \sum_{i=1}^{N_{\text{pixels}}} \left[\frac{C^2(\lambda_i)\sigma^2(\lambda_i) + S^2(\lambda_i)\sigma^2_{C(\lambda_i)}}{C^4(\lambda_i)}\right] d\lambda_i^2 + \sum_{i=1}^{N_{\text{pixels}}} \sum_{j=1, j\neq i}^{N_{\text{pixels}}} \left[\frac{S(\lambda_i)S(\lambda_j)}{C^2(\lambda_i)C^2(\lambda_j)} (\Lambda_1 \sigma^2_{S_b} + \Lambda_4 \sigma^2_{S_r})\right] d\lambda_i d\lambda_j \tag{4.19}$$

for the atomic indices and

$$\sigma[I_m] = 2.5 \frac{\log(e)}{10^{-0.4 I_m}} \frac{1}{\lambda_{c_2} - \lambda_{c_1}} \sigma[I_a] \tag{4.20}$$

for the molecular indices, where

$$\Lambda_1 \equiv \frac{(\lambda_r - \lambda_i)(\lambda_r - \lambda_j)}{(\lambda_r - \lambda_b)^2} \tag{4.21}$$

$$\Lambda_4 \equiv \frac{(\lambda_i - \lambda_b)(\lambda_j - \lambda_b)}{(\lambda_r - \lambda_b)^2} \tag{4.22}$$

$$\sigma^2_{C(\lambda_i)} = \left(\frac{\lambda_r - \lambda_i}{\lambda_r - \lambda_b}\right) \sigma^2_{S_b} + \left(\frac{\lambda_i - \lambda_b}{\lambda_r - \lambda_b}\right) \sigma^2_{S_r} \tag{4.23}$$

$$\sigma^2_{S_b} = \frac{1}{(\lambda_{b_2} - \lambda_{b_1})^2} \sum_{i=1}^{N_{\text{pixels(blue)}}} \sigma^2(\lambda_i)\, d\lambda_i^2 \tag{4.24}$$

$$\sigma^2_{S_r} = \frac{1}{(\lambda_{r_2} - \lambda_{r_1})^2} \sum_{i=1}^{N_{\text{pixels(red)}}} \sigma^2(\lambda_i)\, d\lambda_i^2 \,. \tag{4.25}$$

Note that Cardiel et al. (1998) assume the size of each pixel $d\lambda$ (Θ in their notation) is fixed, and so take it out of all the summations. However, in general (and in my case), $d\lambda$ is not fixed, and so is kept inside the summation signs.

4.5.3 Dealing with fractional pixels in the Lick indices

The Lick indices are a very sensitive measurement, and can depend greatly on the specific data being used, and the exact implementation of the above equations. Some of the Lick indices are calculated over a relatively small wavelength range and hence, depending on the resolution of the spectra, over a small number of pixels. When the edge of the bandpass does not fall exactly on the edge of a pixel in the spectrum, you have to deal with a fractional pixel at each end of the band. A band such as Ca4227, for instance, has a central bandpass 4222.25 – 4234.75 , which is only ~ 6 pixels at 2 sampling. In this section I investigate whether the way in which you deal with fractional pixels has a significant effect on the value of the Lick index.

The most basic way of dealing with the pixel at λ_1 with width $\Delta\lambda$ and value $y(\lambda)$ is to view the pixel as a rectangular block, with height $y(\lambda)$, centred on position λ. The block is cut at some point λ_{min} (the edge of the bandpass). Then the fractional area of the pixel is

$$A = y(\lambda)\left(\lambda_1 + \frac{\Delta\lambda}{2} - \lambda_{min}\right) \,. \tag{4.26}$$

This is illustrated in Figure 4.23. A more accurate version is to take the value of the pixel to be the average of that pixel and the neighbouring pixel, so the fractional area of the pixel is

$$A = \frac{1}{2}\left[y(\lambda_1) + y(\lambda_2)\right]\left(\lambda_1 + \frac{\Delta\lambda}{2} - \lambda_{min}\right) \,. \tag{4.27}$$

This is illustrated in Figure 4.24. The most accurate way is to calculate the exact area under each pixel, using the trapezoidal rule

$$A = \frac{1}{2}\left[y(\lambda_{min}) + y(\lambda_1 + \frac{\Delta\lambda}{2})\right]\left(\lambda_1 + \frac{\Delta\lambda}{2} - \lambda_{min}\right) \,. \tag{4.28}$$

This is illustrated in Figure 4.25.

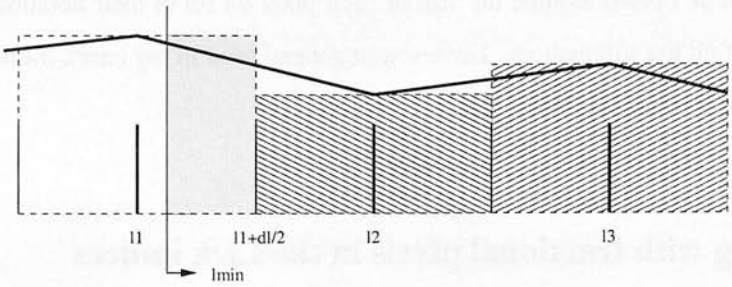

Figure 4.23: An illustration of the most straightforward way of dealing with fractional pixels. The dark vertical lines show the centre of each pixel ($\lambda_1, \lambda_2 \ldots$). The thinner lines show the edges of each pixel ($\lambda_1 + \Delta\lambda/2$). The heavy solid line connects the measured value assigned to each pixel's central wavelength. Each pixel is treated as a block with height $y(\lambda)$. The grey shaded area shows the fractional area of the pixel that will be counted toward the calculation of the Lick index.

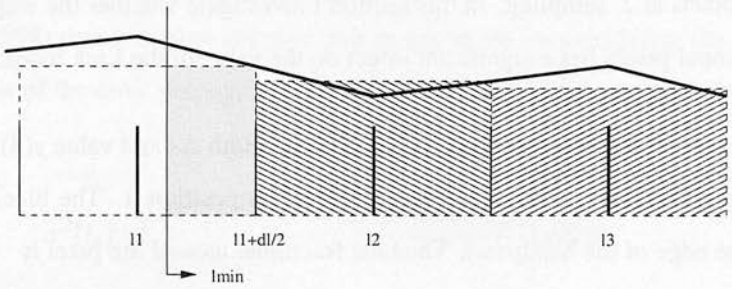

Figure 4.24: An improved version of Figure 4.23, where the height of each pixel is taken to be the average of it and the neighbouring pixel. All notation is the same as in Figure 4.23.

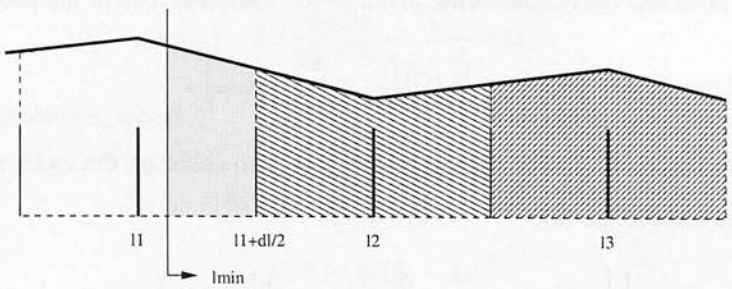

Figure 4.25: The exact area of each pixel is calculated. All notation is the same as in Figure 4.23.

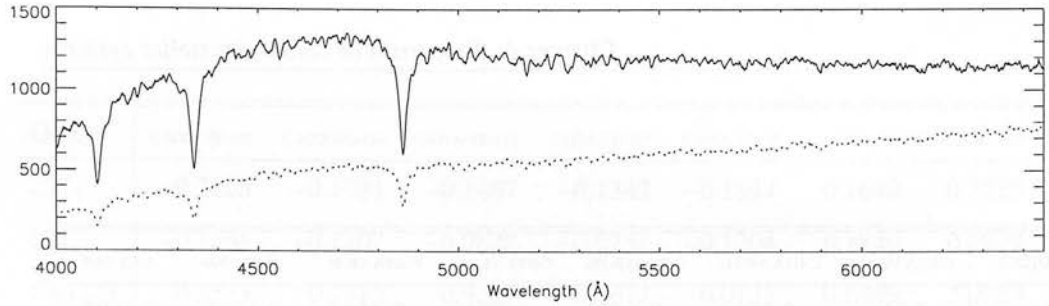

Figure 4.26: Two spectra from the Worthey test set, C HYA VB 112 (solid line) and C HYA VB 111 (dotted line). The flux is in arbitrary units.

Guy Worthey provides a test set of spectra on his website [9] that can be used to confirm you are calculating the Lick indices correctly. Two examples of these spectra are shown in Figure 4.26. I calculated the Lick indices for each spectrum, experimenting with each of the methods of dealing with fractional pixels described above. Worthey's calculated values for each of the test spectra are shown in Table 4.2. My results are shown in the next three tables, specifically the block method in Table 4.3, average neighbouring pixels in Table 4.4, calculating exact area of fractional pixel in Table 4.5. The maximum differences between the different methods, for each index, are shown in Table 4.6. The random error on each index, as calculated by Equations 4.17 and 4.18 is shown in Table 4.7. The maximum difference between the different methods is of the same order of magnitude as the random error in many cases, which suggests the method of dealing with fractional pixels is not insignificant. However, both these differences, and the random error measurements, are likely to be significantly smaller than differences caused by systematics, such as the calibration of the spectra, so it is not clear if they will have much effect overall. I decided to calculate the exact area of the fractional pixels, as the computational expense was not significant with respect to the overall calculation.

[9] `http://astro.wsu.edu/worthey/`.

Object	C-HYA-VB-112	C-HYA-VB-111	C-HYA-VB-103	C-HYA-VB-103	C-HYA-VB-95	S-HR-6770	S-HR-7429
CN_1	–0.2166	–0.1784	–0.1474	–0.1345	–0.1845	0.1647	0.2582
CN_2	–0.1537	–0.1208	–0.0837	–0.0759	–0.1206	0.1835	0.2968
Ca4227	0.3867	0.7314	0.3261	0.2656	0.0179	0.6470	2.0157
G4300	–1.7058	–0.6097	–1.3522	–0.2306	–0.4444	6.2573	6.3599
Fe4383	–1.3612	–0.9046	–0.5561	0.3196	–1.0735	5.2520	7.9968
Ca4455	0.0937	–0.0860	0.0376	0.0277	0.0251	1.3567	2.1084
Fe4531	1.4019	2.0045	1.7000	2.1937	1.5324	3.2418	4.4061
Fe4668	–0.2301	–0.6610	1.1941	1.1886	0.1803	5.4036	7.6690
$H\beta$	7.9793	6.7960	6.9482	6.6314	7.3878	1.6559	0.8861
Fe5015	2.2638	2.7791	2.1369	1.9241	3.1356	6.0680	5.8463
Mg_1	0.0052	0.0003	0.0280	0.0207	–0.0144	0.0521	0.2033
Mg_2	0.0368	0.0294	0.0264	0.0298	0.0181	0.1490	0.3599
Mg b	0.4981	0.6761	0.2494	0.4357	0.4532	2.4936	4.8288
Fe5270	0.9764	1.2326	2.3431	1.3770	0.3502	3.4392	3.6879
Fe5335	0.7577	0.5729	–0.1757	0.3774	0.2472	2.5624	3.5034
Fe5406	0.6434	0.3363	0.1579	0.0742	0.6556	1.8760	2.3421
Fe5709	0.4204	0.2493	0.4228	0.0395	0.1280	0.9422	1.5064
Fe5782	0.5728	0.3266	0.7415	0.7070	0.2567	0.9314	1.0773
Na D	0.7528	0.8871	0.5196	0.6259	1.0093	1.9685	3.5152
TiO_1	0.0113	0.0152	0.0344	0.0173	0.0074	0.0303	0.0220
TiO_2	0.0004	–0.0060	0.0165	0.0001	0.0011	0.0139	0.0285
$H\delta_A$	10.7413	9.2458	6.8251	6.8466	10.3301	–4.5433	–6.4895
$H\gamma_A$	11.5886	9.3231	8.2097	7.1806	9.1983	–6.8469	–9.3953
$H\delta_F$	7.0310	6.0016	5.6658	5.0730	6.3271	–0.8108	–1.2308
$H\gamma_F$	8.2073	6.9467	5.9631	5.6617	6.7501	–1.8909	–3.0677

Table 4.2: Worthey's calculated values for the Lick indices for each of the 7 test galaxies.

Object	C-HYA-VB-112	C-HYA-VB-111	C-HYA-VB-103	C-HYA-VB-103	C-HYA-VB-95	S-HR-6770	S-HR-7429
CN_1	–0.2165	–0.1784	–0.1467	–0.1342	–0.1844	0.1648	0.2585
CN_2	–0.1535	–0.1207	–0.0828	–0.0754	–0.1204	0.1840	0.2979
Ca4227	0.3875	0.7313	0.3293	0.2672	0.0171	0.6499	2.0223
G4300	–1.7018	–0.6069	–1.3480	–0.2207	–0.4393	6.2671	6.3711
Fe4383	–1.3527	–0.8894	–0.5752	0.3159	–1.0867	5.2969	7.9977
Ca4455	0.0937	–0.0800	0.0196	0.0257	0.0125	1.3597	2.1083
Fe4531	1.4102	1.9996	1.7602	2.2407	1.5474	3.2553	4.4120
Fe4668	–0.2231	–0.6432	1.1982	1.1893	0.1930	5.4209	7.7337
$H\beta$	7.9976	6.8148	6.9642	6.6466	7.3931	1.6598	0.8898
Fe5015	2.2721	2.7921	2.1355	1.9391	3.1441	6.1209	5.9026
Mg_1	0.0052	0.0003	0.0279	0.0207	–0.0144	0.0521	0.2034
Mg_2	0.0370	0.0294	0.0263	0.0297	0.0182	0.1491	0.3598
Mg b	0.4974	0.6764	0.2476	0.4364	0.4535	2.5017	4.8567
Fe5270	0.9814	1.2395	2.3620	1.3766	0.3469	3.4455	3.6910
Fe5335	0.7544	0.5661	–0.1976	0.3695	0.2542	2.5650	3.5035
Fe5406	0.6434	0.3363	0.1579	0.0742	0.6556	1.8817	2.3644
Fe5709	0.4171	0.2496	0.4111	0.0275	0.1175	0.9478	1.5097
Fe5782	0.5754	0.3334	0.7530	0.7209	0.2607	0.9371	1.0786
Na D	0.7508	0.8970	0.5226	0.6269	1.0162	1.9718	3.5157
TiO_1	0.0112	0.0151	0.0344	0.0173	0.0074	0.0303	0.0220
TiO_2	0.0004	–0.0060	0.0165	0.0002	0.0010	0.0139	0.0286
$H\delta_A$	10.7591	9.3123	7.0262	6.8772	10.3463	–4.7181	–6.7715
$H\gamma_A$	11.6977	9.4317	8.3551	7.3415	9.3696	–6.9022	–9.5006
$H\delta_F$	6.9790	5.9312	5.5918	5.0222	6.2324	–0.8828	–1.4190
$H\gamma_F$	8.2395	7.0210	6.0473	5.7719	6.8340	–1.8542	–3.0155

Table 4.3: My values for the Lick indices, calculated using the method shown in Figure 4.23.

Object	C-HYA-VB-112	C-HYA-VB-111	C-HYA-VB-103	C-HYA-VB-103	C-HYA-VB-95	S-HR-6770	S-HR-7429
CN_1	–0.2165	–0.1785	–0.1481	–0.1347	–0.1844	0.1641	0.2574
CN_2	–0.1544	–0.1217	–0.0854	–0.0771	–0.1212	0.1827	0.2956
Ca4227	0.3831	0.7271	0.3310	0.2687	0.0273	0.6342	1.9835
G4300	–1.7219	–0.6249	–1.3657	–0.2627	–0.4618	6.2438	6.3536
Fe4383	–1.3710	–0.9284	–0.5578	0.3232	–1.0715	5.2230	7.9627
Ca4455	0.0902	–0.0865	0.0636	0.0332	0.0261	1.3234	2.0767
Fe4531	1.3942	1.9972	1.6751	2.1712	1.5256	3.2292	4.3816
Fe4668	–0.2360	–0.6815	1.1862	1.1796	0.1662	5.3849	7.6552
$H\beta$	7.9602	6.7796	6.9296	6.6138	7.3744	1.6542	0.8892
Fe5015	2.2491	2.7590	2.1185	1.9012	3.1144	6.0220	5.8220
Mg_1	0.0051	0.0002	0.0281	0.0207	–0.0144	0.0520	0.2031
Mg_2	0.0367	0.0293	0.0264	0.0298	0.0180	0.1489	0.3597
Mg b	0.5009	0.6737	0.2589	0.4346	0.4507	2.4776	4.8117
Fe5270	0.9715	1.2287	2.3336	1.3721	0.3497	3.4236	3.6645
Fe5335	0.7509	0.5751	–0.1564	0.3801	0.2389	2.5257	3.4536
Fe5406	0.6287	0.3328	0.1553	0.0794	0.6412	1.8546	2.3167
Fe5709	0.4232	0.2501	0.4291	0.0472	0.1317	0.9396	1.5004
Fe5782	0.5677	0.3212	0.7308	0.6927	0.2531	0.9277	1.0736
Na D	0.7552	0.8839	0.5153	0.6234	1.0079	1.9624	3.5095
TiO_1	0.0113	0.0153	0.0343	0.0172	0.0075	0.0303	0.0219
TiO_2	0.0003	–0.0061	0.0165	0.0000	0.0011	0.0139	0.0284
$H\delta_A$	10.7477	9.3051	7.0219	6.8860	10.3477	–4.6887	–6.7384
$H\gamma_A$	11.6920	9.4361	8.3532	7.3355	9.3661	–6.9089	–9.5079
$H\delta_F$	6.9590	5.9147	5.5560	4.9907	6.2259	–0.8905	–1.4356
$H\gamma_F$	8.2199	6.9988	6.0287	5.7579	6.8175	–1.8453	–2.9991

Table 4.4: My values for the Lick indices, calculated using the method shown in Figure 4.24.

Object	C-HYA-VB-112	C-HYA-VB-111	C-HYA-VB-103	C-HYA-VB-103	C-HYA-VB-95	S-HR-6770	S-HR-7429
CN_1	–0.2189	–0.1808	–0.1497	–0.1366	–0.1866	0.1630	0.2562
CN_2	–0.1560	–0.1231	–0.0861	–0.0780	–0.1226	0.1819	0.2948
Ca4227	0.3815	0.7254	0.3212	0.2589	0.0244	0.6161	1.9602
G4300	–1.6206	–0.5474	–1.2871	–0.1849	–0.3748	6.1780	6.2337
Fe4383	–1.4228	–0.9768	–0.6074	0.2857	–1.1359	5.1880	7.9150
Ca4455	0.0909	–0.0905	0.0492	0.0221	0.0114	1.3062	2.0511
Fe4531	1.3977	1.9846	1.6888	2.1732	1.5267	3.2287	4.3807
Fe4668	–0.2370	–0.6892	1.1657	1.1652	0.1415	5.3561	7.6204
$H\beta$	7.9838	6.7913	6.9333	6.6257	7.3784	1.6617	0.8982
Fe5015	2.2601	2.7615	2.1070	1.9063	3.1067	6.0240	5.8263
Mg_1	0.0052	0.0001	0.0279	0.0205	–0.0147	0.0516	0.2026
Mg_2	0.0368	0.0292	0.0262	0.0296	0.0178	0.1486	0.3593
Mg b	0.5123	0.6828	0.2631	0.4429	0.4594	2.4794	4.7757
Fe5270	0.9707	1.2192	2.3405	1.3683	0.3396	3.4035	3.6410
Fe5335	0.7466	0.5635	–0.1897	0.3549	0.2183	2.5194	3.4500
Fe5406	0.6439	0.3452	0.1426	0.0711	0.6457	1.8667	2.3172
Fe5709	0.4221	0.2387	0.4172	0.0340	0.1274	0.9252	1.4907
Fe5782	0.5746	0.3202	0.7330	0.7043	0.2548	0.9176	1.0625
Na D	0.7586	0.8839	0.5135	0.6149	1.0104	1.9588	3.5098
TiO_1	0.0114	0.0152	0.0342	0.0171	0.0073	0.0301	0.0216
TiO_2	0.0004	–0.0063	0.0163	–0.0001	0.0009	0.0134	0.0281
$H\delta_A$	10.7207	9.2683	6.9823	6.8447	10.3299	–4.7500	–6.7914
$H\gamma_A$	11.6714	9.3967	8.3115	7.2973	9.3286	–7.0328	–9.6510
$H\delta_F$	6.9591	5.9034	5.5430	4.9824	6.2236	–0.9175	–1.4571
$H\gamma_F$	8.2256	6.9990	6.0196	5.7468	6.8130	–1.9204	–3.0896

Table 4.5: My values for the Lick indices, calculated using the method shown in Figure 4.25.

Object	C-HYA-VB-112	C-HYA-VB-111	C-HYA-VB-103	C-HYA-VB-103	C-HYA-VB-95	S-HR-6770	S-HR-7429
CN_1	0.0024	0.0024	0.0030	0.0024	0.0022	0.0018	0.0023
CN_2	0.0025	0.0024	0.0033	0.0026	0.0022	0.0021	0.0031
Ca4227	0.0060	0.0060	0.0098	0.0098	0.0102	0.0338	0.0621
G4300	0.1013	0.0775	0.0786	0.0778	0.0870	0.0891	0.1374
Fe4383	0.0701	0.0874	0.0513	0.0375	0.0644	0.1089	0.0827
Ca4455	0.0035	0.0105	0.0440	0.0111	0.0147	0.0535	0.0573
Fe4531	0.0160	0.0199	0.0851	0.0695	0.0218	0.0266	0.0313
Fe4668	0.0139	0.0460	0.0325	0.0241	0.0515	0.0648	0.1133
$H\beta$	0.0374	0.0352	0.0346	0.0328	0.0187	0.0075	0.0121
Fe5015	0.0230	0.0331	0.0299	0.0379	0.0374	0.0989	0.0806
Mg_1	0.0001	0.0002	0.0002	0.0002	0.0003	0.0005	0.0008
Mg_2	0.0003	0.0002	0.0002	0.0002	0.0004	0.0005	0.0006
Mg b	0.0149	0.0091	0.0155	0.0083	0.0087	0.0241	0.0810
Fe5270	0.0107	0.0203	0.0284	0.0087	0.0106	0.0420	0.0500
Fe5335	0.0111	0.0116	0.0412	0.0252	0.0359	0.0456	0.0535
Fe5406	0.0152	0.0124	0.0153	0.0083	0.0144	0.0271	0.0477
Fe5709	0.0061	0.0114	0.0180	0.0197	0.0142	0.0226	0.0190
Fe5782	0.0077	0.0132	0.0222	0.0282	0.0076	0.0195	0.0161
Na D	0.0078	0.0131	0.0091	0.0120	0.0083	0.0130	0.0062
TiO_1	0.0002	0.0002	0.0002	0.0002	0.0002	0.0002	0.0004
TiO_2	0.0001	0.0003	0.0002	0.0003	0.0002	0.0005	0.0005
$H\delta_A$	0.0384	0.0665	0.2011	0.0413	0.0178	0.2067	0.3019
$H\gamma_A$	0.1091	0.1130	0.1454	0.1609	0.1713	0.1859	0.2557
$H\delta_F$	0.0720	0.0982	0.1228	0.0906	0.1035	0.1067	0.2263
$H\gamma_F$	0.0322	0.0743	0.0842	0.1102	0.0839	0.0751	0.0905

Table 4.6: The maximum difference in the results obtained between the three methods of dealing with fractional pixels.

Object	C-HYA-VB-112	C-HYA-VB-111	C-HYA-VB-103	C-HYA-VB-103	C-HYA-VB-95	S-HR-6770	S-HR-7429
CN_1	0.0010	0.0012	0.0031	0.0025	0.0015	0.0014	0.0019
CN_2	0.0013	0.0015	0.0044	0.0029	0.0024	0.0020	0.0032
Ca4227	0.0112	0.0159	0.0377	0.0267	0.0260	0.0367	0.1003
G4300	0.0507	0.0596	0.0792	0.0665	0.0534	0.0729	0.0968
Fe4383	0.0456	0.0677	0.1089	0.0823	0.0738	0.0818	0.1013
Ca4455	0.0151	0.0234	0.0344	0.0385	0.0274	0.0689	0.0727
Fe4531	0.0283	0.0478	0.0831	0.0422	0.0320	0.0464	0.0555
Fe4668	0.0384	0.0405	0.0887	0.0501	0.0533	0.0509	0.0592
$H\beta$	0.1144	0.1067	0.1003	0.0965	0.1113	0.0371	0.0337
Fe5015	0.0486	0.0504	0.0879	0.0767	0.0570	0.1091	0.1050
Mg_1	0.0004	0.0004	0.0007	0.0006	0.0006	0.0009	0.0008
Mg_2	0.0006	0.0006	0.0008	0.0007	0.0006	0.0016	0.0026
Mg b	0.0253	0.0261	0.0390	0.0289	0.0256	0.0569	0.0973
Fe5270	0.0182	0.0199	0.0530	0.0285	0.0223	0.0571	0.0625
Fe5335	0.0301	0.0199	0.0389	0.0353	0.0296	0.0534	0.0586
Fe5406	0.0196	0.0182	0.0518	0.0366	0.0200	0.0163	0.0285
Fe5709	0.0216	0.0184	0.0483	0.0345	0.0139	0.0279	0.0236
Fe5782	0.0140	0.0166	0.0277	0.0213	0.0197	0.0234	0.0323
Na D	0.0180	0.0149	0.0278	0.0296	0.0236	0.0326	0.0520
TiO_1	0.0004	0.0005	0.0010	0.0006	0.0003	0.0004	0.0003
TiO_2	0.0004	0.0004	0.0009	0.0006	0.0004	0.0002	0.0003
$H\delta_A$	0.0508	0.0579	0.1164	0.0822	0.0882	0.0476	0.0722
$H\gamma_A$	0.0994	0.0739	0.0819	0.0915	0.0761	0.0819	0.1036
$H\delta_F$	0.1054	0.1052	0.1534	0.1183	0.0951	0.0289	0.0411
$H\gamma_F$	0.0991	0.1081	0.0707	0.0884	0.0974	0.0427	0.0606

Table 4.7: For comparison, this table shows the random error on the Lick indices.

4.6 Future work

In this chapter I have experimented with a range of ways of parameterising galaxy spectra. I have also created a high resolution version of the Lejeune et al. (1998) library of stellar spectra for use in population synthesis. Since some of these spectra are not available at high resolution, it was not possible to completely finish this library. Hence it would be useful to get the complete grid of NextGen spectra to fill in the gaps in the M-dwarfs and also to find a library (if one exists) of M-giant spectra at higher resolution, to replace the low resolution Fluks et al. (1994) and Bessell et al. (1991) spectra.

With respect to parameterising the galaxy spectra, I found that the direct methods of empirical population synthesis (least squares fitting and direct inversion) were not practical for the large matrices I was dealing with. One possibility would be to parallelise the direct inversion code so that it could cope with the larger matrices. However the other limitations of this method mean I do not think it would be worth doing this.

Once the high resolution library of stellar spectra is complete it will be an important resource for doing high resolution population synthesis. An obvious application would be to investigate the age-metallicity degeneracy using a grid of high resolution synthetic galaxies. Some of the Lick indices are already known to correlate better with age or with metallicity. A grid of synthetic spectra may allow further constraints to be placed on this.

CHAPTER 5

Galaxy stellar populations and their dependence on environment

5.1 Introduction

Large surveys allow the study of subtle statistical trends across a massive number of objects. This chapter is concerned with how the spectral properties of galaxy spectra change with their local density. The local density of a galaxy is a measure of the number of other galaxies in its immediate environment. There are clear differences in the nature of galaxies at both extremes: a lone field galaxy is generally different to a galaxy near the centre of a massive cluster. Davis and Geller (1976) showed that elliptical galaxies are more strongly clustered than spiral galaxies. Combining this with the observation that the fraction of elliptical galaxies in clusters increases as local density increases (Dressler, 1980) gives the morphology-density relation. Many studies of galaxy properties (particularly elliptical galaxies) focused mainly on galaxies in clusters. Measuring the local density of each galaxy in a large survey allows you to look at how the trends change as you move from the field galaxy, through galaxies in small

groups, to galaxies in much richer environments like clusters. Several large area surveys have allowed the study of trends as a function of local environment (*e.g.* Faber et al., 1989; da Costa et al., 2000), however these have had much smaller samples than the SDSS.

Although galaxies are very different from each other, their properties do form several well established correlations. Spiral galaxies show a good correlation between rotation and luminosity, the Tully-Fisher relation (Tully and Fisher, 1977). Elliptical galaxies form a Fundamental Plane of radius, luminosity, velocity dispersion and surface brightness (Djorgovski and Davis, 1987; Dressler et al., 1987). The line index properties of elliptical galaxies provide some insight into their homogeneity by showing that they have old stellar populations. This supports the theory that they formed early, rather than at late times as a result of mergers between less massive galaxies (see Worthey et al., 1994; Vazdekis et al., 1996; Tantalo et al., 1998). A good reference about the properties of galaxies in a cosmological context is Combes et al. (1995).

There is strong empirical evidence that galaxy properties are significantly affected by the density of their environment. In particular properties such as star formation rates (SFRs) (Dressler et al., 1985), gas content (Solanes et al., 2001) and morphology (Dressler, 1980) have strong trends with local density. Merchán and Zandivarez (2002) constructed a groups catalogue with the 100 K public data release from the 2dF. Using the PCA based η parameters of Madgwick et al. (2002) as a representation of star formation rate, Martínez et al. (2002) find that the fraction of galaxies with high star formation rates is strongly correlated with the virial mass of the group they are located in. Gómez et al. (2003) have studied star formation rate as it changes with local density in the SDSS. They used the equivalent width of Hα as a measure of star formation rate and found that the SFR is lower in dense environments than in the field population.

In a theoretical context, whether we expect galaxy properties to be significantly affected by the density of their environment depends on our theories of galaxy formation. In the standard cosmological paradigm, the structure we observe in the universe today is the result of hierarchical clustering. In this scenario, small scale fluctuations in the initial density field (observed as temperature fluctuations in the CMB) collapse under their own gravity, forming dark matter haloes. Through a series of mergers these form increasingly massive systems. Galaxies then

form when the gas cools and forms stars in the centre of the dark matter haloes. Hence in this paradigm, the structure, evolutionary history and large scale distribution of galaxies is determined by the structure, evolutionary history and large scale distribution of the surrounding dark matter haloes. A study of the formation of evolution of dark matter haloes by Lemson and Kauffmann (1999), using semi-analytic galaxy formation models in conjunction will N-body simulations, found that only the mass distribution of dark matter haloes varied as a function of environment. This led them to conclude that none of the other properties of dark matter haloes were directly dependent on environment. In other words, and trends in the morphology, luminosity, surface brightness and star formation rate with environment arise because galaxies are preferentially found in higher mass haloes in overdense environments and lower mass haloes in underdense environments.

In this chapter I will be investigating how the Lick indices change with the local density of galaxies. The purpose of the Lick indices and how they are defined have been described in Section 4.5. The Lick indices are sensitive to changes in a galaxy's age and metallicity — although there is a well known degeneracy between age and metallicity in terms of their effect on galaxy spectra (see Worthey et al., 1994). Some good references about how local environmental factors such as metallicity affect Lick indices (within globular clusters and synthetic populations) are Tripicco and Bell (1995), Puzia et al. (2002) and Thomas et al. (2003). There are well known trends of metallicity with the properties of individual galaxies, for example more massive galaxies tend to be more metal rich. The aim of this chapter is to see whether there is any trends between Lick index strength in galaxies and their environments.

Section 5.2 provides the relevant details of the SDSS from which my sample of galaxies has been drawn. The process of measuring local density, specifically in the 2dF groups catalogue is discussed in Section 5.3. Section 5.4 outlines the sample selection and basic properties of the sample. Because of the clear differences between elliptical and spiral (or red and blue) galaxies, trends for each group are considered separately as well as for the entire sample. The process of splitting the sample into these two groups is described in Section 5.5. Finally, the results are presented in Section 5.6 and ideas for future work in Section 5.7.

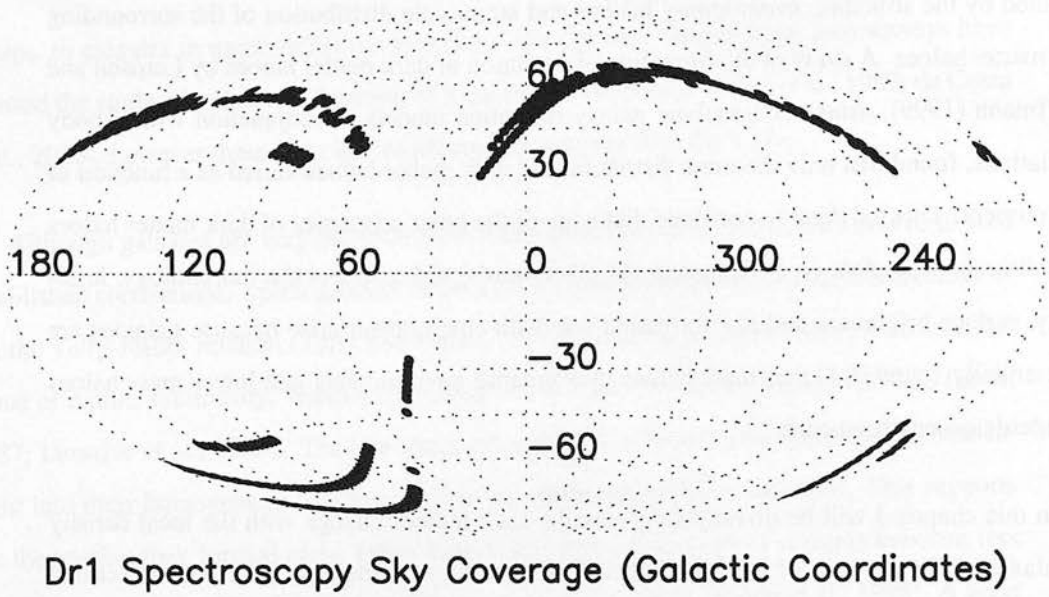

Figure 5.1: The spectroscopic coverage of the SDSS DR1, in galactic coordinates. Image source: `http://www.sdss.org/dr1/`

5.2 The Sloan Digital Sky Survey

The SDSS is a large redshift survey which, when finished, will have observed around 1 million objects covering a quarter of the sky. It consists of both imaging and spectroscopic data. So far there have been two data releases, the Early Data Release (EDR) (Stoughton et al., 2002) and Data Release 1 (DR1) (Abazajian et al., 2003). Figure 5.1 shows the spectroscopic coverage of DR1. Figure 5.2 shows the distribution of the main sample of DR1 galaxies (a total of 78 275) in redshift space.

This section outlines the basic properties of the SDSS, focusing on the spectra and measured properties that are most relevant to this work. There are several publications from the SDSS collaboration that deal with each aspect of the survey in detail. The technical details of the survey are given by York et al. (2000). The target selection procedure for the main galaxy sample is described by Strauss et al. (2002), the spectroscopic selection procedure is given by Blanton et al. (2003a) and the SDSS photometric system is described by Fukugita et al. (1996).

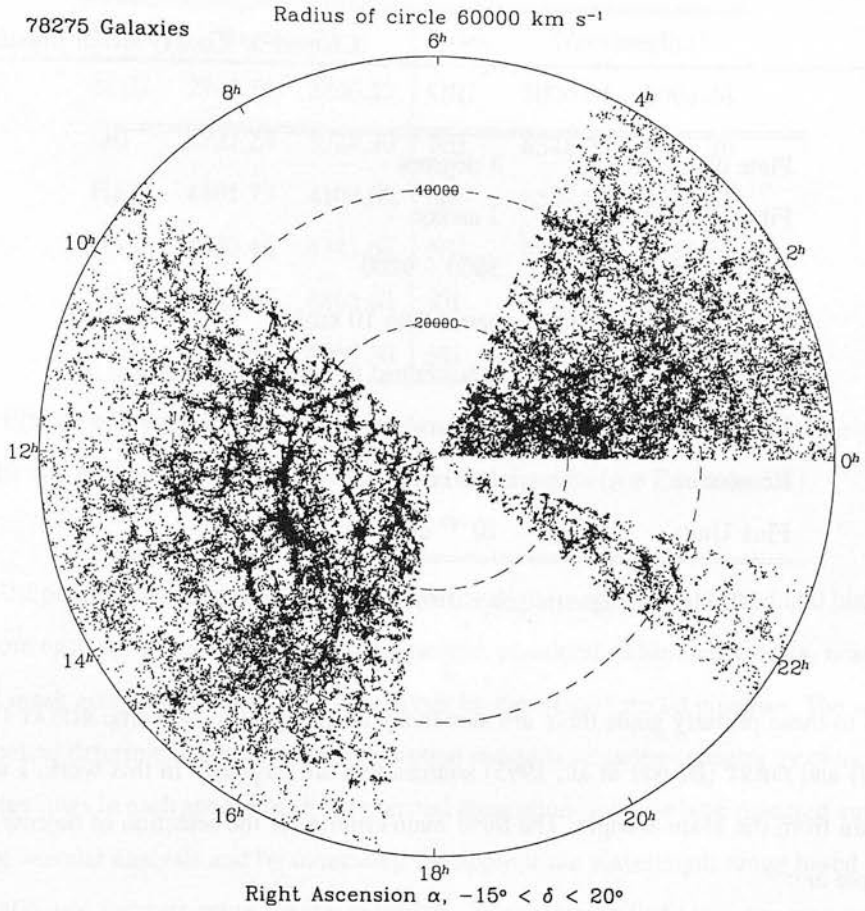

Figure 5.2: The distribution of DR1 galaxies in redshift space. Image source: `http://www.sdss.org/dr1/`

5.2.1 Spectra

The spectroscopic survey is predominantly a survey for bright galaxies, luminous red galaxies and quasars and as a result, most of the fibres are allocated to one of three samples:

1. Bright galaxies (the Main Sample) with Petrosian r-band magnitude < 17.77
2. Luminous red galaxies with Petrosian r-band magnitude down to 19.5
3. Quasars, targeting quasar candidates as faint as $i < 20.2$

Plate diameter	3 degrees
Fibre diameter	3 arcsec
Wavelength coverage	3800 – 9200
Wavelength calibration	better than 10 km/s
Wavelength reference	heliocentric vacuum wavelengths
Binning	log-lambda, 69 km/s per pixel
Resolution	1850 to 2200
Flux Units	10^{-17} erg/s/cm^2/

Table 5.1: General properties of the SDSS spectra.

In addition to these primary goals there are also many stellar spectra and some ROSAT (Voges et al., 1999) and FIRST (Becker et al., 1995) sources that are targeted. In this work, I will be using spectra from the Main Sample. The three main criteria for the selection of objects in the Main Sample are:

1. $r_{PSF} - r_{model} > s_{limit}$
2. $r_{petro} < r_{limit}$
3. $\mu_{50} < \mu_{50,limit}$

where r_{PSF} is an estimate of the magnitude using the local PSF as a weighted aperture, r_{model} is an estimate of the magnitude using the better of a de Vaucouleurs and an exponential fit to the image, r_{petro} is a modified form of the magnitude described by Petrosian (1976) and μ_{50} is the half-light surface brightness, defined as the average surface brightness within the radius that contains half of the Petrosian flux. The different magnitudes mentioned above are described in Section 5.2.2. For most of the survey, the values for these limits are: $s_{limit} = 0.3$, $r_{limit} = 17.77$ mag and $\mu_{50,limit} = 24.5$ mag in 1 arcsec^2.

Table 5.1, reproduced from the SDSS website[1], shows the main properties of the SDSS spectra. The spectroscopic pipeline consists of two stages — `spectro2d` and `spectro1d`. The

[1] `http://www.sdss.org/dr1`

Index	Wavelength ()		Index	Wavelength ()	
MgII	2799.50	2800.32	OIII	5006.54	5008.24
OII	3727.24	3728.30	NII	6548.05	6549.86
Hδ	4101.73	4102.89	Hα	6562.80	6564.61
Hγ	4340.46	4341.68	NII	6583.45	6585.27
Hβ	4861.36	4862.68	SII	6716.44	6718.29
OIII	4958.91	4960.30	SII	6730.82	6732.67

Table 5.2: Emission lines measured in SDSS galaxies. The left hand value for each line is in air wavelengths and the right hand value is in vacuum wavelengths (see Equation 5.1).

`spectro2d` pipeline reduces the raw data and calibration images from the red and blue CCD cameras from each spectrograph and produces merged, co-added, calibrated spectra, noise estimates, and mask arrays (see Table 5.4) for analysis by the `spectro1d` pipeline. The `spectro1d` pipeline determines emission and absorption redshifts, classifies spectra by object type, and measures lines in each spectrum. Emission and absorption lines are both detected automatically using wavelet analysis and by measuring the appropriate wavelength range based on the highest confidence redshift value for the spectrum. The emission lines that are measured for galaxy spectra are given in Table 5.2. All the spectra are given a rough classification as part of the pipeline. The distribution of these classifications for the 186 250 DR1 objects with spectra is shown in Table 5.3.

5.2.2 Magnitudes

Dealing with the SDSS magnitudes can be confusing as several different magnitude systems have been used throughout the progress of the survey. The original magnitude system, as described by Fukugita et al. (1996), is denoted with primes ($u'\,g'\,r'\,i'\,z'$). The system used in the EDR and associated papers is denoted with asterisks ($u^*\,g^*\,r^*\,i^*\,z^*$). The new system, used in the DR1 and associated papers has no superscript ($u\,g\,r\,i\,z$). The differences between the different systems are small, typically no more that a few hundredths of a magnitude. The filters for the DR1 magnitude system are shown in Figure 5.3.

Type	Number
Galaxies	134 000
Quasars ($z < 2.3$)	17 700
Quasars ($z > 2.3$)	980
Stars	17 600
M stars and later	4500
Sky spectra	9700
Unknown	1770
Total	186 250

Table 5.3: Pipeline classifications of the DR1 spectra.

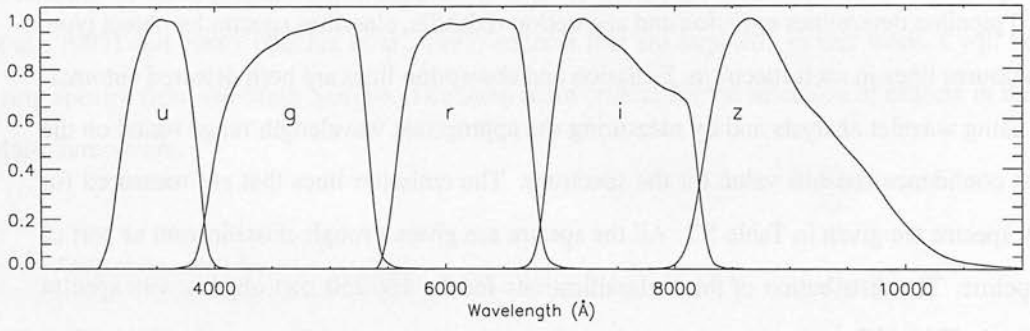

Figure 5.3: The SDSS ($u\,g\,r\,i\,z$) magnitude filters.

There are also several different types of magnitudes, each of which is most appropriate for certain applications.

- **PSF magnitudes:** For isolated stars, which are well-described by the point spread function (PSF), the optimal measure of the total flux is determined by fitting a PSF model to the object.

- **fibre magnitudes:** Defined as the flux contained within the aperture of a spectroscopic fiber (3″ in diameter) for each waveband.

- **Petrosian magnitudes:** Measuring galaxy fluxes is more difficult than measuring stellar fluxes, because galaxies do not all have the same radial surface brightness profile. To

avoid biases it is desirable to measure a constant fraction of the total light, independent of the position and distance of the object. To satisfy these requirements, the SDSS uses a modified form of the Petrosian (1976) system, measuring galaxy fluxes within a circular aperture whose radius is defined by the shape of the azimuthally averaged light profile.

- **model magnitudes:** Just as the PSF magnitudes are optimal measures of the fluxes of stars, the optimal measure of the flux of a galaxy would use a matched galaxy model. To measure model magnitudes each image is fitted with a de Vaucouleurs profile and an exponential profile. To ensure the colours can be measured accurately the flux is measured through equivalent apertures in all bands. Then the model (exponential or de Vaucouleurs) of higher likelihood in the *r* filter is selected and applied (*i.e.* allowing only the amplitude to vary) in the other bands after convolving with the appropriate PSF in each band.

5.2.3 Line indices

The SDSS `spectro1d` pipeline calculates the Lick indices plus some extra line indices as part of the standard reduction procedure. These indices are included in the released FITS data files for each source. When the EDR was released, several approximations were made in the way the Lick indices were calculated in the `spectro1d` pipeline, and hence it is not recommended that the indices included in the EDR spectra files be used. I modified the pipeline code to calculate the indices and index errors according to the definitions given in Section 4.5 and these modifications have now been incorporated into the pipeline, so the indices and errors included with the DR1 spectra are correct.

The SDSS spectra have a mask array which gives information about the quality of each pixel in the spectrum. For example, if there are sky lines or other problems that affect the particular pixel they can be masked out. The full set of SDSS masks is given in Table 5.4. The Lick indices should only be calculated using good quality data, so in calculating the indices, the SDSS pipeline does not use pixels that have the masks FULLREJECT, NOSKY, BRIGHTSKY or NODATA. This means the equations defining the Lick indices (4.12, 4.13, 4.15 and 4.16) have to be adjusted so that they only sum over unmasked pixels. When calculating the Lick

indices I found that there were still problems due to bad pixels near the index bandpass. Hence I also used the masks BADSKYCHI and NEARBADPIXEL. Also, if several pixels in the index bandpasses (or those used for calculating the pseudo-continuum) are masked, then the value of the index can be strongly affected. For this reason, I chose to calculate Lick indices only for those spectra with less than 3 pixels masked.

The SDSS spectra are all quoted in vacuum wavelengths, whereas most Lick index bandpasses (such as those in Table 3.2) are quoted in air wavelengths. Hence a small adjustment must be made to the index bandpasses (for an example of the magnitude of this adjustment, see Table 5.2 which gives air and vacuum wavelengths for some of the major emission lines). The standard formula for converting between vacuum and air wavelengths is (from Morton, 1991)

$$\lambda_{\rm air} = \lambda_{\rm vac}\left[1 + 2.735\times10^{-4} + \frac{131.4182}{\lambda^2_{\rm vac}} + \frac{2.767\times10^{8}}{\lambda^4_{\rm vac}}\right]^{-1}. \qquad (5.1)$$

Also, when using the SDSS Lick indices, note that they are calculated using the bandpass definitions from Worthey et al. (1994) rather than the revised version from Trager (1997) which I use throughout this thesis.

5.3 The 2dF groups catalogue

At the time of starting this work, the SDSS had not finished their measurements of the local density distribution. However, the 2dF did have a groups catalogue in preparation, and so I have used this instead.

There are two distinct approaches to measuring the density distribution of a large sample of galaxies. One is to define a continuous parameter (such as the two-point correlation function) which results in a smooth map of changing density. The other is to consider discrete groups of galaxies which represent the various bound systems in the survey region. The method used here is the latter, *i.e.* I am using a group catalogue in which every galaxy in the 2dF survey has been assigned membership to a group of two or more galaxies, or determined to be an isolated galaxy and hence not in a group. This catalogue is the largest groups catalogue currently available, created from a sample of ~ 190 000 galaxies. About 53% of the galaxies are placed into groups

#	Mask name	Description
0	NOPLUG	Fiber not listed in plugmap file
1	BADTRACE	Bad trace from routine TRACE320CRUDE
2	BADFLAT	Low counts in fiberflat
3	BADARC	Bad arc solution
4	MANYBADCOLUMNS	> 10% pixels are bad columns
5	MANYREJECTED	> 10% pixels are rejected in extraction
6	LARGESHIFT	Large spatial shift between flat and object pos'n
7	BADSKYFIBER	Sky Fiber shows extreme residuals
8	NEARWHOPPER	Within 2 fibers of a whopping fiber (inclusive)
10	SMEARIMAGE	Smear available for red and blue cameras
11	SMEARHIGHSN	S/N sufficient for full smear fit
12	SMEARMEDSN	S/N only sufficient for scaled median fit
16	**NEARBADPIXEL**	Bad pixel within 3 pixels of trace
17	LOWFLAT	Flat field less than 0.5
18	**FULLREJECT**	Pixel fully rejected in extraction (INVVAR=0)
19	PARTIALREJECT	Some pixels rejected in extraction
20	SCATTEREDLIGHT	Scattered light significant
21	CROSSTALK	Cross-talk significant
22	**NOSKY**	Sky level unknown at this wavelength (INVVAR=0)
23	**BRIGHTSKY**	Sky level > flux + 10*(flux_{err}) AND sky > 2.0 * median
24	**NODATA**	No data available in combine B-spline (INVVAR=0)
25	COMBINEREJ	Rejected in combine B-spline
26	BADFLUXFACTOR	Low flux-calibration or flux-correction factor
27	**BADSKYCHI**	Relative $\chi^2 > 3$ in sky residuals at this wavelength
28	REDMONSTER	Contiguous region of bad χ^2 in sky residuals

Table 5.4: Mask definitions for the SDSS spectra. When low numbered flags (< 16) are set, those will be set for half of the spectra – either the blue or red spectrograph. The higher-numbered flags (≥ 16) are set for individual pixels. The masks that I used when calculating the Lick indices in this chapter are shown in bold text.

containing at least two members (of which there are 28 213). Of these, there are 6773 groups which contain at least four galaxies. This section outlines how the groups catalogue is created.

The 2dF Galaxy Redshift Survey (2dFGRS) (Colless et al., 2001) is a massive redshift survey covering approximately 1500 square metres of sky, carried out at the Anglo-Australian Observatory. It consists of spectra for 245 591 objects, mainly galaxies, above an extinction-corrected magnitude of $b_J = 19.45$. Of these, good quality redshifts have been measured for 221 414 galaxies. The survey details are described in Colless et al. (2001) and the final data release in Colless et al. (2003). More information and data products are available from the 2dFGRS website [2].

A groups catalogue is created from the raw data (in this case a subset of $\sim$ 190 000 galaxies from the 2dFGRS) using a groupfinder algorithm. Given a set of galaxies with angular positions and redshifts, the aim of the groupfinder algorithm is to create subsets of galaxies that are the most likely to represent the bound structures that exist in the survey. It aims to minimise the amount of contamination by nearby, but physically separate, objects while at the same time trying not to miss any of the true group members. Which of these goals is most important will depend on the specific application. In practice the groupfinder algorithm achieves a compromise between these two goals.

The groupfinder algorithm used to create this catalogue is a Friends-of-Friends (FOF) percolation algorithm, which is the standard class of algorithms used to find groups in redshift surveys. The algorithm works by linking together all the galaxies within a particular linking volume of each galaxy. The particular nature of the algorithm is specified by the shape and size of the linking volume and how it varies throughout the survey. Since the number density of galaxies varies as a function of redshift, it is necessary to scale the linking volume in order to produce galaxy groups of a similar overdensity, regardless of the redshift. The scale of the linking volume is chosen so that for a group of galaxies sampled at varying completeness, the edges of the recovered group are in the same place. In redshift space groups of galaxies will appear elongated along the line of sight and so the shape of the linking volume used is cylindrical (rather than spherical) to account for this. The optimal parameters for the groupfinder

[2] http://msowww.anu.edu.au/2dFGRS/

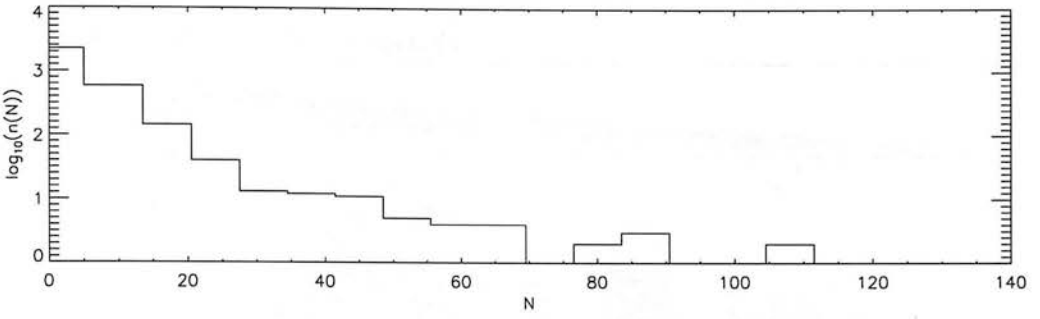

Figure 5.4: The distribution of group sizes in the NGP groups catalogue.

algorithm were obtained by testing on a mock 2dFGRS catalogue constructed using N-body simulations. For more details of the groupfinder algorithm and the specific parameters used see Eke et al. (2003).

The resulting catalogue consists of a group size for each galaxy (*i.e.* how many galaxies are in the group it is located in) and a velocity dispersion σ for each group [3]. The velocity dispersion is a measure of the spread of the individual galaxies velocities around the mean velocity of the group. It is calculated using

$$\sigma = \sqrt{\max(0, \frac{N\sigma_{gap}^2}{N-1} - \sigma_{err}^2)} \tag{5.2}$$

where

$$\sigma_{gap} = \frac{\sqrt{\pi}}{N(N-1)} \sum_{i=1}^{N-1} w_i g_i \tag{5.3}$$

and σ_{err} is the redshift error. The g_i terms are the differences between the recession velocities of the N galaxies in the group, in size order, *i.e.*

$$g_i = v_{i+1} - v_i, \quad i = 1, 2, \ldots, N-1 \tag{5.4}$$

and the w_i terms are weights given by

$$w_i = i(N-i)\ . \tag{5.5}$$

The distribution of group sizes for the North Galactic Plane (NGP) is shown in Figure 5.4.

[3] I will use σ to mean *group* velocity dispersion throughout this chapter. Note that some studies of spectral properties with environment focus on the *galaxy* velocity dispersion (also σ).

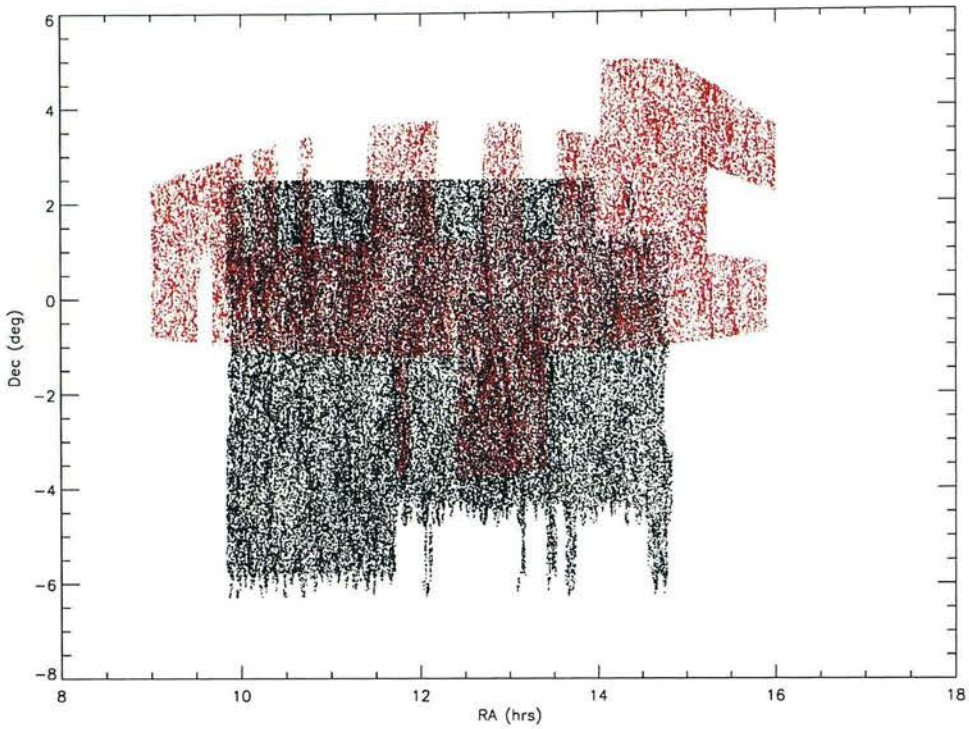

Figure 5.5: The region of overlap between the 2dF NGP groups catalogue (black) and the SDSS DR1 data (red).

5.4 Sample selection and selection effects

As I am using galaxies from the SDSS in conjunction with local density information from the 2dF groups catalogue, I first had to cross-match the two catalogues. This restricted me to using the region of overlap between the 2dF catalogue and the SDSS DR1 catalogue. This overlap region is shown in Figure 5.5. Cross-matching the two catalogues resulted in an initial sample of 15 569 galaxies.

However, when any sample is selected like this, it is likely that it is magnitude limited. This means that the relative numbers of intrinsically bright and faint galaxies that we see may not correspond to the relative numbers per unit volume of space. Bright galaxies are over-represented and the average luminosity of the galaxies we see increases with distance. This bias can be avoided by selecting a volume-limited sample. In the SDSS, the photometric limit

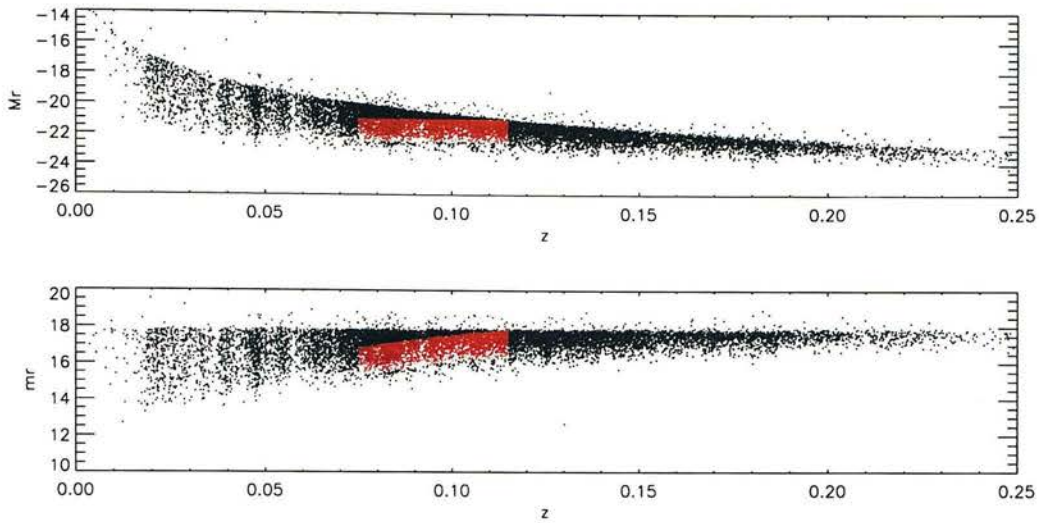

Figure 5.6: Illustration of the luminosity bias as it affects my sample of 15 569 galaxies. The lower panel shows apparent magnitude m_r versus redshift. The cutoff, r_{limit} is 17.77. The upper panel shows the absolute magnitude M_r for the same galaxies. Moving to higher redshifts, only the brightest galaxies are visible. The red sources form a volume limited sample, as described in the text.

for spectroscopic targeting is $r_{limit} = 17.77$, *i.e.* only galaxies with $r < 17.77$ are targeted spectroscopically. Figure 5.6 shows the affect of this bias in my sample of 15 569 galaxies. The apparent magnitude cutoff of 17.77 (bottom panel) means that as you go to higher redshifts, only the brightest galaxies are included in the sample (top panel). Selecting a volume limited sample reduces the size of the sample dramatically. The cuts shown by a red box in Figure 5.6 ($0.075 \leq z \leq 0.115$ and $-22.5 \leq M_r \leq -21.0$) result in a sample of 3873 spectra.

It is also necessary to consider selection effects resulting from magnitude limits on the 2dF groups catalogue. Because the survey is magnitude limited, all low luminosity galaxies will be missed, a bias that gets worse with increasing redshift. Groups are only detected if the number of galaxies in a certain region is greater than 3 and hence at high redshifts only larger groups will tend to be selected. The group velocity dispersion is correlated with mass and so only groups with high velocity dispersion will be found at higher redshift. This is demonstrated in Figure 5.7 which plots group velocity dispersion versus redshift for all spectra in the 2dF NGP groups catalogue. There is a clear trend of increasing group velocity dispersion with redshift.

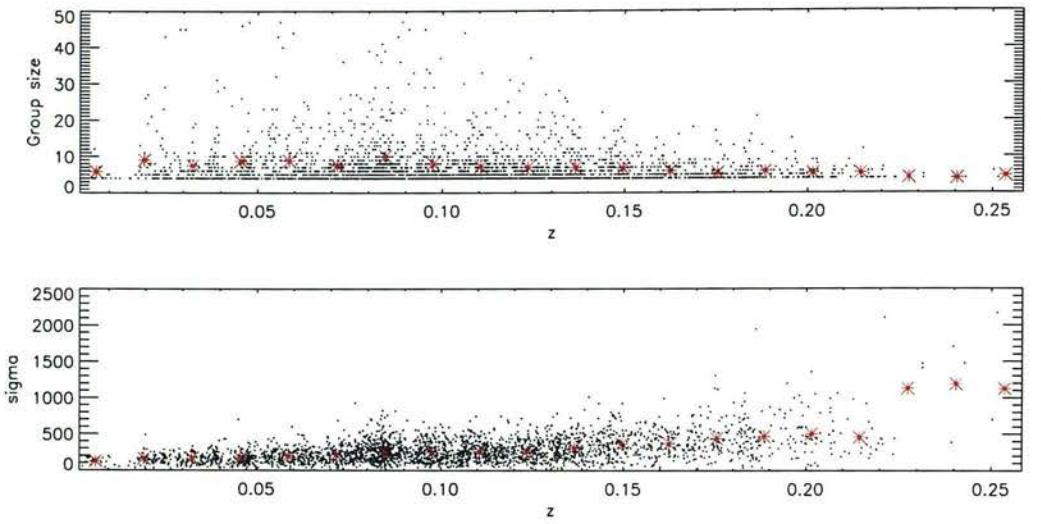

Figure 5.7: The group size (top) and velocity dispersion (bottom) for the groups in the NGP, plotted against redshift. Binned averages (for bin size of 0.013) are given by the crosses.

The fraction of galaxies that are not detected because they fall below the apparent magnitude cutoff increases with redshift and hence the number of galaxies detected in each group will not be an accurate measure of the group size. The way the velocity dispersion is calculated makes it a much more robust measure of the group size and hence I will be using it throughout this chapter.

Any trends found between Lick indices and group velocity dispersion could be either environmental (genuinely due to velocity dispersion) or evolutionary (due to redshift). Using the volume limited sample described above should resolve this problem as the average velocity dispersion does not change significantly over the limited redshift range. This is demonstrated in Figure 5.8 and confirms that the volume limited sample chosen above is a reasonable one. The final step is to select those galaxies which are located in a group (*i.e.* are not isolated galaxies). I have done this by selecting galaxies which are in a group with $\sigma \neq 0$. Of the 15 569 galaxies in the 2dF/SDSS overlap region, 5536 of these are located in groups with $\sigma \neq 0$. This corresponds to 1679 galaxies in the volume limited sample.

As discussed in Section 5.2.2 there are four different types of magnitudes in the SDSS survey. In the work following I use both *Petrosian* and *model* magnitudes. Figure 5.9 shows a

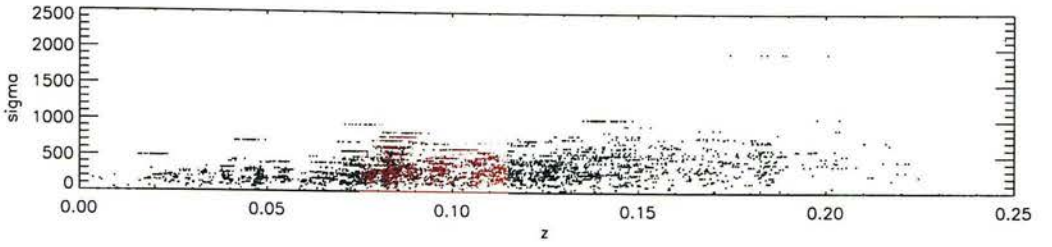

Figure 5.8: Velocity dispersion with redshift for the 15 569 sources in my sample. The red sources form a volume limited sample, as described in the text. Of the 15 569 galaxies 5536 are located in groups with $\sigma \neq 0$ (*i.e.* 10033 sources are located at $\sigma = 0$ in this plot).

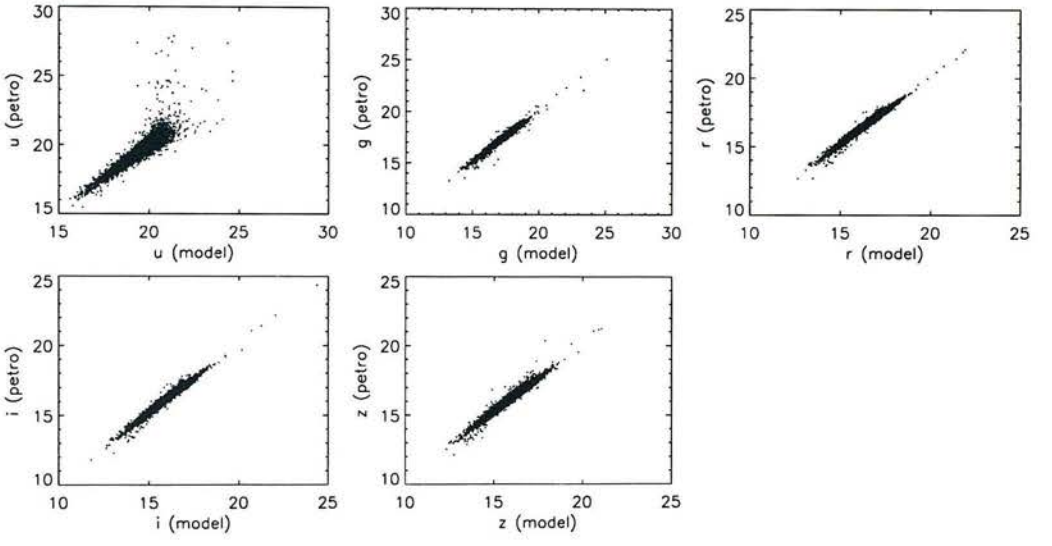

Figure 5.9: A comparison of the Petrosian and model magnitudes for my sample. The different magnitudes are described in Section 5.2.2.

comparison of these different magnitudes for the sample I have selected. The advantage of the model magnitudes is that they give a higher signal-to-noise measurement than the Petrosian magnitudes. The agreement between the two types of magnitudes is generally quite good, although the scatter is higher in the u band. This is mainly because the u-band flux is generally quite low and aperture photometry includes significant Poisson noise and background subtraction uncertainties.

5.5 Colour magnitude separation

There is a well established bimodality in large galaxy samples, due to the presence of two different populations: early type galaxies (E/S0) and late type galaxies (Sa-Sd spirals and irregulars). These two morphological types occupy different regions of the colour magnitude diagram (Tully et al., 1982). Treating these two distinct groups as one sample could hide any trends that may be present, and so it is important to separate them. Redshift surveys such as SDSS allow the colour bimodality to be quantified without using morphological information directly, which is an advantage since morphology becomes difficult to measure accurately as redshift increases. It is interesting to study the nature of the colour bimodality as it is likely that it is due to different physical processes in galaxy formation (Budavari et al., 2003). This has been done by several people for samples of SDSS galaxies. For example Strateva et al. (2001) show that the galaxies can be separated well into two groups, roughly corresponding to morphological types, using the $g-r$ versus $u-g$ colours, in conjunction with the g versus $u-r$ colours.

I have separated the galaxies into two groups using the separation method proposed by Baldry et al. (2003). The main difference between the Baldry et al. (2003) method and previous methods is that they do not use a cut in morphology or in spectral type to divide the galaxies into two groups. The basis of their approach is to assume that the colour distribution of galaxies can be approximated by the sum of two 'normal' Gaussian functions, a *bimodal* function. They use the rest frame $u-r$ colour as their spectral-type indicator, which is defined by

$$C_{ur} = (u_{model} - k_u) - (r_{model} - k_r) \tag{5.6}$$

where k_u and k_r are k-corrections to the magnitudes (see Equation 1.20). There is a clear bimodality in the galaxy distributions, obvious directly from plotting C_{ur} versus M_r.

The sample used by Baldry et al. (2003) is derived from the SDSS large scale structure `sample11` which covers 2420 square degrees. It was then magnitude limited using $13.5 < r < 17.5$ over 29% of the area and $13.5 < r < 17.77$ over 71% of the area, resulting in a sample of 208 570 items This sample was further restricted by selecting a low redshift range ($0.004 < z < 0.080$) and making a cut in absolute magnitude ($-23.5 < M_r < -15.5$) resulting in

a final sample of 66 846 galaxies. The method used by Baldry et al. (2003) can be summarised as follows. Firstly they corrected for sample incompleteness. Then they assumed that the bivariate distribution is the sum of two distinguishable distributions

$$\Phi_{comb} = \Phi_r + \Phi_b \, . \tag{5.7}$$

The red and blue distributions are parameterised by

$$\Phi(M_r, C_{ur}) = \phi(M_r) G[C_{ur}, \mu(M_r), \sigma(M_r)] \tag{5.8}$$

where ϕ is the luminosity function and G is the colour function. $\mu(M_r)$ and $\sigma(M_r)$ are the mean and standard deviation of the Gaussian function in G, as shown in Equation 5.10 below. The luminosity functions were then fit with Schechter (1976) functions, which can be written in terms of magnitudes as

$$\phi(M_r) = c\phi^* e^{-c(\alpha+1)(M_r - M^*)} e^{-e^{-c(M_r - M^*)}} \tag{5.9}$$

where $c = 0.4 \ln(10)$, M^* and ϕ^* are the characteristic magnitude and number density, and α is the faint-end slope. The colour function, G, was parameterised using a Gaussian normal distribution

$$G(C_{ur}, \mu, \sigma) = \frac{1}{\sigma\sqrt{2\pi}} e^{\frac{(C_{ur}-\mu)^2}{2\sigma^2}} \, . \tag{5.10}$$

Both μ and σ were constrained to be contiguous functions of M_r, in particular a straight line and a hyperbolic tan function. The hyperbolic tan function was chosen as it was found fit the data better than polynomials with the same number of parameters.

To fit the functions to the distribution, the sample was divided into 16 absolute magnitude bins of with 0.5, from -23.5 to -15.5. Each of these subsamples were divided into 28 colour bins of width 0.1 in C_{ur}. Then double Gaussian functions were fitted to these colour distributions. For most of the bins, the double Gaussian function is a good representation of the data. It was then assumed that the Gaussian parameters vary smoothly from one absolute magnitude bin to the next. The dispersion and mean of each distribution were fitted by the straight line as hyperbolic tan functions. The resulting colour divider (optimised by considering the 'completeness' C and 'reliability' $\mathcal{R}$ of the sample following Strateva et al., 2001) is given by

$$C'_{ur}(M_r) = 2.06 - 0.243 \tanh\left[\frac{M_r + 20.07}{1.09}\right] \tag{5.11}$$

which is their Equation 11. There is some (of course unavoidable) overlap between the two distributions, but this is minimised by the chosen splitting function.

To apply this cut to my sample I first had to make several corrections to the magnitudes. The magnitudes in the SDSS database are corrected for atmospheric extinction but not for Galactic extinction. The extinction A_X of an object in some waveband X is defined to be the difference between the observed magnitude in that waveband, $m(X)$ and the waveband that would be observed in the absence of dust, $m_0(X)$

$$A_X \equiv (m - m_0)_X \, . \tag{5.12}$$

The *reddening* or colour excess, $E(X-Y)$, in some colour $X-Y$ is defined as the difference between the observed colour $m(X) - m(Y)$ and the intrinsic colour $m_0(X) - m_0(Y)$

$$E(X-Y) \equiv [m(X) - m(Y)] - [m_0(X) - m_0(Y)] = A_X - A_Y \, . \tag{5.13}$$

There is a reddening correction factor provided with each SDSS source, computed following Schlegel et al. (1998). The reddening corrections are given in magnitudes at the position of each object in the SDSS catalogue. Each correction factor is additive, *i.e.* subtracting it from the magnitudes in each band gives the corrected magnitude.

A k-correction must be applied to the galaxy magnitudes to account for the difference between emitted-frame and observed-frame bandpasses due to redshift. I calculated the k-corrections using `kcorrect` v1.16 by Blanton et al. (2003b) [4], following the definition of k-correction in Equation 1.20. When using `kcorrect` the `sdssfix` flag was turned on to give more realistic errors on the magnitudes. The final equation for calculating absolute magnitude, taking into account the extinction correction and the k-correction is given by

$$M_r = r - k_r - 5\log(D_L/10pc) \tag{5.14}$$

where r is the extinction corrected Petrosian magnitude; D_L is the luminosity distance for a cosmology with and k_r is the k-correction using `kcorrect`.

Figure 5.10 shows my sample, split with the dividing function in Equation 5.11. For the rest of this work the sources above the thick line will be considered as *red* galaxies and the

[4] See also Michael Blanton's `kcorrect` website `http://cosmo.nyu.edu/~mb144/kcorrect/`

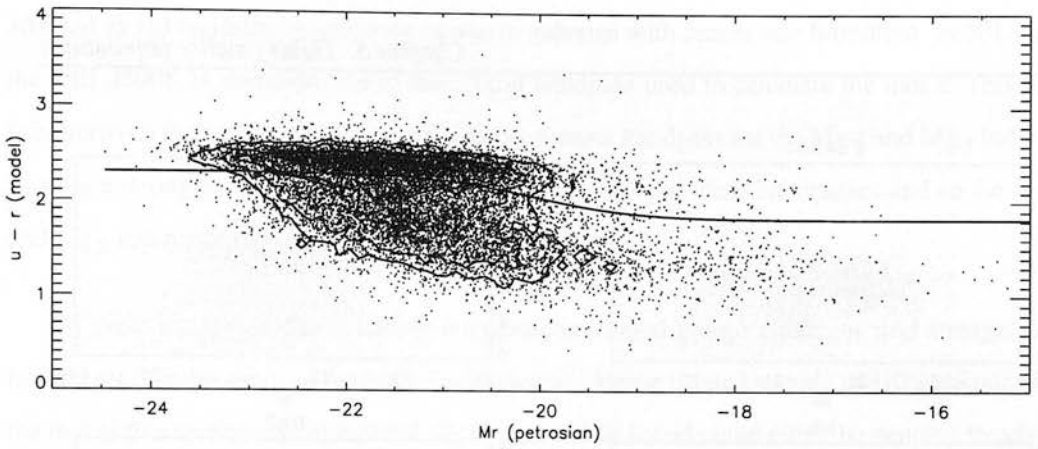

Figure 5.10: My sample (as described in the text) split with Baldry's optimal divider given by Equation 5.11. The x-axis gives the absolute r magnitude (Petrosian) and the y-axis gives $u-r$ model magnitudes.

sources below the line considered as *blue* galaxies. From the 15 569 sources in the 2dF/SDSS overlap region, 7815 are red and 7754 are blue. In my volume limited sample of 1679 galaxies in groups, 1075 are red galaxies and 597 are blue galaxies. The fraction of red galaxies is greater because blue galaxies are more likely to be field galaxies and hence not included in my sample.

5.6 Results and discussion

First I consider the entire sample of 15 569 spectra. Several of the Lick indices split the galaxies into red and blue types quite well. Figure 5.11 shows Lick index versus absolute r magnitude for four of the indices. In two of the plots (Hβ and Fe4531) it is clear that the blue and red galaxies follow a similar distribution. However, for the other two (G4300 and Mg_2) the two populations are split reasonably well by the indices. The Mg_2 index is known to correlate well with metallicity, and so this demonstrates that the redder galaxies have higher metallicity, which is what we would expect. The G4300 index corresponds to a region with a number of molecular lines and so again it is not surprising that this is clearly stronger in the red galaxies

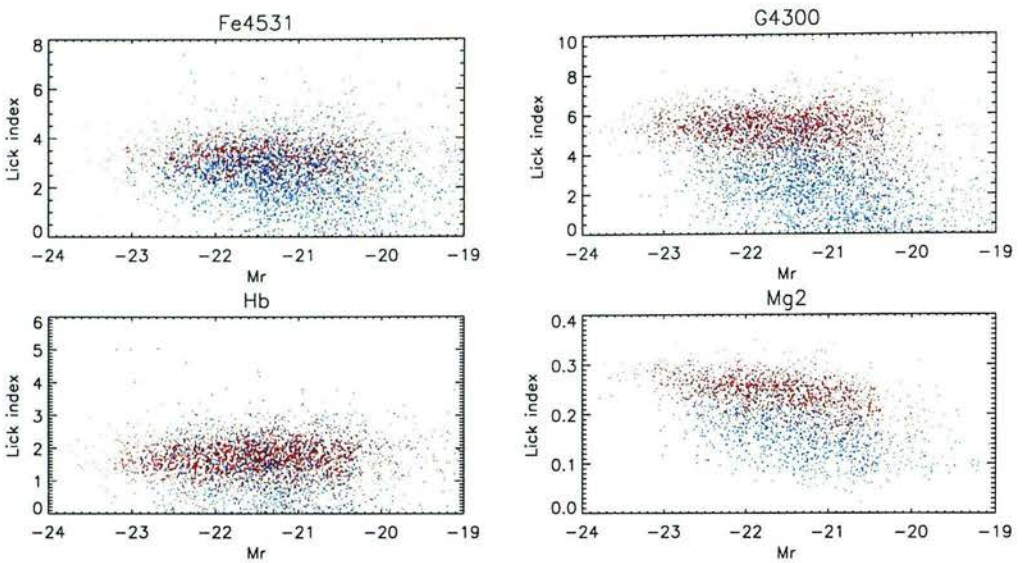

Figure 5.11: Lick indices versus M_r, demonstrating that several of the indices split the red and blue galaxies into two populations quite successfully (G4300 and Mg_2) whereas others do not (Hβ, Fe4531).

than in the blue galaxies.

As mentioned in Section 5.2, indices can be greatly affected if they have 2 or more masked pixels in either their central bandpass or one of the bandpasses used to calculate the pseudo-continuum. Because of this, there are small variations in the number of spectra in the sample that could have a particular index calculated successfully. The number of spectra in the final sample for each index is included in the results table.

Another issue is the effect of emission lines on the measurement of the Lick indices. The most extreme effect happens when an emission line swamps the actual Lick bandpass. However, the wings of nearby emission lines can be enough to dramatically change the measured value of an index. This can happen if the emission line in located near a Lick bandpass or one of the bandpasses used to calculate the continuum. The emission lines measured in the SDSS pipeline are given in Table 5.2. Only Lick indices with bandpasses between $4800 < \lambda < 5100$ are potentially affected (Hβ, Fe5015, Mg_1 and Mg_2).[5] Clearly Hβ is directly

[5] Hδ_A and Hγ_A are also affected but I am not using them in this analysis.

affected as Hβ emission is relatively strong in galaxies with recent star formation. Fe5015 has the OIII λ5008.24 emission line in the central bandpass used to calculate the index. This line falls between the central bandpass and blue continuum bandpass for the Mg_1 and Mg_2 indices. It is not a strong enough line for the wings to affect either of these bandpasses and so the Mg_1 and Mg_2 indices are also unaffected by emission lines.

To avoid the biases due to having a magnitude limited groups catalogue and a magnitude limited set of galaxies from the SDSS I will use the volume limited sample of 1679 galaxies for the rest of this section. As mentioned above, any trends found could either be genuine trends of Lick index with velocity dispersion, or an evolutionary trend with redshift. Using this sample should resolve this problem but to be sure I used the Spearmann rank-order correlation test to rule out any correlation with redshift. This is a non-parametric test, using the rank of the values in each dimension. If R_i is the rank of x_i among the other x values and S_i is the rank of y_i among the other y values then the correlation coefficient r_s is given by

$$r_s = \frac{\sum_i (R_i - \bar{R})(S_i - \bar{S})}{\sqrt{\sum_i (R_i - \bar{R})^2}\sqrt{\sum_i (S_i - \bar{S})^2}} . \tag{5.15}$$

The significance of any correlation (*i.e.* non-zero value of r_s) is tested using

$$t = r_s \sqrt{\frac{N-2}{1-r_s^2}} \tag{5.16}$$

which is distributed approximately the same as the *Student's t* distribution with $N - 2$ degrees of freedom. I used the IDL `r_correlate` routine (based on that in Press et al., 1992) which returns r_s and the probability that the correlation found is random $P(r_s)$. A value of $P(r_s)$ close to 1.0 suggests the correlation is purely random (*i.e.* there is no correlation). A value of $P(r_s)$ close to 0.0 suggests that the correlation is real.

Many of the indices show a trend with group velocity dispersion when the entire volume limited sample (1679 sources) is considered. For example, the G4300 index, shown in Figure 5.12, has $r_s = 0.129$ with $P(r_s) = 0.13 \times 10^{-7}$, a highly significant trend. However, this trend is mainly due to the changing fraction of red and blue galaxies as group velocity dispersion increases. When considered individually the red sample has $r_s = 0.033$ with $P(r_s) = 0.29$ and the blue sample has $r_s = 0.113$ with $P(r_s) = 0.01$. Since the fraction of red galaxies increases with group size, and the red galaxies, have, on average a higher value for the G4300 index

Index	N	N_r	Red r_s	$P(r_s)$	N_b	Blue r_s	$P(r_s)$
CN_1	1652	1066	**0.071**	**0.02**	586	–0.001	0.97
CN_2	1658	1068	**0.073**	**0.02**	590	0.026	0.53
Ca4227	1666	1069	0.035	0.25	597	0.064	0.12
G4300	1665	1071	0.033	0.29	594	**0.113**	**0.01**
Fe4383	1657	1069	**0.082**	**0.01**	588	**0.081**	**0.05**
Ca4455	1667	1072	0.021	0.49	595	0.062	0.13
Fe4531	1667	1072	–0.024	0.42	595	0.034	0.40
C4668	1664	1070	0.055	0.07	594	0.039	0.35
$H\beta^{\dagger}$	1664	1069	0.009	0.77	595	0.024	0.56
Fe5015†	1080	726	**0.097**	**0.01**	354	0.013	0.80
Mg_1	820	548	**0.089**	**0.04**	272	0.018	0.77
Mg_2	1014	694	**0.100**	**0.01**	320	0.063	0.26
Mg b	1151	724	0.033	0.38	427	**0.126**	**0.01**
Fe5270	1482	978	0.050	0.12	504	**0.095**	**0.03**
Fe5335	1392	925	0.042	0.20	467	0.077	0.10
Fe5406	1508	980	0.003	0.93	528	0.054	0.22
Fe5709	1155	773	0.036	0.32	382	–0.045	0.38
Fe5782	1245	807	–0.009	0.79	438	–0.017	0.73
NaD	1495	951	0.049	0.13	544	0.035	0.41
TiO_1	1367	896	0.047	0.16	471	–0.005	0.91
TiO_2	1450	994	**0.103**	**0.00**	456	0.030	0.52

Table 5.5: Spearmann rank-order correlation coefficients r_s for each of the Lick index vs. group velocity dispersion plots. Indices with a significant trend ($P(r_s) \leq 5\%$) are shown in bold. The total sample size (N) and the red and blue sample sizes (N_r and N_b) are also given. Indices marked with a dagger (†) may be affected by emission lines (see text).

then there is a stronger overall trend. For the rest of this section I will consider the red and blue samples separately to distinguish between cases where there is a trend within one of the samples and where there is a trend due to the fraction of red and blue galaxies changing.

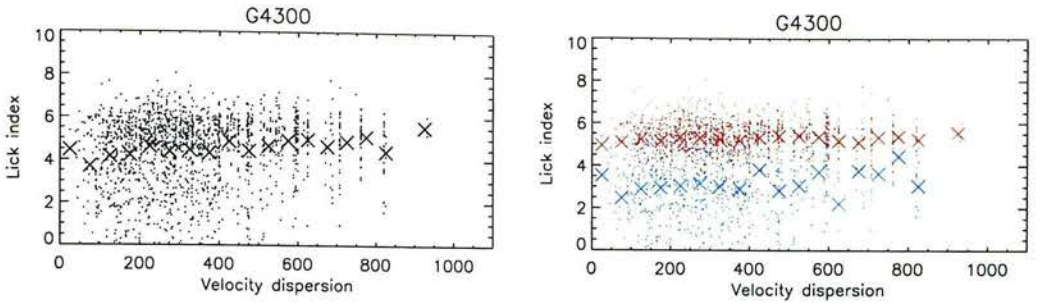

Figure 5.12: Trends for the G4300 index with group velocity dispersion, showing that the trend observed when considering both red and blue galaxies together is partly due to the changing fraction of red galaxies as velocity dispersion increases.

Figures 5.13 gives the results for each Lick index versus group velocity dispersion. Table 5.5 gives the correlation coefficients and probabilities for each plot.

5.6.1 Comments on specific indices

Tripicco and Bell (1995) showed that the Lick indices fall into several different groups based on what is the primary effect on their value. The indices that correspond largely to one strong line (Ca4227, Mg_2, Mg *b*, and Na D) are dependent on the abundance of the element forming the dominant line. Whereas, indices that consist of a band of weaker lines (G4300 and some of the Fe indices) are mainly affected by the microturbulent velocity of the star. This information is important when considering what physical change underlies changes in the Lick indices (*i.e.* it does not always correspond directly to a change in the line strength of the line for which the index is named). Most of the indices in Table 5.5 show no significant trend with group velocity dispersion. This could suggest that local density does not correlate strongly with element abundances, or that it results in many effects, some of which cancel each other out, resulting in no strong trends. Following are some comments on specific indices.

- The CN_1 and CN_2 indices cover almost the same wavelength ranges, the only difference being the range over which the blue continuum is defined (modified by Worthey et al., 1994, so that CN_2 avoids Hδ). Both measure the strength of CN λ4150 and unsurpris-

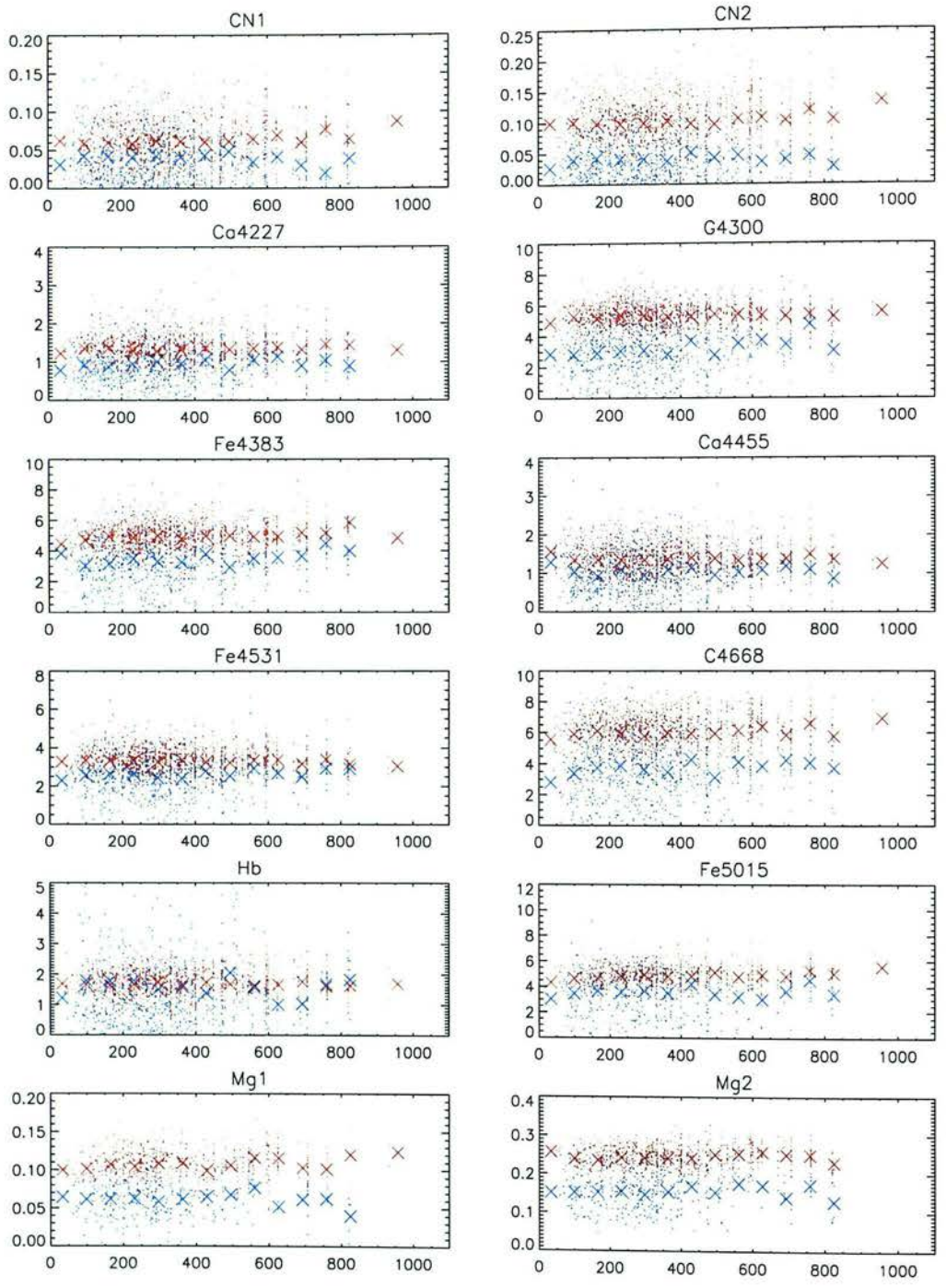

Figure 5.13: Lick index (y-axis) versus group velocity dispersion (x-axis). The red and blue samples are coloured accordingly. The crosses give binned averages for each sample.

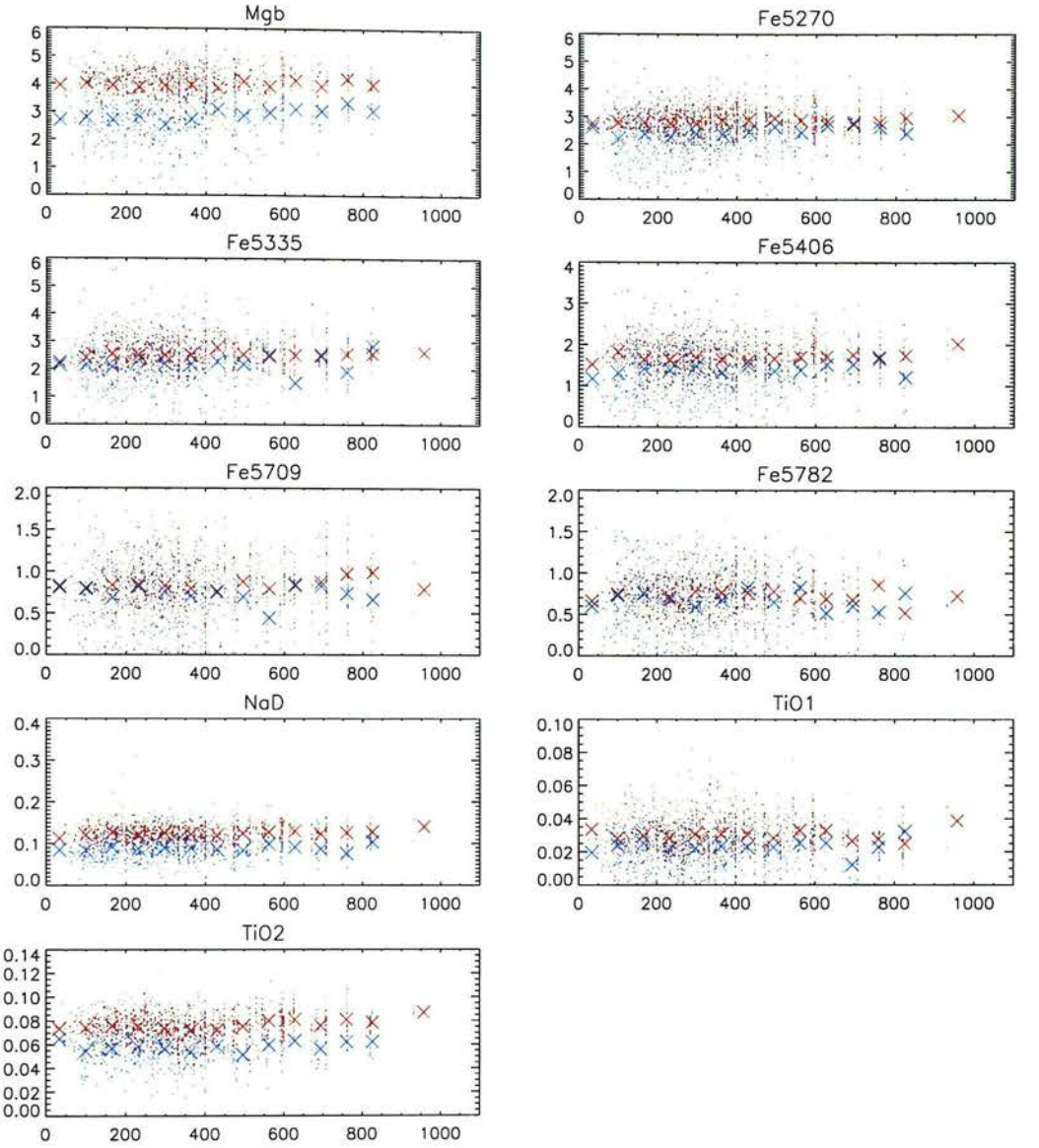

(Figure 5.13 continued.)

ingly the results for these two indices are very similar. The blue sample shows no trend with group velocity dispersion. The red sample shows a slight increase in the value of the index with increasing group velocity dispersion. Tripicco and Bell (1995) find that CN_1 and CN_2 are sensitive to changes in the carbon and nitrogen abundances, and Thomas et al. (2003) find that nitrogen abundance is the most significant factor. Nitrogen enhancement can occur when stars accrete nitrogen enriched ejecta from AGB stars. Since this happens later in the stellar lifecycle it is more likely to have occurred in older, redder

galaxies. Since these are found to be more common in rich clusters, this could explain why these indices increase with group velocity dispersion.

- G4300 is primarily sensitive to carbon and oxygen abundances and to a lesser extent titanium and iron (Tripicco and Bell, 1995). It shows no significant trend for the red sample. The blue sample shows an increase in the value of the index with increasing group velocity dispersion.

- Fe4383 is mainly affected by the strength of the dominant iron line, but also by carbon and magnesium (Tripicco and Bell, 1995). It shows trends with both the red and blue samples, both increasing with increasing group velocity dispersion.

- The Hβ index shows no trend for red or blue galaxies. This is in agreement with the results from a study of early type galaxies by Bernardi et al. (2003) who find that while Hβ showed strong evolution with redshift it had no dependence on environment for a given redshift.

- Mg_1 and Mg_2 are most sensitive to Mg abundance and to a lesser extent carbon and iron. They are two of the best metallicity indicators of the Lick indices. They both show no significant trends in the blue sample, and show an increase with increasing group velocity dispersion in the red sample. Again, this could be explained by the increased fraction of old, metal-rich galaxies that are found in larger groups. Bernardi et al. (2003) find no evidence for a change in the strength of Mg_2 with local density for early type galaxies. Both this work and theirs is somewhat limited by sample size and until a similar study is done with a larger sample the results are inconclusive.

- Mg *b* shows no significant trend in the red sample, but for the blue sample increases with increasing group velocity dispersion.

- Fe5270 shows no significant trend in the red sample, but for the blue sample increases with increasing group velocity dispersion.

- Both the TiO_1 and TiO_2 indices primarily measure the strength of the TiO absorption features. TiO lines are only present in the spectra of cool (M-type) stars. A study of Galactic globular clusters by Puzia et al. (2002) found that the clusters with the highest metallicity has the strongest TiO_2 absorption lines. TiO_2 increases with increasing group

velocity dispersion, for the red sample. This is consistent with TiO_2 being strongest in high metallicity environments within galaxies. These galaxies are more likely to be found in older, rich groups. The TiO_1 index also shows a slight increase with increasing group velocity dispersion but the significance from the Spearmann test is greater than my cutoff (16% rather than $< 5\%$). This weakens the conclusions that can be drawn from the TiO_2 trend as you would expect to find both increasing with increasing metallicity.

5.6.2 Discussion

In this section I have looked for trends between Lick indices, a very fine resolution spectral properties corresponding to absorption features in stars, and group velocity dispersion, a measure of the size of groups of galaxies. There are several areas in which problems with this type of analysis can arise. Firstly there is the issues associated with an finding accurate measure of local density. I have used the group velocity dispersion as it can be approximated with equal accuracy regardless of the redshift. However, having to restrict my study to the galaxies that fall in the overlap between the SDSS and 2dF surveys means I have dramatically decreased my original sample.

Secondly there is the difficulty of calculating the Lick indices accurately. One advantage of the SDSS is that it has a resolution high enough to allow the study of these high resolution features. However, the signal to noise ratio is not always favourable for calculating indices that are very sensitive to any changes in the spectra. One way of overcoming this problem is to co-add spectra (such as done by Bernardi et al., 2003) but this has the disadvantage of many times less spectra (particularly after they have been binned into redshift and local density) and hence smaller scale statistics. I chose not to do this, but am aware that the measurement of the indices is probably the largest factor of error in this process. It is important to note that the systematic errors in calculating the indices usually exceed the random errors discussed in Section 4.5.

Finally, once the indices have been measured and the trends plotted, there is the difficulty of assessing whether an observed trend is due to the Lick index itself changing or a measured

property that it depends on changing. For example, if the Lick index changes with redshift, and the group velocity dispersion changes with redshift, then a trend in Lick index versus group velocity dispersion might be a result of these other factors. I have tried to avoid these effects by choosing a volume limited sample and checking that there was no systematic change in group velocity dispersion over that redshift range.

Most of the indices demonstrated some overall increase with increasing group velocity dispersion when considering red and blue galaxies together. This is due to the average index for the red sample generally being slightly higher than the average index for the blue sample, and the fraction of red galaxies increasing with group velocity dispersion. When considered separately, several of the indices showed some increase with increasing group velocity dispersion for the red sample (CN_1, CN_2, Fe4383, Fe5015, Mg_1, Mg_2, TiO_2) and several for the blue sample (G4300, Fe4383, Mg *b*, Fe5270). However, these are all fairly weak trends and would have to be tested on larger samples before any conclusions can be drawn. This is particularly evident because some indices which are known to correspond to very similar underlying physical phenomena have trends which are not in agreement. For example, TiO_2 shows a trend but TiO_1 does not.

Theoretical predictions by Lemson and Kauffmann (1999) suggest that for galaxies of a given mass, we would not expect to see any change in star formation history with group size. When considering galaxies with various masses, we may expect an overall change in star formation history and metallicity with group size, due to the changing fraction of massive galaxies as the group size increases. However, work by De Propris et al. (2003) shows that although the galaxy luminosity function for galaxies in clusters is different to that of field galaxies, it is not highly dependent on the richness or size of the clusters. In other words, once we are considering galaxies located in groups or clusters, the size of the cluster does not seem to significantly affect the luminosity distribution. Hence we would not necessarily expect any change in the star formation history and metallicity properties of galaxies as local density increases. My results show that most of the Lick indices (which are tracers of metallicity and star formation) do not show any trend with group velocity dispersion, and those that do show a very weak trend. These results agree with there being no significant trend in star formation history with group size.

5.7 Future work

Clearly the most significant improvement to these results would be gained by using a larger sample. The main limiting factor in my sample size was having to combined the SDSS sources with the 2dF groups catalogue to get the local density information. Using a SDSS groups catalogue, when one becomes available, would avoid this limitation.

One aspect of this research that would be interesting to follow up would be to compare the Lick indices with principal components to get more idea of what the principal components tell us about the stellar populations in galaxies. The 2dF analysis (Folkes et al., 1999) and the SDSS analysis (Yip et al., 2003) show that the main principal components carry information about the emission lines in the galaxies. However, lower components may reveal information about the stellar populations, which would be useful since principal components are so easy to calculate. There has been some work in this area (*e.g.* Kong and Cheng, 2001) but it has mainly focused on first few principal components. A comprehensive study will compare the advantages of human selected parameters (Lick indices) with mathematically optimal parameters (PCA) in tracing physical changes in the galaxy spectra. Since the principal components are easier to calculate and more robust it would be useful to see if they reveal much information about the stellar populations.

A longer term project that ties together the work in Chapters 4 and 5 would be to use Lick indices and principal component analysis to test the predictions of semi-analytic galaxy formation models such as van Kampen et al. (1999). These models produce a distribution of galaxies, which used in conjunction with galaxy spectral synthesis packages produces a synthetic redshift survey. It would be interesting to test these models by investigating whether the predicted distributions of Lick indices corresponded to the observed distributions in the SDSS.

CHAPTER 6

Conclusions

The overall motivation for this thesis was to study the way spectral properties of galaxies vary with their local environment. This is a question that, in an era of massive redshift surveys such as the 2dF and the SDSS, it is now possible to provide some answers to. I had available large datasets of galaxies from the completed 2dF survey, and also from the continuing SDSS results. However, to make use of these it was necessary to develop better tools for comparison of synthetic spectra to the observational data.

One important aspect of dealing with large datasets is the ability to classify objects automatically. This also requires some form of information extraction (preferably automatic) to take place before the classification stage. In Chapter 2 I have carried out a comparative study of different automatic classification methods that have been used in the literature. I highlighted some of the difficulties with these methods, probably the most significant one being the lack of good training data. Ideally training data should be a subset of the data that is to be classified, and this is an issue that needs to be resolved before machine learning methods can be used in 'real-world' astronomy problems like classifying stellar spectra in the SDSS. The current state of the art in this field is neural network classification. In the final section of Chapter 2 I introduce Support Vector Machines, which have not be used widely in astronomy, although they

have been shown to be successful in other applications. While the results I get do not better the ones obtained using neural networks, this was only after a comparatively small amount of experimentation and so I think there is still potential for these to be useful in stellar classification. Some possible directions for future research on this topic are; testing support vector machines more extensively on a wider range of astrophysics classification problems, trying different types of support vector machines and looking more deeply into the theoretical basis for selecting a good kernel.

Returning to the main aim, which was to generate synthetic galaxy spectra to compare with spectra from the SDSS, the resolution of existing libraries of synthetic spectra proved to be a limiting factor. To make full use of the SDSS spectra it was desirable to have synthetic galaxy (and hence stellar) spectra at a resolution of 2 (as opposed to the 20 spectra normally used). In Chapter 3 I present a library of 2 resolution Kurucz spectra that covers a wide range of physical parameters. To confirm the accuracy of these spectra I compare them to the old 20 Kurucz spectra and also to a library of observed spectra at a similar resolution, STELIB. I found some differences between the colours of the 20 and 2 spectra, which are due to changes in the data and software between the generation of the two sets. The library I have produced covers the same range in physical parameters as the original library of Kurucz spectra, with the exception of the low temperature stars ($T_{\rm eff} < 5000$K). Due to the large number of TiO lines the low temperature spectra contain, they are very slow to generate and I did not have the resources to complete these during my PhD. However, the set that I have generated will be a useful resource for population synthesis and other applications.

These higher resolution Kurucz spectra cover a wide range of physical parameters, but to do population modelling it is necessary to supplement these spectra with libraries that cover the extremely high temperature and low temperature spectra. In Chapter 4 I attempt to do this, with some success, although it was not possible to complete the library due to the availability of spectra at higher resolution. This will soon become less of a problem now that the availability of computing resources has improved and higher resolution libraries can be produced.

The next stage was to look at the properties of composite stellar systems. In Chapter 4 I experimented with a range of ways of parameterising galaxy spectra. I found that the direct

methods of empirical population synthesis (least squares fitting and direct inversion) were not practical for the large matrices I was dealing with. One possibility would be to parallelise the direct inversion code so that it could cope with the larger matrices. However the other limitations of this method mean I do not think it would be worth doing this. An alternative to these methods is the Lick indices which is a system that provides a standard way of measuring certain absorption line strengths in the spectra of stars and galaxies.

Finally, in Chapter 5 I investigate some of the spectral properties of observed galaxy spectra, specifically how the Lick indices change with local density. This work primarily used the SDSS spectra. However the 2dF groups catalogue was used to get a measure of local density for each galaxy. Most of the indices demonstrated some overall increase with increasing group velocity dispersion when considering red and blue galaxies together. This is due to the average index for the red sample generally being slightly higher than the average index for the blue sample, and the fraction of red galaxies increasing with group velocity dispersion. When considered separately, several of the indices showed some increase with increasing group velocity dispersion for the red sample (CN_1, CN_2, Fe4383, Fe5015, Mg_1, Mg_2, TiO_2) and several for the blue sample (G4300, Fe4383, Mg *b*, Fe5270). However, these are all fairly weak trends and would have to be tested on larger samples before any conclusions can be drawn. The main limiting factor in my sample size was having to combined the SDSS sources with the 2dF groups catalogue to get the local density information. Using a SDSS groups catalogue, when one becomes available, would avoid this limitation.

The next step in this work would be to compare the results from the SDSS galaxies with predictions from synthetic spectra, using the best-match model galaxies from population synthesis (generated using the higher resolution synthetic spectra presented in Chapter 3). A longer term project that ties together the work in Chapters 4 and 5 would be to use Lick indices and principal component analysis to test the predictions of semi-analytic galaxy formation models such as van Kampen et al. (1999). These models produce a distribution of galaxies, which used in conjunction with galaxy spectral synthesis packages produces a synthetic redshift survey. It would be interesting to test these models by investigating whether the predicted distributions of Lick indices corresponded to the observed distributions in the SDSS.

Bibliography

Aaronson, M. et al.: 1978, ApJ **223**, 824

Abazajian, K. et al.: 2003, AJ, *accepted,* astro-ph/0305492

Abraham, R. G., van den Bergh, S., and Nair, P.: 2003, *Astrophysical Journal* **588**, 218

Allard, F. and Hauschildt, P. H.: 1995, ApJ **445**, 433

Alonso, A., Arribas, S., and Martínez-Roger, C.: 1999, A&AS **139**, 335

Baade, W.: 1944, ApJ **100**, 137

Bailer-Jones, C. A. L.: 2001, in R. Gupta, H. P. Singh, and C. A. L. Bailer-Jones (eds.), *Automated Data Analysis in Astronomy*

Bailer-Jones, C. A. L., Irwin, M., and von Hippel, T.: 1998a, MNRAS **298**, 361

Bailer-Jones, C. A. L., Irwin, M., and von Hippel, T.: 1998b, MNRAS **298**, 1061

Baldry, I. et al.: 2003, ApJ, *submitted*

Barbuy, B. et al.: 2003, A&A **404**, 661

Becker, R. H., White, R. L., and Helfand, D. J.: 1995, ApJ **450**, 559

Bennett, C. L. et al.: 2003, ApJ, *accepted* astro-ph/0302207

Bernardi, M. et al.: 2003, AJ **125**, 1882

Bertone, E. et al.: 2002, in N. Piskunovs, W. W. Weis, and D. F. Gray (eds.), *Modelling of Stellar Atmospheres*

Bessell, M. S.: 1990, PASP **102**, 1181

Bessell, M. S., Castelli, F., and Plez, B.: 1998, A&A **333**, 231

Bessell, M. S. et al.: 1989, A&AS **77**, 1

Bessell, M. S. et al.: 1991, A&AS **89**, 335

Bica, E.: 1988, A&A **195**, 76

Binney, J. and Merrifield, M.: 1998, *Galactic astronomy*, Princeton University Press

Bishop, C. M.: 1995, *Neural Networks for Pattern Recognition*, Clarendon Press

Blackwell, D. E., Shallis, M. J., and Selby, M. J.: 1979, MNRAS **188**, 847

Blanton, M. R. et al.: 2003a, AJ **125**, 2276

Blanton, M. R. et al.: 2003b, AJ **125**, 2348

Boehm-Vitense, E.: 1981, ARA&A **19**, 295

Boehm-Vitense, E.: 1989, *Introduction to stellar astrophysics. Volume 2 - Stellar atmospheres*, Cambridge University Press

Bressan, A. et al.: 1993, A&AS **100**, 647

Bruzual, G.: 2001, *Astrophysics and Space Science Supplement* **277**, 221

Bruzual, G. and Charlot, S.: 1993, ApJ **405**, 538

Bruzual, G. and Charlot, S.: 2003, MNRAS, *accepted,* astro-ph/0309134

Budavari, T. et al.: 2003, ApJ, *accepted,* astro-ph/0305603

Burstein, D. et al.: 1984, ApJ **287**, 586

Burstein, D., Faber, S. M., and Gonzalez, J. J.: 1986, AJ **91**, 1130

Cardelli, J. A., Clayton, G. C., and Mathis, J. S.: 1989, ApJ **345**, 245

Cardiel, N. et al.: 1998, A&AS **127**, 597

Cassisi, S. et al.: 1999, A&AS **134**, 103

Castelli, F., Gratton, R. G., and Kurucz, R. L.: 1997, A&A **318**, 841

Castelli, F. and Munari, U.: 2001, A&A **366**, 1003

Cayrel de Strobel, G. et al.: 1997, A&AS **124**, 299

Cayrel de Strobel, G., Soubiran, C., and Ralite, N.: 2001, A&A **373**, 159

Charbonnel, C. et al.: 1996, A&AS **115**, 339

Charlot, S. and Bruzual, A. G.: 1991, ApJ **367**, 126

Charlot, S., Worthey, G., and Bressan, A.: 1996, ApJ **457**, 625

Chavez, M., Malagnini, M. L., and Morossi, C.: 1997, A&AS **126**, 267

Christlieb, N. et al.: 1997, in *ASSL Vol. 212: Wide-field spectroscopy*, pp 109–+

Clegg, R. E. S. and Middlemass, D.: 1987, MNRAS **228**, 759

Colless, M. et al.: 2001, MNRAS **328**, 1039

Colless, M. et al.: 2003, astro-ph/0306581

Collobert, R. and Bengio, S.: 2001, *Journal of Machine Learning Research* **1**, 143

Combes, F. et al.: 1995, *Galaxies and Cosmology*, Springer-Verlag

Conti, P. S.: 2000, PASP **112**, 1413

Corbally, C. J., Gray, R. O., and Garrison, R. F. (eds.): 1994, *The MK process at 50 years. A powerful tool for astrophysical insight*

Cristianini, N. and Shawe-Taylor, J.: 2000, *An Introduction to Support Vector Machines*, Cambridge University Press

da Costa, L. N. et al.: 2000, AJ **120**, 95

Daubechies, I.: 1988, *Comm. Pure Appl. Math.* **41**, 909

Davis, M. and Geller, M. J.: 1976, ApJ **208**, 13

De Propris, R. et al.: 2003, MNRAS **342**, 725

Djorgovski, S. and Davis, M.: 1987, ApJ **313**, 59

Dressler, A.: 1980, ApJ **236**, 351

Dressler, A. et al.: 1987, ApJ **313**, 42

Dressler, A., Thompson, I. B., and Shectman, S. A.: 1985, ApJ **288**, 481

Eke, V. R. et al.: 2003, *in preparation*

Faber, S. M.: 1972, A&A **20**, 361

Faber, S. M.: 1973, ApJ **179**, 731

Faber, S. M. et al.: 1985, ApJS **57**, 711

Faber, S. M. et al.: 1989, ApJS **69**, 763

Fioc, M. and Rocca-Volmerange, B.: 1997, A&A **326**, 950

Fluks, M. A. et al.: 1994, A&AS **105**, 311

Folkes, S. et al.: 1999, MNRAS **308**, 459

Freedman, W. L. et al.: 2001, ApJ **553**, 47

Fukugita, M. et al.: 1996, AJ **111**, 1748

Gómez, P. L. et al.: 2003, ApJ **584**, 210

Giménez de Castro, C. G. et al.: 2001, A&A **366**, 317

Goderya, S. N. and McGuire, P. C.: 2000, *American Astronomical Society Meeting* 197

Goerdt, A. and Kollatschny, W.: 1998, A&A **337**, 699

González, J. J.: 1993, *Ph.D. Thesis*

González Delgado, R. M. and Leitherer, C.: 1999, ApJS **125**, 479

Gorgas, J. et al.: 1993, ApJS **86**, 153

Gray, R. O.: 1989, AJ **98**, 1049

Gunn, J. E. and Stryker, L. L.: 1983, ApJS **52**, 121

Gunn, J. E., Stryker, L. L., and Tinsley, B. M.: 1981, ApJ **249**, 48

Gustafsson, B. et al.: 1975, A&A **42**, 407

Hanbury Brown, R., Davis, J., and Allen, L. R.: 1974, MNRAS **167**, 121

Harris, H. C. et al.: 2003, AJ, *accepted,* astro-ph/0305347

Hauschildt, P. H., Allard, F., and Baron, E.: 1999a, ApJ **512**, 377

Hauschildt, P. H. et al.: 1999b, ApJ **525**, 871

Heavens, A. F., Jimenez, R., and Lahav, O.: 2000, MNRAS **317**, 965

Heiter, U. et al.: 2002, A&A **392**, 619

Henry, T. J., Kirkpatrick, J. D., and Simons, D. A.: 1994, AJ **108**, 1437

Hogg, D. W. et al.: 2002, astro-ph/0210394

Houdashelt, M. L. and Bell, R. A.: 2003, *Elemental Abundances in Old Stars and Damped Lyman-α Systems, 25th meeting of the IAU, Joint Discussion 15, 22 July 2003, Sydney, Australia* 15

Houdashelt, M. L. et al.: 2000, AJ **119**, 1424

Houk, N.: 1979, in *IAU Colloq. 47: Spectral Classification of the Future*, pp 51–56

Houk, N. and Swift, C.: 1999, *Michigan catalogue of two-dimensional spectral types for the HD Stars ; vol. 5*, Department of Astronomy, University of Michigan

Hubble, E. P.: 1926, ApJ **64**, 321

Humphreys, R. M. et al.: 2001, *American Astronomical Society Meeting* 199

Ibata, R. A. and Irwin, M. J.: 1997, AJ **113**, 1865

Jacoby, G. H., Hunter, D. A., and Christian, C. A.: 1984, ApJS **56**, 257

Johnson, H. L. and Morgan, W. W.: 1953, ApJ **117**, 313

Katz, D. et al.: 1998, A&A **338**, 151

Kauffmann, G. et al.: 2003, MNRAS **341**, 33

Keenan, P. C.: 1993, PASP **105**, 905

Keenan, P. C. and McNeil, R. C.: 1976, *An atlas of spectra of the cooler stars: Types G,K,M,S, and C. Part 1: Introduction and tables*, Ohio State University Press

Kirkpatrick, J. D., Henry, T. J., and Simons, D. A.: 1995, AJ **109**, 797

Kong, X. and Cheng, F. Z.: 2001, MNRAS **323**, 1035

Kupka, F. G. et al.: 2000, *Baltic Astronomy* **9**, 590

Kurtz, M. J.: 1982, *Ph.D. Thesis*

Kurtz, M. J. and Lasala, J.: 1991, in *Objective-Prism and Other Surveys*, pp 133–+

Kurucz, R.: 1992, in *IAU Symp. 149: The Stellar Populations of Galaxies*, p. 225

Kurucz, R.: 1993a, *ATLAS9 Stellar Atmosphere Programs and 2 km/s grid. Kurucz CD-ROM No. 13. Cambridge, Mass.: Smithsonian Astrophysical Observatory, 1993.* 13

Kurucz, R.: 1993b, *Diatomic Molecular Data for Opacity Calculations. Kurucz CD-ROM No. 15. Cambridge, Mass.: Smithsonian Astrophysical Observatory, 1993.* 15

Kurucz, R.: 1993c, *SYNTHE Spectrum Synthesis Programs and Line Data. Kurucz CD-ROM No. 18. Cambridge, Mass.: Smithsonian Astrophysical Observatory, 1993.* 18

Kurucz, R.: 1994, *Atomic data for opacity calculations. Kurucz CD-ROM No. 1. Cambridge, Mass.: Smithsonian Astrophysical Observatory, 1994.* 1

Kurucz, R.: 1999, *1999 TiO linelist from Schwenke (1998). Kurucz CD-ROM No. 24. Cambridge, Mass.: Smithsonian Astrophysical Observatory, 1999.* 24

Kurucz, R. L.: 1979, ApJS **40**, 1

Kurucz, R. L.: 1995, in *ASP Conf. Ser. 81: Laboratory and Astronomical High Resolution Spectra*, pp 583–+

Kurucz, R. L.: 1996, in *ASP Conf. Ser. 108: M.A.S.S., Model Atmospheres and Spectrum Synthesis*, pp 160–+

Lambert, D. L. (ed.): 1991, *Frontiers of stellar evolution*

Langer, W. D., Wilson, R. W., and Anderson, C. H.: 1993, ApJ **408**, L45

Lasala, J.: 1994, in *ASP Conf. Ser. 60: The MK Process at 50 Years: A Powerful Tool for Astrophysical Insight*, pp 312–+

Lasala, J. and Kurtz, M. J.: 1985, PASP **97**, 605

Le Borgne, J.-F. et al.: 2003, A&A **402**, 433

Leitherer, C. et al.: 1996a, PASP **108**, 996

Leitherer, C., Fritze-von Alvensleben, U., and Huchra, J. (eds.): 1996b, *From stars to galaxies: The impact of stellar physics on galaxy evolution*

Lejeune, T., Cuisinier, F., and Buser, R.: 1997, A&AS **125**, 229

Lejeune, T., Cuisinier, F., and Buser, R.: 1998, A&AS **130**, 65

Lemson, G. and Kauffmann, G.: 1999, MNRAS **302**, 111

Lindegren, L. and Perryman, M. A. C.: 1996, A&AS **116**, 579

Madgwick, D. S. et al.: 2002, MNRAS **333**, 133

Malyuto, V.: 1984, in *ASSL Vol. 110: IAU Colloq. 78: Astronomy with Schmidt-Type Telescopes*, pp 287–+

Maraston, C.: 2003, astro-ph/0301419

Martínez, H. J. et al.: 2002, MNRAS **333**, L31

Merchán, M. and Zandivarez, A.: 2002, MNRAS **335**, 216

Meyer, Y.: 1993, *Wavelets: Algorithms and Applications*, SIAM

Milhalas, D.: 1978, *Stellar Atmospheres*, W. H. Freeman

Mitchell, T.: 1997, *Machine Learning*, McGraw-Hill

Morgan, W. W.: 1958, PASP **70**, 364

Morgan, W. W., Abt, H. A., and Tapscott, J. W.: 1978, *Revised MK Spectral Atlas for stars earlier than the sun*, Yerkes Observatory and Kitt Peak National Observatory

Morgan, W. W. and Keenan, P. C.: 1973, ARA&A **11**, 29

Morgan, W. W., Keenan, P. C., and Kellman, E.: 1943, *An atlas of stellar spectra, with an outline of spectral classification*, The University of Chicago press

Morton, D. C.: 1991, ApJS **77**, 119

Moultaka, J. and Pelat, D.: 2000, MNRAS **314**, 409

Murtagh, F. and Heck, A.: 1987, *Multivariate data analysis*, Astrophysics and Space Science Library

Ostlie, D. A. and Carroll, B. W.: 1996, *An Introduction to Modern Stellar Astrophysics*, Addison-Wesley

Peacock, J. A.: 2000, *Cosmological Physics*, Cambridge University Press

Peebles, J.: 1993, *Principles of Physical Cosmology*, Princton University Press

Pelat, D.: 1997, MNRAS **284**, 365

Pelat, D.: 1998, MNRAS **299**, 877

Peletier, R.: 1999, in *ASP Conf. Ser. 187: The Evolution of Galaxies on Cosmological Timescales*, pp 231–244

Petrosian, V.: 1976, ApJ **209**, L1

Pickles, A. J.: 1985, ApJ **296**, 340

Pickles, A. J.: 1998, PASP **110**, 863

Pickles, A. J. and Visvanathan, N.: 1985, ApJ **294**, 134

Plez, B.: 1992, A&AS **94**, 527

Plez, B., Brett, J. M., and Nordlund, A.: 1992, A&A **256**, 551

Poggianti, B. M., Bressan, A., and Franceschini, A.: 2001, ApJ **550**, 195

Press, W. H. et al.: 1992, *Numerical recipes in C. The art of scientific computing*, Cambridge University Press

Prugniel, P. and Soubiran, C.: 2001, A&A **369**, 1048

Puzia, T. H. et al.: 2002, A&A **395**, 45

Renzini, A. and Buzzoni, A.: 1986, in *ASSL Vol. 122: Spectral Evolution of Galaxies*, pp 195–231

Ridgway, S. T. et al.: 1980, ApJ **235**, 126

Roberts, M. S. and Haynes, M. P.: 1994, ARA&A **32**, 115

Salpeter, E. E.: 1955, ApJ **121**, 161

Schaller, G. et al.: 1992, A&AS **96**, 269

Schechter, P.: 1976, ApJ **203**, 297

Schlegel, D. J., Finkbeiner, D. P., and Davis, M.: 1998, ApJ **500**, 525

Schmidt, A. et al.: 1989, Ap&SS **157**, 79

Schmidt, A. A. et al.: 1991, MNRAS **249**, 766

Schmidt-Kaler, T.: 1979, in *IAU Colloq. 47: Spectral Classification of the Future*, pp 285+

Schmidt-Kaler, T.: 1982, in L. H. Aller et al. (eds.), *Numerical Data and Functional Relationships in Science and Technology*

Seaton, M. J.: 1995, *The opacity project*, Institute of Physics Pub.

Silva, D. R. and Cornell, M. E.: 1992, ApJS **81**, 865

Singh, H. P., Gulati, R. K., and Gupta, R.: 1998, MNRAS **295**, 312

Sion, E. M. et al.: 1983, ApJ **269**, 253

Smalley, B. et al.: 2002, A&A **395**, 601

Smalley, B. and Kupka, F.: 1997, A&A **328**, 349

Solanes, J. M. et al.: 2001, ApJ **548**, 97

Steinmetz, M.: 2002, in U. Munari (ed.), *GAIA Spectroscopy, Science and Technology*

Stoughton, C. et al.: 2002, AJ **123**, 485

Straižys, V., Lazauskaite, R., and Valiauga, G.: 2002, *Baltic Astronomy* **11**, 341

Straižys, V., Liubertas, R., and Valiauga, G.: 1997, *Baltic Astronomy* **6**, 601

Strateva, I. et al.: 2001, AJ **122**, 1861

Strauss, M. A. et al.: 2002, AJ **124**, 1810

Tantalo, R., Chiosi, C., and Bressan, A.: 1998, A&A **333**, 419

Thomas, D., Maraston, C., and Bender, R.: 2003, MNRAS **339**, 897

Tinsley, B. M. and Gunn, J. E.: 1976, ApJ **203**, 52

Trager, S. C.: 1997, *Ph.D. Thesis*

Trager, S. C. et al.: 1998, ApJS **116**, 1

Tripicco, M. J. and Bell, R. A.: 1995, AJ **110**, 3035

Tully, R. B. and Fisher, J. R.: 1977, A&A **54**, 661

Tully, R. B., Mould, J. R., and Aaronson, M.: 1982, ApJ **257**, 527

van Kampen, E., Jimenez, R., and Peacock, J. A.: 1999, MNRAS **310**, 43

Vazdekis, A. et al.: 1996, ApJS **106**, 307

Vieira, E. F. and Ponz, J. D.: 1995, A&AS **111**, 393

Voges, W. et al.: 1999, A&A **349**, 389

Weaver, W. B. and Torres-Dodgen, A. V.: 1997, ApJ **487**, 847

West, R. M.: 1973, in *IAU Symp. 50: Spectral Classification and Multicolour Photometry*, pp 109–+

Whipple, F. L.: 1935, *Harvard College Observatory Circular* **404**, 1

Whitney, C. A.: 1983, A&AS **51**, 443

Worthey, G.: 1998, PASP **110**, 888

Worthey, G. et al.: 1994, ApJS **94**, 687

Worthey, G., Faber, S. M., and Gonzalez, J. J.: 1992, ApJ **398**, 69

Worthey, G. and Ottaviani, D. L.: 1997, ApJS **111**, 377

Wozniak, P. R. et al.: 2001, *American Astronomical Society Meeting* 199

Yi, S. et al.: 2001, ApJS **136**, 417

Yip, C.-W. et al.: 2003, *in preparation*

York, D. G. et al.: 2000, AJ **120**, 1579

Zekl, H.: 1982, A&A **108**, 380

Zwitter, T., Munari, U., and Castelli, F.: 2002, in U. Munari (ed.), *GAIA Spectroscopy, Science and Technology*